Ultrashort pulse induced nanostructures in transparent materials

Dissertation

zur Erlangung des akademischen Grades

doctor rerum naturalium (Dr. rer. nat.)

vorgelegt dem Rat der Physikalisch-Astronomischen Fakultät

der Friedrich-Schiller-Universität Jena

von Dipl.-Phys. Felix Zimmermann,

geboren am 24.06.1986 in Suhl

1. Gutachter: Prof. Dr. Stefan Nolte, Jena

2. Gutachter: Prof. Dr. Hartmut Bartelt, Jena

3. Gutachter: Prof. Dr. Ya Cheng, Shanghai (China)

Tag der Disputation: 28. März 2017

Contents

1 Introduction

Glass fascinates mankind since its first discovery about 30 thousand years ago. Besides the challenging conditions for fabricating glasses with homogeneous properties the technological prospects for precise machining were first developed in the last millennium. While core areas of glass processing were dominated by well-established mechanical techniques such as scribing, grinding, sawing and polishing the technological progress and ongoing miniaturization demanded alternative processing tools. Within the end of the 20^{th} century the development of ultrashort pulse laser systems paved the way for precise and cost-efficient solutions for materials processing in key technologies such as computer chips, medical surgery or in the field of automotive. Even more, the short pulse duration represents the key to locally process transparent materials within the bulk to induce modifications with feature sizes smaller than the wavelength of light [1, 2].

When focusing ultrashort laser pulses in the bulk of glass nonlinear absorption leads to extreme non-equilibrium states within a confined volume mediating the localized deposition of the laser pulse energy. Fused silica turned out as versatile platform to study the laser-induced modifications. Typically three different kinds are distinguished. First, isotropic refractive index changes allow for inscribing waveguides [3, 4] that may serve to realize complex photonic networks [5, 6]. Second, a confined micro-explosion within the focal volume may leave a region devoid of any material [7, 8] that can be used for data storage [9] or microfluidic purposes [10]. Finally, one of the key findings of laser materials processing is the local inscription of strong birefringence due to a sub-wavelength grating structure within an otherwise isotropic host material [11, 12].

The observation of local anisotropy under laser irradiation goes back to the discovery of laser-induced periodic surface structures (LIPSS) in the 1960s [13]. While LIPSS can be induced on the surface of various materials using cw and pulsed laser irradiation, periodic nanostructures in the bulk of transparent materials, so-called nanogratings, uniquely form when using ultrashort laser pulses. First studies of these nanogratings discovered anisotropic light scattering in germanium doped silica [11] as well as in pristine silica

[14] after femtosecond laser irradiation. In 2003, Shimotsuma et al. reported on the underlying nanostructure with sub-wavelength periodicity which causes the induced birefringence [12]. Later on it was found that the orientation of the grating planes is always perpendicular to the laser polarization, while the formation of the grating (typically ascribed as a self-organization mechanism) requires several hundreds of laser pulses [15]. Thus, the degree of birefringence can be tuned by setting the laser parameters adequately. In combination with the direct writing technique using a high precision translation stage, the three spatial degrees of freedom (x, y, z), and the possibility of locally tailoring the birefringence amplitude and orientation enables the fabrication of various photonic functionalities. These range from wave plates for the generation of diverse polarization states [16, 17], computer generated holograms [18] to microscopic applications [19].
Moreover, nanogratings can be rewritten, i.e. an existing nanograting is erased and newly arranged when inscribing again at the same position with a differently oriented polarization direction [20]. This phenomenon is useful for data storage applications since imprinted information in terms of nanograting-based data units can easily be corrected or updated as needed.
Above all, nanogratings were assumed to be a special feature of laser-irradiated fused silica due to the anomalous glass density behavior on the fictive temperature [21]. Contrarily, the observation of nanogratings in crystals such as tellurium dioxide single crystal and sapphire has been reported, too [22, 23]. The irradiation leads to rapid ionization and bond breaking of the glass network (SiO_2 tetrahedrons in case of silica). Consequently, laser-irradiated glass is composed of point defects which in turn might mediate the feedback process towards a quasi-periodic nanograting. The observation of nanogratings in different materials such as crystals suggests that a general process dictates the self-assembling. Since their discovery several theories were put forward to explain the formation of nanogratings [12, 24, 15, 25]. However, these models may only disclose individual aspects of the nanograting characteristics. The nanoplasmonic model, for instance, describes the nanograting formation based on anisotropic growth of plasma hot spots which subsequently arrange periodically via quasi-metallic waveguiding [15]. The imprinted nanograting exhibits periods corresponding to $\lambda/2n$ (λ - laser wavelength, n - refractive index of the bulk material). However, the model does not explain the continuous shift of the periodicity with varying pulse overlap that has been measured experimentally [16]. Another approach was made by Beresna et al. reporting on a longitudinal periodicity of nanogratings (along the laser inscription direction) which is explained by short-living exciton-polaritons [25].

The formation of the transverse periodicity, however, remains open. This highlights, that the underlying formation mechanism is still elusive.
From an experimental point of view, one challenging aspect is the structural investigation of the nanostructures buried in the bulk of glasses. Mostly polishing and subsequent etching is used to excavate the induced structures making them accessible to electron microscopy (SEM) [26, 27]. However, etching destroys the underlying fine structure and reveals only the coarse structure of nanogratings such as the grating bars. Thus, the question came up whether nanogratings are composed of a merely continuous modulation of the material density [28] or consist of microscopic voids arranged in quasi-periodic grating planes. In contrast, a microscopic pore morphology was observed after cleaving of laser-irradiated samples and subsequent imaging with SEM [29]. However, these time-consuming preparation methods visualize arbitrary cross sections and hardly reveal information about the ensemble of microscopic structures induced. In addition, these methods are not suited to investigate various parameter dependencies of nanogratings.
The goal of this thesis is to explore the formation of nanogratings uncovering the fundamental constituents and their formation into regular nanostructures. Based on the current state of knowledge the nanograting characteristics and their emergence sequence during the cumulative action of several ultrashort laser pulses are studied. Moreover the rewriting of nanogratings as well as their relation to periodic surface structures is analyzed. To uncover the nanostructure dependence on the material composition different glasses are investigated under ultrashort laser irradiation. These investigations serve to develop a new understanding of the nanograting genesis. In addition, the generation of local anisotropy is used to realize various photonic functionalities for polarization manipulation that can be applied for high-resolution microscopy.
After this introduction, **Chapter 2** deals with the current state of knowledge providing an overview on the absorption of ultrashort laser pulses, the resulting material modifications as well as theoretical aspects of the nanograting formation. Subsequently, in **Chapter 3** laser-induced nanostructures in fused silica are investigated. After exploring their formation threshold and characteristics in dependence of various process parameters, laser-induced defects and the temperature stability of nanostructures are studied. **Chapter 4** covers in-situ measurements of the nanograting evolution as well as the step-wise formation based on small-angle X-ray scattering (SAXS) and focused ion beam (FIB) milling in combination with SEM. Subsequently, rewriting of nanogratings and laser-induced surface structures are explored. Afterwards nanostructures in different glasses ranging from

common glass types such as borosilicate and titanium doped low expansion glass (ULE, Schott) to selectively doped glasses are studied and the findings are summed up to develop a new model of the nanograting formation. Finally, **Chapter 5** presents applications of laser-induced nanostructures for high-resolution microscopy which is followed by the conclusion and outlook.

2 Current state of knowledge

2.1 Fundamentals of glasses

Glasses are the backbone of nowadays life due to their outstanding mechanical, chemical and optical properties. In general, glasses can be defined as frozen-in supercooled liquids [30, 31]. They exhibit an amorphous structure without any long range periodic atomic arrangement. The most commonly used glasses are silica based. The vitreous silica, known as fused silica, consists of 4 oxygen and one silicon atom building relatively rigid SiO_4 tetrahedrons. These are linked at all four corners, while each oxygen atom is shared between two silicon atoms (Si-O-Si) to form a three-dimensional network. While the tetrahedrons have a high internal order [32], different angles for the interconnection as well as rotation of the tetrahedrons are allowed. These building blocks form rings consisting of three or more - but predominantly 5 and 6 tetrahedrons. The structure of pristine silica exhibits regions of strained Si-O bonds and dangling bond type defects [33, 30] such as silicon dangling bonds ($E^{'}$-center) and oxygen dangling bonds (”non-bridging oxygen hole center, NBOHC”). In addition, peroxy defects (Si-O-O-Si) or defects associated to impurity sites especially SiH or SiOH exist.

Another important property is the time-dependent glass transformation behavior. Glasses are fabricated by cooling of melts with comparatively high cooling rate to avoid crystallization. If so, the liquid melt is cooled below the softening temperature of the crystal forming a supercooled liquid. The enthalpy (or volume) gradually decreases without any abrupt decrease due to discontinuous structural rearrangement (see Fig. 2.1). During this process the viscosity increases until the atoms can no longer arrange to the equilibrium liquid structure. The enthalpy departs from the equilibrium line of the liquid and finally merges the enthalpy of the solid while the temperature region in between is known as transformation region. The temperature at which the enthalpy of the solid and the liquid line intersects is called fictive temperature. It describes the structure of a glass which is

considered to be the equilibrium liquid at the fictive temperature [30]. This is typically used as a measure for the glass structure and depends on kinetic factors such as the cooling rate.

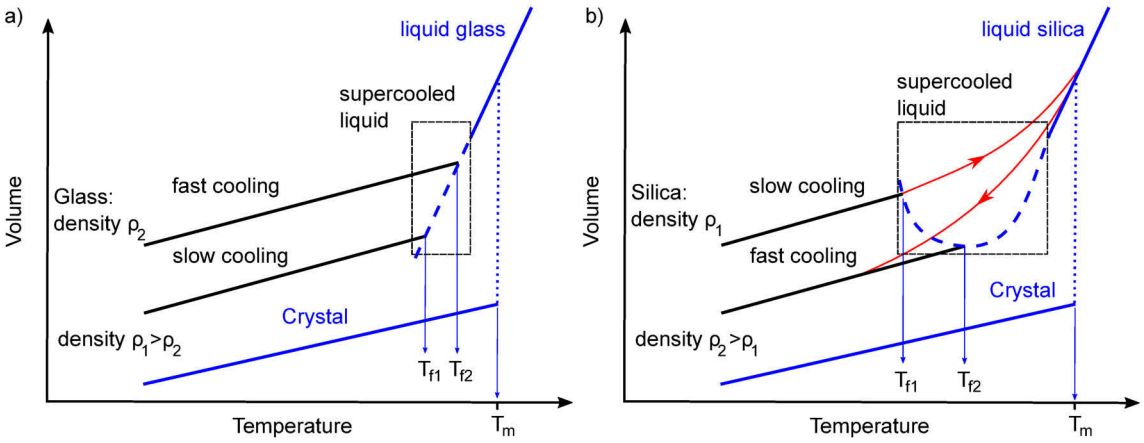

Fig. 2.1: Glass transition behavior for normal glasses (a) and silica (b), according to [34, 35]. Fast heating and cooling (indicated by the red trace) leads to increased glass density due to the *anomaly of silica*. The dashed curve represents the volume change as function of the fictive temperature.

Typically two kinds of glasses can be distinguished. For *normal* glasses (e.g. Borofloat 33, Schott) the final volume after rapid cooling is higher in contrast to low cooling rates (see Fig. 2.1 (a)). Pristine silica is known to exhibit *anomalous* behavior leading to smaller volume and hence higher density after rapid cooling [34] (see Fig. 2.1 (b)). This results in a modified network structure in terms of an increased number of 3- and 4-fold rings [36, 37] that can be measured by Raman spectroscopy [38].

The glass properties such as the softening point or the glass density behavior on the fictive temperature can be changed by adding network modifiers (K, Ba, Na) to the glass melt. The resulting structure gets more complex as the regular structure of SiO_4 tetrahedrons gets disturbed. Common glasses such as borosilicate glasses (e.g. BK7 or Borofloat 33, Schott) consist of multiple components (e.g. SiO_2, B_2O_3, Na_2O, K_2O [39]) while their basic network structure is similar to silica with boron atoms replacing some silicon. However, to sequentially change fundamental glass properties binary glass systems are well suited as these consist of fully linked networks containing mixtures of e.g. silica and germanium tetrahedrons [40]. Thus, in this work, several glass types ranging from common types for optical applications as well as binary glasses with tailored composition (doping percentage) were used.

2.2 Absorption of ultrashort laser pulses in transparent materials

The density of free electrons in the conduction band of transparent materials at room temperature is small (10^8-10^{10} cm^{-3}) and mostly defect-induced [41]. In addition, the bandgap (E_g, e.g. 9 eV for fused silica) is typically larger than the energy of a single photon (e.g. 2.4 eV at 515 nm) resulting in negligible linear absorption of light. In contrast, ultrashort laser pulses with a pulse duration of e.g. 500 fs and a pulse energy of 200 nJ can provide intensities around 10^{13} $\frac{W}{cm^2}$ when focused with a numerical aperture NA $\geq$ 0.1. Consequently, the high intensities trigger nonlinear absorption mechanisms that allow for the excitation of electrons into the conduction band [42].

The initial generation of quasi-free electrons is driven by either multiphoton absorption or field ionization [43]. In case of multiphoton absorption n photons of energy E_{ph}=hv are simultaneously absorbed leading to the bridging of the band gap (E_g) if the condition n·hv$\geq$ E_g is fulfilled [44, 45]. For field ionization the strong laser field distorts the atomic Coulomb field enabling an electron to tunnel through the remaining potential barrier [45, 46]. To distinguish between both processes the Keldysh parameter:

$$\gamma = \frac{w}{e}\sqrt{\frac{E_g m_e^* c n_0 \epsilon_0}{2I}} \tag{2.1}$$

is used [47]. Here w denotes the angular frequency, e the elementary charge, m_e^* the effective electron mass, c the speed of light, n_0 the refractive index, ϵ_0 the electric permittivity and I the laser intensity. When $\gamma \gg 1$ multiphoton absorption is dominant while field ionization prevails if $\gamma \ll 1$. For the intermediate regime, i.e. where the Keldysh parameter is nearly one (as in this work) both mechanisms contribute as illustrated in Figure 2.2 (a).

After the initial generation of excited electrons the further absorption process is mostly governed by avalanche ionization. Excited electrons sequentially absorb single photons by inverse Bremsstrahlung and reach an energy state that exceeds the band gap. Due to inelastic collisions (impact ionization) the acquired energy can be transferred to an electron in the valence band which gets excited leading to both electrons located at the conduction band minimum. Subsequently this process can be repeated to form an electron avalanche (see Fig. 2.2 (b)).

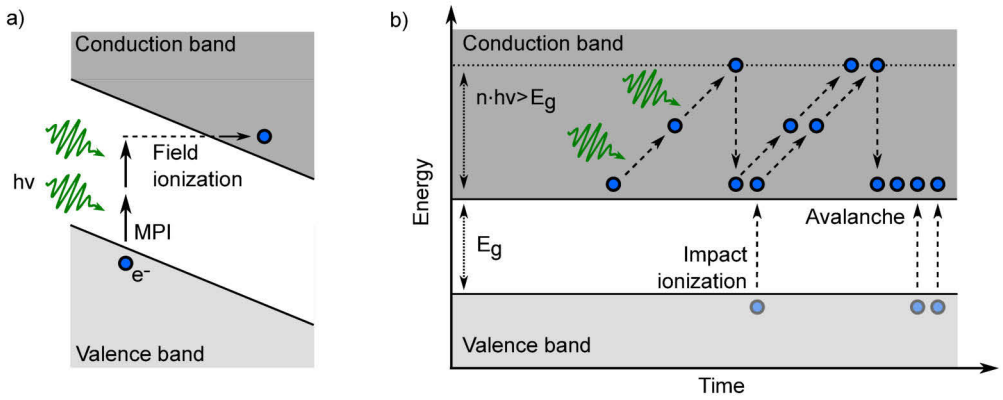

Fig. 2.2: (a) Illustration of the intermediate regime where multiphoton ionization (MPI) and field ionization generate a free electron. (b) Sketch of the avalanche ionization process.

The above mentioned absorption mechanism and the resulting material modification largely depend on the laser pulse duration. Excited electrons in the conduction band distribute their energy due to collisions among each other on timescales of 10-100 fs [48]. Thus, avalanche ionization is in particular dominant for longer pulse durations while multiphoton ionization, in addition strongly depending on the pulse intensity, is favored when using short pulse durations (<100 fs).

The rapid excitation of electrons by the above mentioned processes happens much faster than the energy can be transferred to the lattice. This is due to the corresponding electron-phonon collision time (typically a few ps [49, 50]) that is larger than the pulse duration of ultrashort laser pulses. Consequently strong non-equilibrium conditions are generated since the lattice remains cold for the time the laser pulse is present. The subsequent transfer of energy to the lattice is decoupled from the excitation and hence the modification zone is mainly confined to the irradiated region in contrast when using longer pulse durations (e.g. ns-pulses).

The formation of permanent damage is typically linked to the critical electron density n_{cr} [45, 43]. When the electron density of the excited material n_e approaches the critical electron density ($n_{cr} \sim 10^{20}\,\mathrm{cm}^{-3}$ for a laser wavelength of 515 nm) the plasma frequency:

$$\omega_{pl} = \sqrt{\frac{n_e e^2}{m_e \epsilon_0}}, \tag{2.2}$$

with m_e being the mass of an electron, equals the laser frequency leading to strong absorption as well as reflection of the laser light. Subsequently, thermalization of the lattice

occurs within a few tens of picoseconds. On longer timescales, shock wave propagation, heat diffusion and rapid quenching of the glass induces structural changes [1, 51].

2.3 Laser-induced modifications

The resulting modifications range depending on the excitation conditions from refractive index change, cracking, void formation to local melting. The latter is linked to the heat diffusion time $t_D = \omega_0^2/D$, with ω_0 the focal radius and D the diffusivity of the material. The diffusivity is defined as: $D = \kappa/(\rho c_p)$, with κ the thermal conductivity, ρ the material density and c_p the specific heat. In fused silica the heat diffusion time corresponds to 1 µs assuming a focal size of 1 µm (e.g. focusing with a numerical aperture of 0.5 at a laser wavelength of 515 nm). When the time in between two successive laser pulses is shorter than this time the temperature in the focal volume increases step-wise from pulse to pulse (so-called heat accumulation) leading to local melting [51, 52].
Figure 2.3 (a) illustrates the femtosecond processing geometry mostly used for inducing structural changes. Objectives with high numerical aperture (NA > 0.1) serve to focus the laser pulses into the bulk. By use of high precision translation stages extended regions with almost arbitrary geometries can be inscribed while moving the sample and/or the objective to scan the laser focus correspondingly (so-called *laser direct writing*). For fused silica three types of modifications can be distinguished: isotropic refractive index changes (so-called type I) typically used for waveguiding [3], local birefringence due to so-called nanogratings (type II) [12] and confined voids [7, 8] (see Fig. 2.3 (b)). These three types can be clearly distinguished for pulse durations below 200 fs while at higher pulse durations nanogratings form already above a permanent damage threshold [53]. In the following the modifications will be briefly explained.

2.3.1 Isotropic refractive index change

When tightly focusing femtosecond pulses into the bulk rapid heating and subsequent quenching of the glass matrix leads to a local increase of the fictive temperature. Due to the anomaly of silica (see Fig. 2.1 (b)) this corresponds to densification of the irradiated region. Raman investigations reveal an increased number of 3- and 4-fold rings while 5- and 6- fold rings decrease in number as well as a smaller overall bonding angle of silicon atoms, respectively [37, 54, 55]. As first discovered by Davis et al. a smooth refractive

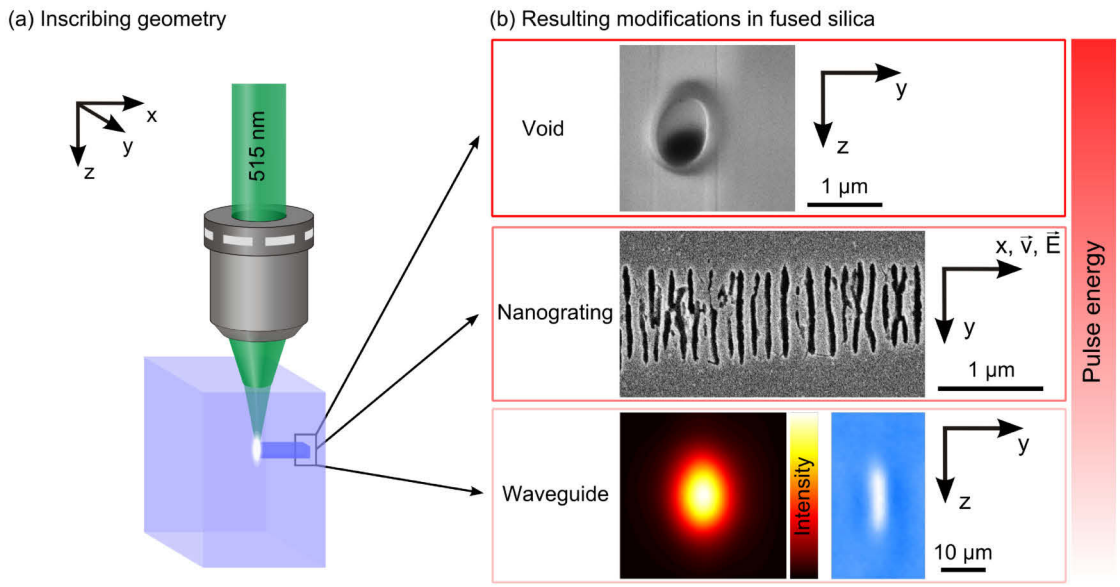

Fig. 2.3: (a) Sketch of the laser inscribing geometry. (b) Resulting structural modifications in fused silica (from top to bottom): SEM image of a void, a nanograting trace, and microscope image (bottom right) as well as measured mode field at 633 nm (bottom left) of a waveguide.

index increase of about 0.035 can be obtained allowing for guiding of light [3]. Further publications demonstrated the application for low-loss (<0.15 dB/cm) waveguides [52, 56, 57] that, even more, opened a wide field for studying complex photonic networks [4, 58]. In Figure 2.3 (b) an exemplary waveguide as well as the corresponding mode field is shown.

2.3.2 Void formation

In the case of very high peak intensities the excited electrons are strongly heated by the laser field resulting in high electron temperatures and pressure that may exceed the bulk modulus of the glass. This triggers a confined micro-explosion within the irradiated region. As a consequence a rarefaction wave propagates radially outward leaving an empty void [59, 7]. Due to mass conservation the void is surrounded by densified material such as the high pressure modifications of silica (e.g. stishovite) [60, 9]. The size of the voids scales with the laser pulse energy and is typically less than one micrometer when using strong focusing (NA≈1) and a pulse energy of a few hundred nJ (see Fig. 2.3 (c)). The voids can be arbitrarily arranged in 3D and sized for data storage purposes [59].

2.3.3 Birefringent material modification

Most intriguingly local birefringence due to so-called nanogratings can be induced when using an intermediate regime of pulse energy. First observations were made by Kazansky et al. who reported on anisotropic light scattering in germanium doped silica after femtosecond laser irradiation [11]. Soon local birefringence of laser processed fused silica was discovered by Sudrie et al. [14]. Later, in 2003, an underlying grating structure with periods smaller than the wavelength of the inscription laser turned out to cause this birefringence [12]. Moreover it was found that these nanogratings always orientate perpendicular to the laser polarization. In addition, besides the transversal periodicity (see e.g. Fig. 2.3 (b)), a second periodicity in longitudinal direction (along the laser inscription direction) was discovered by Beresna et al. [25]. However, the longitudinal periodicity can be obtained when using high laser pulse energies only [26, 61].
Within numerous studies it was found that the nanogratings evolve during the cumulative action of several hundreds of laser pulses leading to strong birefringence [53, 15, 16]. This birefringence is mostly due to the anisotropic nature of the grating structure and hence is denoted as form-birefringence. However, also stress-birefringence due to glass quenching and morphological changes accounts to the total birefringence [62]. Still, in a simplified sketch nanogratings can be described as a periodic modulation of the refractive index as shown in Figure 2.4
A dielectric material composed of thin layers (compared to the wavelength) with a refractive index n_2 and thickness w_2 separated by material with n_1 and w_1 appears optically homogeneous and can be described by the effective medium theory [63]. Assuming the period ($\Lambda = w_1 + w_2$) is smaller than the wavelength of light the structure behaves as an uniaxial negative crystal with the optical axis (n_0 - ordinary refractive index) normal to the grating planes. The resulting form-birefringence ($n_e - n_0$; n_e - extraordinary refractive index) is given by [15, 63]:

$$n_e^2 - n_0^2 = \frac{f(f-1)\left(n_2^2 - n_1^2\right)^2}{f n_1^2 + (1-f) n_2^2}, \tag{2.3}$$

with the geometrical parameter $f = \frac{w_2}{w_1+w_2} = w_2/\Lambda$. A typical value for the birefringence of nanogratings is $n_e - n_0$ = -4·10^{-3} [64]. Correspondingly, the optical retardance, which is the product of the size of the modified region (typically several µm, see Fig. 2.4) and the birefringence, can be as high as 350 nm at a probe wavelength of 546 nm [65]. Assuming

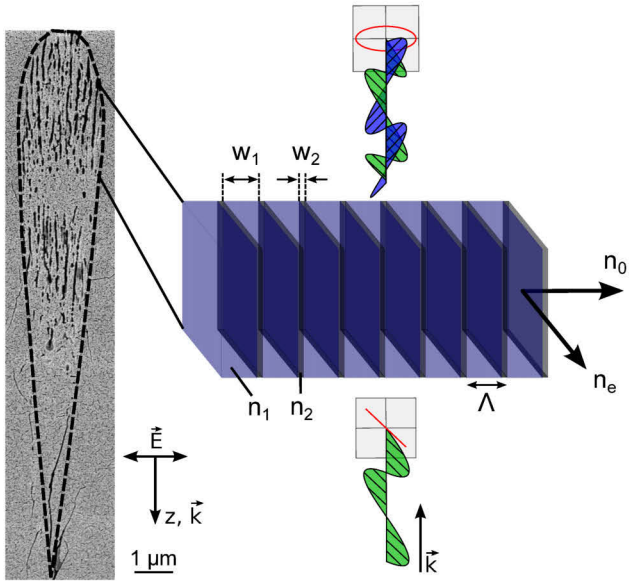

Fig. 2.4: (left) SEM image of longitudinal cross section (along the laser inscribing direction) of nanogratings and (right) sketch of the form-birefringence model.

the grating planes are embedded in glass with $n_1 = 1.45$ (at 633 nm) and $n_e \approx n_0 \approx n_1$ while the grating planes are thin ($w_2 \ll w_1$) the Equation 2.3 can be written as [15]:

$$n_0 - n_e \approx \frac{2w_2}{\Lambda}\left(\frac{\delta n^2}{n_1} + \frac{\delta n^3}{n_1^2}\right). \tag{2.4}$$

In this approximation geometrical factors of the grating (period and plane thickness) together with the refractive index contrast $\delta n = n_1 - n_2$ determine the form-birefringence. This index contrast is positive based on the strong decrease of refractive index compared to the bulk value within the grating planes of about (-0.4 to -0.2) in contrast to a slight increase in between the grating planes of (0.02 to 0.05) [28].

Since the amount and orientation of the birefringence induced can be set with the laser parameters and polarization, respectively, nanogratings build the backbone of versatile photonic functionalities. These range from wave plates for polarization manipulation and the generation of optical vortices [66, 16], computer generated holograms [18], data storage purposes [7, 67] to microfluidic applications using the increased etch rate in contrast to untreated silica [68, 10].

From the first observations of the grating structure it was speculated about the constituents of nanogratings [12]. First SEM images using backscattering electron contrast

illustrated the periodic grating planes while almost no topographic contrast could be detected studying secondary electron images. Thus, it was assumed that nanogratings are merely continuous modulation patterns of the material contrast [28]. Other studies of polished and etched nanograting samples assumed that the grating planes rather consist of photo-induced nanocracks [26]. However, etching blurs the underlying structure leaving only coarse features such as grating planes. Still, more recent observations of fractured cross sections suggest that nanogratings consist of self-aligned nanocracks with a thickness of 20 nm [15, 29]. Although morphological changes due to stress relaxation during cleaving can not be fully excluded the assumption of empty cracks explains the tremendous birefringence of nanogratings [69].

2.4 Theoretical aspects of nanostructure formation

Although many theories have put forward to explain the experimentally observed formation, evolution as well as physical phenomena linked to nanogratings the involved mechanism are still elusive and object of intense research [70, 71]. The initial theory came up with the discovery of the grating structure by Shimotsuma et al. [12] and was, due to similarities in periodicity and alignment, motivated by the well-known laser-induced periodic surface structures (LIPSS) [13, 72]. The model bases on interference of the incident laser field with the laser-induced plasma waves leading to a periodic modulation within the bulk. However, the resulting nanograting properties (e.g. distance of the grating planes) strongly depend on the optical properties and the temperature of the plasma. In contrast the strong pulse energy dependence of the period could not be confirmed by experimental observations.

Another model was proposed by Taylor et al. [15, 73] explaining the formation in three steps: (1.) Localized absorption at intrinsic defects leads to spherical plasma hot spots. These hot spots grow (2.) to anisotropic plasma sheets perpendicular to the laser polarization due to local field enhancement. This growth is based on a feedback mechanism from pulse to pulse while laser-induced defects lower the ionization rate for the subsequent pulse. Finally, the plasma disks merge into nanoplanes and (3.) periodically arrange due to a cavity-like amplification process. The anisotropic plasma planes act as quasi-metallic waveguides while their distance (grating period) is pinned at the lowest optical (TM - transverse magnetic) mode [74, 73]. Consequently, the distance of grating planes is

constant and corresponds to λ/2n, with λ being the laser wavelength and n the refractive index of the bulk glass. However, the continuously decreasing period when increasing the number of applied laser pulses can not be explained by this, even if the refractive index changes [16].
Another approach concentrates on the explanation of the longitudinal periodicity of nanogratings based on short-living exciton-polaritons [25]. This assumes low electron densities to avoid screening of the exciton-polariton interaction by the laser-induced plasma [70]. However, the model does not explain the fact that at low laser pulse energies the longitudinal periodicity can not be obtained [26, 61]. In addition, the explanation of the transversal periodicity remains open.
Finally, Liao et al. proposed the excitation of surface plasma waves at the interfaces of unmodified and modified material [75]. Thus the electric field becomes periodically modulated while the resulting period of the imprinted grating depends on the electron density. In contrast, experimental observations of the local rearrangement of the modified material exclude the interaction of the laser field with surface plasma waves [76].
Recent theoretical studies demonstrate that laser-induced defects and material inhomogeneities mediate the feedback process and the fact, that these increase in number from pulse to pulse, may facilitate the continuous shift of periodicity [71, 77]. Thus, by slightly changing the material composition (doping) may allow for studying the nanograting characteristics and hence the influence of the host material. This will be studied in detail in Chapter 4.5.

3 Laser-induced nanostructures in fused silica

In this chapter the formation of nanostructures in fused silica is investigated. First the experimental approach for inscribing and characterizing the nanostructures is presented. Subsequently this chapter covers the influence of the most relevant process parameters on the formation and characteristics of nanogratings. Finally, laser-induced defects which mediate the formation process, mesoscopic and microscopic network changes as well as the temperature stability of nanogratings will be studied. These properties are not only relevant for the generation but also for application purposes of nanograting-based photonic devices.

3.1 Experimental methodology

3.1.1 Laser inscription

For the inscription of nanostructures in the bulk of fused silica various laser setups were used. The experimental approach for the inscription, however, is mostly similar: An ultrashort laser source emits pulses with pulse durations of a few ps down to the subpicosecond range at wavelengths ranging from 515, 800, 1030 up to 1550 nm. Polarization optics such as half-wave plate and polarizer serve to adapt the laser pulse energy. The laser pulse repetition rate (R) can be tuned with an (external or internal) acousto-optical modulator and the direction of the linear polarization is set by a half-wave plate. To focus the pulses in the bulk aspheric lenses with numerical apertures (NA) from 0.1 up to 0.6 are used.

The size of the modification (D) is determined in a first approximation by the spot size and can be approximated along the direction transversal to the inscribing laser beam with $D=2\omega_0=2\lambda/(\pi NA)$, with ω_0 being the beam waist radius given by the laser wavelength

and the NA of the objective. The pulses are focused in shallow material depths (150-200 µm; depending on the objective) where spherical aberrations are still small. High-precision translation stages (Aerotech) serve to inscribe single spots or extended regions such as single lines (for SEM inspection) up to two- or three-dimensional structures (for retardance measurements or wave plates) while the speed of the sample movement (v) varies from less than 1 µm/s up to several tens of mm/s. The formation of nanostructures strongly depends on the pulse overlap while the corresponding discrete pulse number effectively incident on one laser spot N_p corresponds to $N_p = D \cdot R/v$. When inscribing multiple traces the line separation was set to avoid overlapping of individual traces.

3.1.2 Characterization of nanostructures

The laser-induced nanostructures are buried within the bulk glass and exhibit feature sizes smaller than the wavelength of light. Thus, the modified region is not directly accessible and challenging to evaluate noninvasively. One intuitive approach is the macroscopical analysis of the induced birefringence by measuring their amount (optical retardance) and slow axes orientation. For this purpose a commercial strain analyzer (Ilis StrainMatic M4/60.13) was used in this work. Within the setup the birefringent sample is illuminated by linear polarized laser light (wavelength 587 nm) that in general changes to an elliptical polarization state by passing through the sample. Subsequently, the ellipticity is analyzed by a subsequent quarter wave plate and a rotating analyzer measuring the shift in polarization angle which is proportional to the optical retardance. To evaluate both the orientation of the slow axes as well as the retardance magnitude typically several incident polarization states are used. The resulting retardance can be determined with an accuracy of 0.1 nm while multiple measurements of nanograting samples inscribed with the same laser parameters, however, revealed a statistical error of 1 nm.

The spatial resolution of 9.9 µm is larger than the typical size of a single spot. Thus, several lines were inscribed next to each other (while avoiding an overlap of traces) with a total size of several hundreds of µm and the averaged retardance was measured. A comparison with the retardance gained by a microscopical retardance device (Abrio PolScope, CRi Inc.) revealed good agreement.

To visualize the nanograting structure scanning electron images (SEM) were acquired. To this end, the laser focus was scanned through the glass slightly tilted with respect to the longitudinal position (z) to uncover also depth information. Afterwards the sample

was mechanically polished and etched in 1 % hydrofluoric acid for 90 s and coated with gold to prevent charge accumulation. Based on the porous structure of nanogratings (see Chapter 4) the increased etch rate yields the coarse structure of nanogratings such as large pores and their distance (period).

3.1.3 X-ray scattering

One of the key challenges for the experimental investigation of nanogratings is the structural analysis. Common methods rely on polishing, etching or cleaving of laser-irradiate samples which destroy fine structural features and, when imaging with SEM, only reveal information about arbitrary spatial cross sections. These drawbacks can be overcome by small-angle X-ray scattering (SAXS), which is well suited to study density inhomogeneities within an isotropic material background with resolution down to the nanometer scale [78, 79]. This can be done in a contactless and nondestructive fashion while the modifications of interest are still buried in the glass. While SAXS is sensitive to the electronic density contrast of objects larger than single atoms wide-angle X-ray scattering (WAXS) covers correlations on atomic scale and may serve to evaluate laser-induced strain based on changes of the atomic bond distances. This allows for studying different stress states, e.g. due to glass quenching or complex morphological changes.

Small-angle X-ray scattering (SAXS)

The theory of X-ray scattering goes back to the classical description of scattering by Thomson and Debye [80, 81]. This considers only elastic light scattering at particles with the scattering vector:

$$\mathrm{q} = \frac{4\pi}{\lambda} sin(\theta), \tag{3.1}$$

(with θ being the scattering angle) while multiple scattering processes are neglected (see Fig. 3.1 (a)) [78]. The scattering amplitude is proportional to the Fourier transformation of the electron density distribution $\rho(r)$ and hence directly provides structural information of the probed sample. SAXS is sensitive to the local scattering contrast $\Delta\rho(r) = \rho(r) - \rho_0$ while scattering from an isotropic background (density ρ_0) only adds at q=0.
Commonly used to probe suspended nanoparticles [82, 83] SAXS can, due to the reciprocity of the scattering process, also be applied to analyze material inhomogeneities

such as empty voids in an isotropic glass matrix. While the scattering vector q (see Equation 3.1) defines the angle region for the feature sizes of interest, the probe wavelength is typically set by considering experimental issues such as the attenuation of the X-ray beam by passing through the sample. Thus, for thick glass samples of several hundred µm short wavelengths ($\lesssim$ 1 Å) are preferred. Depending on the geometry and the instrumental resolution scattering within the q-range from 10^{-3}–10^{-1} Å^{-1} (θ=0.004° - 0.5°) is measured leading to resolvable feature sizes from a few nanometer up to some hundreds of nanometer. The scattering intensity I(q) per space angle element can be written as [83]:

$$I(\mathrm{q}) = r_e^2 N \left| \int_V \Delta\rho(r) exp(-i\mathrm{q}r) dr \right|^2 , \tag{3.2}$$

$$= r_e^2 N V^2 \Delta\rho^2 F^2(\mathrm{q}), \tag{3.3}$$

where r_e denotes the classical electron radius, N the number density of scattering particles within the probed volume and r is the three-dimensional scattering length. The spatial integration over the probed object (volume V) is called form factor F. If the shape of the probed particles is known, e.g. spherical objects, the known form factor can be used to derive the number or density and size of the probed particles.

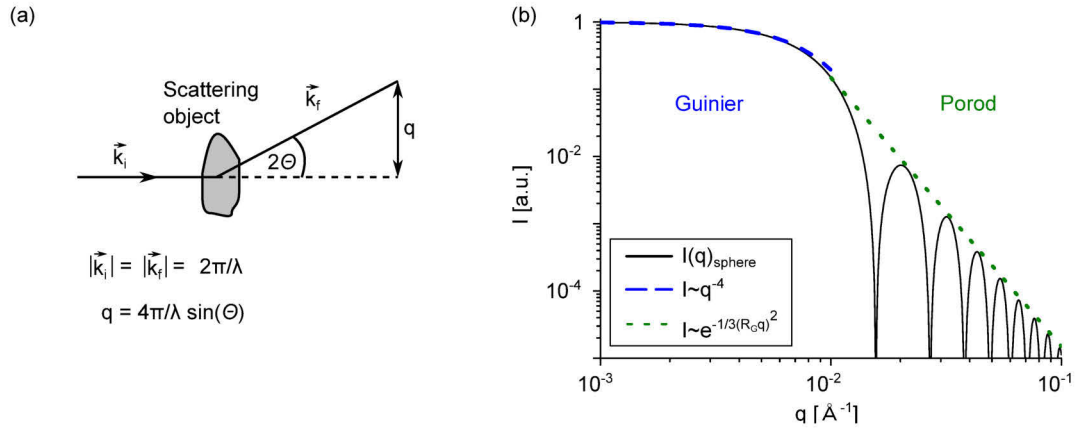

Fig. 3.1: (a) Sketch of the scattering process. (b) Calculated scattering intensity of an ideal sphere. Corresponding fits in the low-q and high-q region indicate the Guinier and Porod regime, respectively.

At an early stage Guinier noticed that differently shaped particles exhibit a similar trend of scattered intensity in the low-q range that can be approximated with a Gaussian func-

tion corresponding to G·exp($-q^2R_g^2/3$), where R_g is a parameter which accounts for the average size of the scattering object and G is a prefactor [78]. In contrast, at high-q values (Porod region) the scattered intensity decays with a power law $\sim B{\cdot}q^{-d_f}$ with d_f being a structural parameter and the constant prefactor B. Figure 3.1 (b) illustrates the calculated scattering intensity of an ideal sphere indicating both regions. Destructive interference leads to discrete zero points in the high-q range. In a real experiment these points vanish if the shape of the scattering object is not ideally spherical and/or the size of different objects varies (polydispersity). In the case of scattering objects with multiple size hierarchies (i) the so-called unified approach combines the Guinier and Porod regime to describe the total scattering response of the ensemble [84, 85]:

$$I_u(q) = \sum_i G_i\, exp\left(-\frac{q^2R_{g,i}^2}{3}\right) + B_i(q^*)^{-d_{f,i}}, \tag{3.4}$$
$$q^* = \frac{q}{\left[erf\left(6^{-1/2}qR_g\right)\right]^3} \sim q/R_g.$$

The error function erf defines the low-q cut-off to avoid divergent behavior. In the case of multiple structural levels the analysis of each level allows for determining the corresponding structural diameter (assuming spherical shape) $D = 2(5/3)^{1/2}R_g$, as well as d_f (for compact objects $d_{f,i}$=4 and $d_{f,i}$ <4 for objects with smooth density variations). Moreover, the prefactors of both terms in Equation 3.4 together with R_g serve to evaluate the size distribution of each particle level in terms of a polydispersity index (PDI):

$$\mathrm{PDI} = \frac{BR_g^4}{1.62G}. \tag{3.5}$$

For spheres with a defined size (monodispersity), the poldydispersity index is 1, while a value of 5.56 corresponds to log-normally distributed feature sizes [85]. A crucial parameter for evaluating the overall scattering response is the Porod invariant P [86, 85]:

$$P = \int_0^\infty I(q)r^2dr = 2\pi^2\Delta\rho^2\phi(\phi - 1), \tag{3.6}$$

with ϕ being the particle filling fraction. For a porous material with a filling fraction $\phi \ll 1$ the Porod invariant is proportional to the total pore volume. Correspondingly, P provides the total scattering strength (number of scattering objects) of the probed particle ensemble.

Wide-angle X-ray scattering (WAXS)

X-ray scattering under wide-angles is sensitive to the atomic configuration in the glass network, i.e. the atomic pair correlation function [87, 88]. This covers a q-range from 0.5-4 Å^{-1}. Changes in the scattering such as a shift in the peak position or width of the diffraction peak represent the modified atomic rearrangement and provide information about the lattice parameters, defects or strain [89]. In fused silica a single correlation peak at 1.6 Å^{-1} is related to the next neighbor atomic distances (Si-O). In a first order approximation a change in volume is related to the nearest neighbor distances and represents the (remnant) strain e.g. due to laser irradiation.
However, an absolute strain value requires calibration of the scattering change $\frac{dS}{dT}\big|_p$ which is related to $\frac{dS}{dV}\big|_T$ via the linear coefficient of expansion, where $S = S(\mathrm{q})$ is the wide-angle scattering intensity, T denotes the temperature, V the volume and p the pressure. By using the linear expansion coefficient of silica ($5.7{\cdot}10^{-7}$ K^{-1} [90]) the averaged strain within the probed glasses can be derived. Since the relation of scattering change to strain is linearly approximated the corresponding scattering contribution is an additive function. Thus, if only a part of the volume exhibits strain the local strain is higher than the derived strain by the relative volume contribution of the irradiated part assuming a monotone strain distribution.

3.2 Influence of relevant laser parameters

Based on the current state of knowledge first the influence of relevant laser and process parameters on the nanograting formation is investigated. Starting from the most promising theoretical approach, the nanoplasmonic model, the prediction of the nanograting period on the laser wavelength will be analyzed. Nanogratings are known to assemble during the action of several hundreds of laser pulses. Thus, the corresponding period and optical retardance in dependence of the number of laser pulses is studied subsequently. Moreover the temporal pulse sequence may regulate the effect of laser-induced defects and hence

the feedback mechanism from pulse to pulse to form a regular nanograting. Finally, the laser pulse intensity denotes a crucial parameter for the underlying nonlinear absorption mechanism. Consequently, by varying the focusing, the laser pulse energy and the pulse duration allows for evaluating the corresponding nanograting threshold.

3.2.1 Laser wavelength and pulse number

When changing the inscribing laser wavelength while keeping the number of laser pulses per spot fixed (here 10^3) the average distance of the grating planes increases nearly linear and agrees with the predicted period ($\Lambda/2n$) as shown in Figure 3.2. The inset depicts two exemplary SEM images of nanogratings inscribed at 515 nm and 1550 nm indicating that mainly the distance of grating planes increases rather than the size of the planes. However, due to the etching process no detailed view on the size of grating planes can be given at this stage.

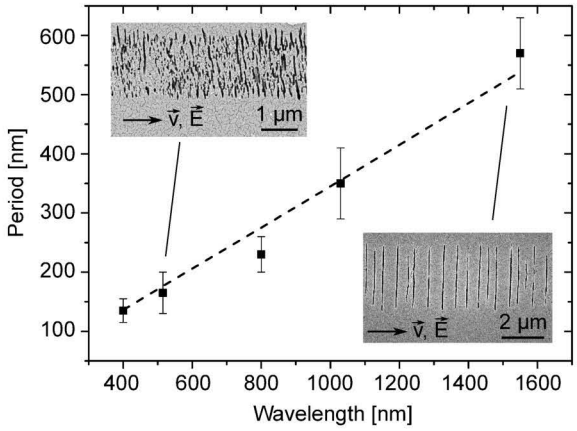

Fig. 3.2: Nanograting period in dependence on the wavelength of the inscribing laser. The dashed curve represents the predicted period ($\Lambda = \lambda/2n$) by the nanoplasmonic model considering the material dispersion [91].

Smaller inscription wavelengths facilitate pronounced absorption due to the reduced number of photons required for multiphoton absorption (e.g. 4 photons at 515 nm instead of 8 photons at 1030 nm to bridge the bandgap of 9 eV). Consequently the threshold for the formation of nanogratings is slightly higher at larger wavelengths [92]. In contrast the slightly higher optical retardance at 515 nm as well as the fact, that the threshold is independent on the pulse number affirms that nonlinear absorption plays a minor role in the underlying formation mechanism [92].

The formation of strong birefringence due to nanogratings requires a sufficient laser pulse overlap during inscription. When scanning the laser focus through the glass and keeping the focusing objective fixed the overlap can be set by either varying the speed of the sample movement or the laser repetition rate, respectively. However, to avoid defect or heat mediated effects due to changing temporal pulse spacing, the variation of the sample movement provides a reasonable way to set the number of applied laser pulses effectively incident on one laser spot.

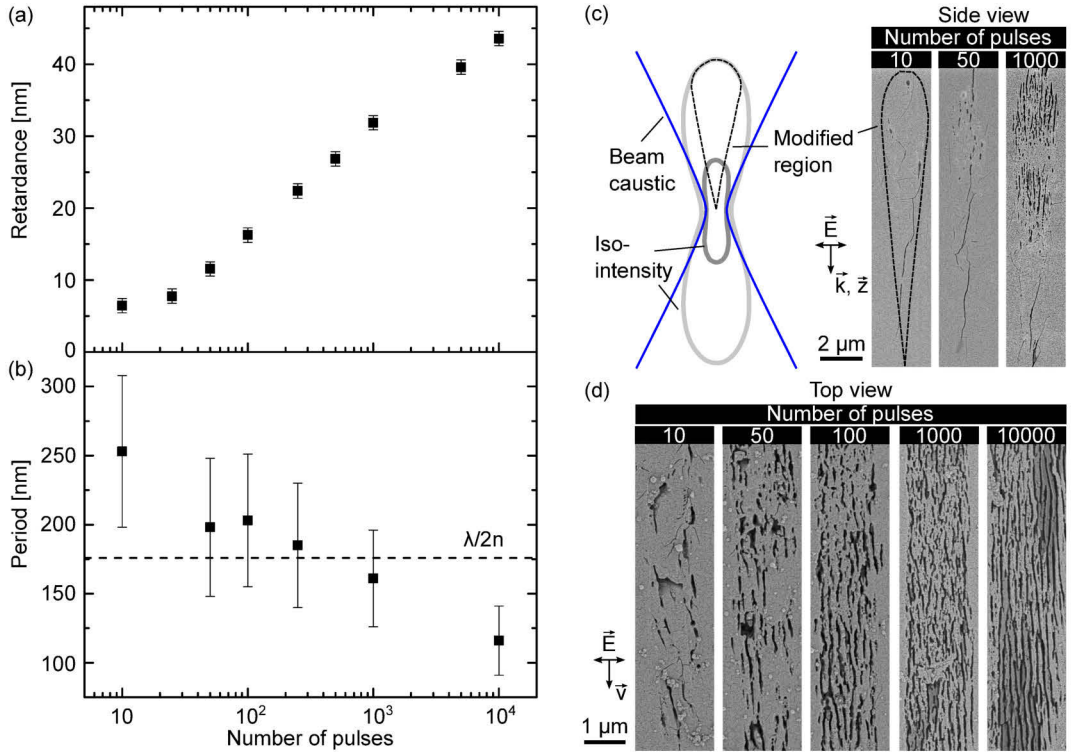

Fig. 3.3: (a) Optical retardance and (b) nanograting period in dependence of the number of applied laser pulses. (c) Sketch of the longitudinal intensity distribution (iso-intensity lines and the beam caustic is shown) as well as SEM images along the direction of the inscription laser and (d) along the transversal direction. The laser wavelength was 515 nm, the repetition rate 500 kHz and the laser pulse energy 190 nJ.

Figure 3.3 (a) shows the optical retardance which increases in a logarithmic fashion from about 25 pulses per spot. The consecutive irradiation triggers a strong change in the overall grating properties (see Fig. 3.3 (b-d)): Most conspicuous, the number of grating planes increases which is the structural equivalent of growing retardance. During this evolution the order increases and a highly periodic grating is formed. The grating planes are mainly

located above the laser focus and arranged within a tear-drop shaped modification region. Due to the spatially moving breakdown towards the incoming irradiation [93, 94], the modified region in principle follows the iso-intensity lines of the laser pulse.
The average distance of grating planes (period) decreases with ongoing irradiation while the deviation from the mean value shrinks as well (Fig. 3.3 (b)). Intriguingly, even smaller periods as predicted by the nanoplasmonic theory ($\Lambda/2n$) are measured in agreement with observations from other groups [95, 96]. Although the macroscopical retardance depends on the period (see Equation 2.4) the strong rise in birefringence can not only be explained by this reduction. The increase in number of grating planes also leads to a higher refractive index contrast. However, a more detailed view will be given in Chapter 4. Still, the clear evolution of a well-ordered nanograting accompanied by strong retardance denotes the number of pulses as important parameter for the formation mechanism.

3.2.2 Temporal pulse sequence

The evolution from random nanostructures towards a regular arranged grating requires the cumulative action of several hundreds of laser pulses given a delicate feedback mechanism. Besides the effective pulse number per laser spot the temporal pulse sequence is defined by the laser repetition rate. The laser-induced birefringence basically develops below a repetition rate of 1 MHz for fused silica (see Fig. 3.4). Interestingly the maximal retardance shifts to smaller repetition rates for increasing laser pulse energy. This is a consequence of increasing temperatures the larger the pulse energy becomes. The laser-induced heat can not fully diffuse in between two successive pulses, that results in heat accumulation setting in at lower repetition rates [43, 52, 97]. This means that even at very low pulse energy (e.g. at 50 nJ) weak form-birefringence can be induced at high repetition rates beyond 1 MHz [98]. Intriguingly, the short pulse separation seems to be even beneficial for the nanograting formation since the retardance increases with the repetition rate at low pulse energy of about 50 nJ which is most likely due to transient defects (see Section 3.3) [99]. For application purposes, however, the benefit due to the high repetition rate (and hence possible scanning speed) can not compensate for the weak birefringence.
Moreover, another interesting approach is to use ultrashort pulse trains consisting of a few laser pulses with high repetition rate and comparatively long time in between these trains (so-called bursts) instead of a continuous pulse train at constant repetition rate (see Fig. 3.5). This can be achieved e.g. by an acousto-optical modulator which continuously picks

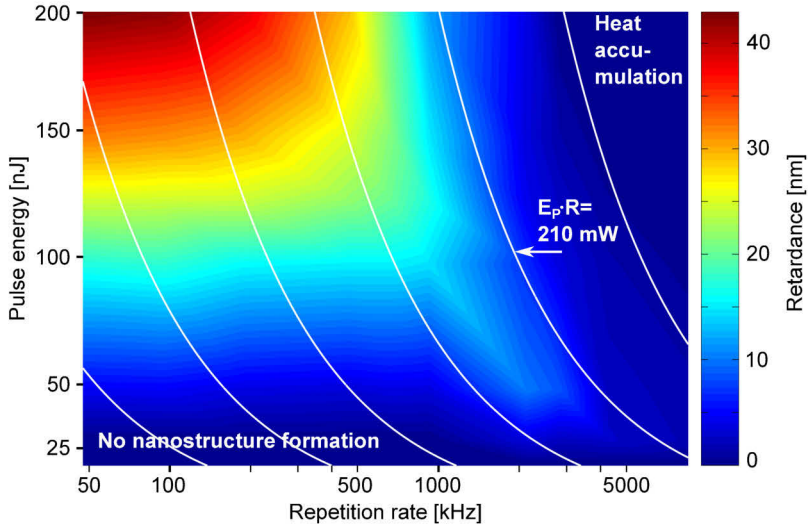

Fig. 3.4: False-color map of measured retardance as function of repetition rate and pulse energy. The upper threshold for nanograting formation follows regions of constant average laser power (white lines). Depending on the retardance value the threshold is around 210 mW (E_P - pulse energy, R - repetition rate). The laser wavelength was 515 nm, the pulse duration 450 fs, the number of laser pulses per spot was kept constant at 10^3 and the numerical aperture of the objective was 0.55.

a certain number of pulses with a repetition rate R_L to generate femtosecond laser bursts with a burst repetition rate R_B. When applying bursts for the inscription of nanogratings two regimes can be distinguished (see Fig. 3.6 (a)). The burst inscription was performed

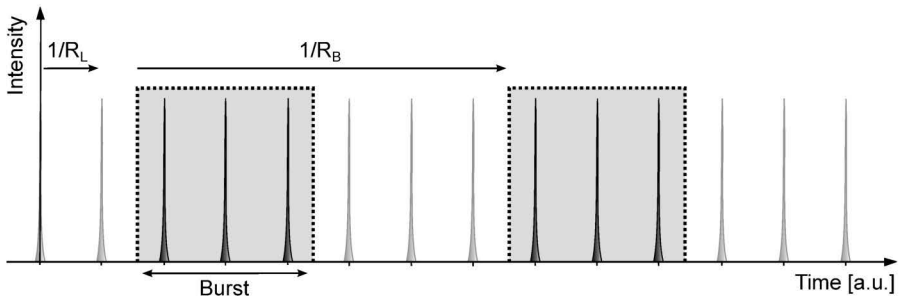

Fig. 3.5: Laser bursts can be generated e.g. by an acousto-optical modulator which picks a certain number of pulses pulses with an initial laser repetition rate R_L. In that way femtosecond laser bursts with a repetition rate of R_B are created.

using a fixed laser repetition rate of R_L=9.4 MHz and a burst repetition rate of R_B=10 kHz while changing the number of laser pulses within a burst to stepwise increase the average laser power. To compare with continuous pulses at the same average power the repetition

rate was stepwise increased (e.g. continuous pulses at 20 kHz compared with two-pulse Bursts at R_B=10 kHz).

When the number of laser pulses within a burst is between two and four higher birefringence is measured compared to continuous pulses (see Fig. 3.6 (a)). The short time in between the pulses within a burst of 106 ns facilitates pronounced absorption due to laser-induced bond-type defects from the previous pulse(s) [99, 100, 101]. The relaxation of excited electrons includes the formation of self-trapped excitons (STEs) which decay within several hundred picoseconds into point defects via several decay channels (see Section 3.3).

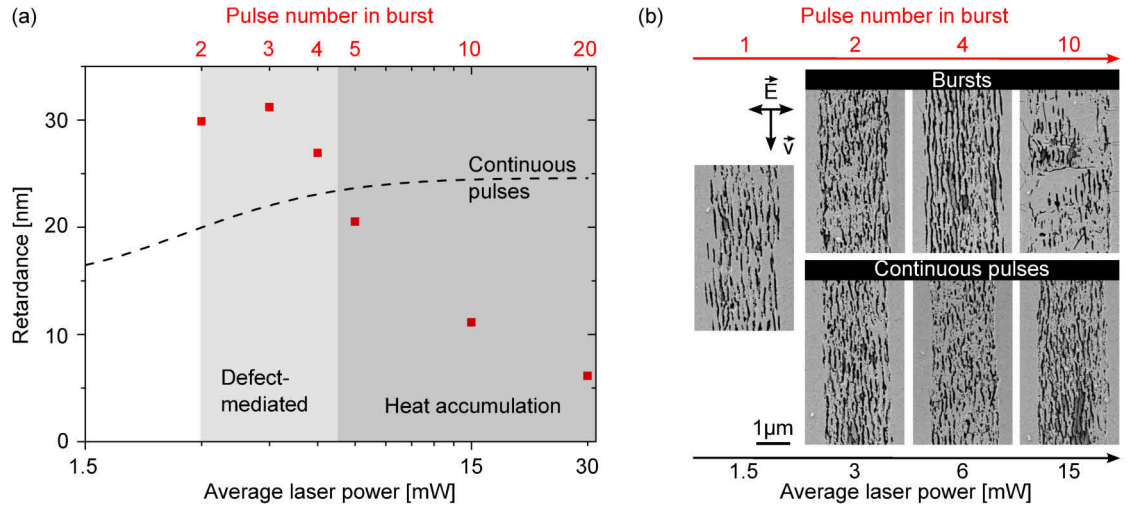

Fig. 3.6: (a) Retardance of laser-induced nanogratings inscribed with bursts with different laser pulse numbers within a burst and (dashed) with continuous pulses. For continuous pulses the average power was set by the laser repetition rate keeping the individual pulse energy. (b) SEM images for nanogratings inscribed with continuous pulses and bursts using a laser wavelength of 515 nm, a pulse energy of 150 nJ and an objective with a numerical aperture of 0.55.

Thus, transient defects facilitate the formation of nanostructures when using bursts as the SEM images in Figure 3.6 (b) show. In particular at four laser pulses a wider modification zone is obtained representing the structural equivalent of higher birefringence.

By further increasing the number of pulses within a burst elevated temperature due to heat accumulation disturbs the sequential grating formation and erases nanometric modifications. Correspondingly, the measured retardance decreases rapidly. For continuous pulses (dashed curve in Fig. 3.6 (a)) the birefringence slightly increases with average power (repetition rate) in contrast to Figure 3.4. This is due the constant velocity of the sample

movement (0.06 $\frac{mm}{s}$) and hence increasing number of laser pulses per spot. Heat accumulation sets in at higher repetition rates above 200 kHz at a pulse energy of 150 nJ (see Fig. 3.4).

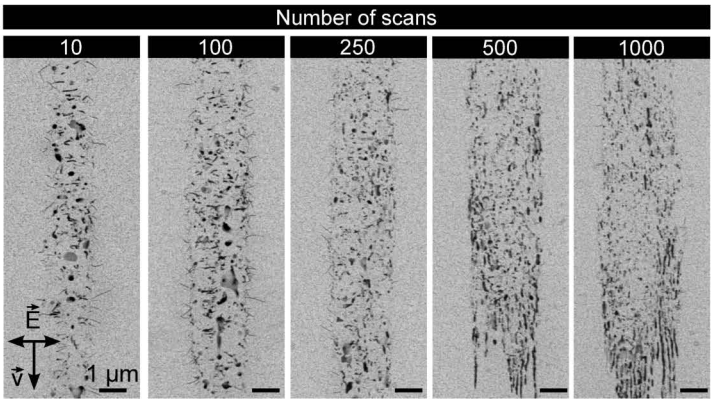

Fig. 3.7: SEM images of nanostructures inscribed at a laser wavelength of 515 nm, repetition rate of 10 kHz and pulse energy of 150 nJ. Please note that the structures were inscribed at constant scanning speed of 60 mm/s corresponding to 1 pulse per spot only varying the number of individual scans.

The result of defect-assisted absorption becomes even more apparent when scanning the laser focus at constant velocity without spatial overlap (e.g. at high velocity of 60 mm/s that corresponds to 1 pulse per spot) and varying the number of scans. This means that, due to the lack of synchronization between the laser pulses and the positioning system, the spatial position of the incident laser pulses varies for each individual scan. However, although for several scans the laser pulses spatially overlap the temporal overlap is small due to the time in between two individual scans of about 20 ms.
The process of grating formation is strongly delayed as the SEM images in Figure 3.7 shows. Only after more than 500 individual scans regularly ordered grating planes start to appear. This approach reveals that nanogratings can be inscribed even at very low pulse repetition rate. However, laser-induced defects influence the feedback process from pulse to pulse.

3.2.3 Pulse energy and duration

Nonlinear absorption and the subsequent generation of free electrons strongly depends on the pulse intensity reached within the focal volume. Hence the formation of nanostructures is linked to the pulse energy that exceeds a certain threshold, e.g. about 20 nJ at a

pulse duration of 450 fs and a laser wavelength of 515 nm (NA of the focusing objective 0.5). Figure 3.8 (a) shows corresponding SEM images of nanogratings in top and side view. Both image sequences illustrate the formation of regularly ordered grating planes which extend over an increasing spatial cross section with growing pulse energy. As indicated in Figure 3.3 (c), the modified (tear-drop shaped) region follows the iso-intensity lines of the focused laser pulse. Thus, as the pulse energy increases, the modified region becomes larger confirming that the threshold for nanograting formation depends on the laser intensity [102].

Structural characteristics such as the period hardly change with varying pulse energy. Thus, the retardance mainly increases due to the larger modification region as Figure 3.8 (a) shows. The measurements of the retardance (see Fig. 3.8 (b)) were performed using a constant pulse overlap of 10^3 pulses per spot using different focusing objectives with a numerical aperture (N.A.) varying from 0.16 to 0.55. As the numerical aperture defines the size of the spot and hence the laser intensity reached within the focus the energy threshold for nanostructure formation decreases with the numerical aperture. The

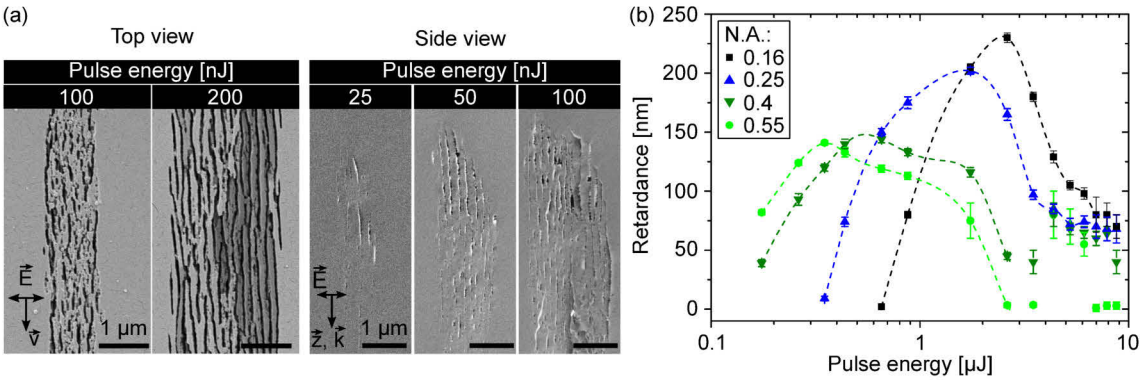

Fig. 3.8: (a) SEM images in top and side view after polishing and etching (top view) and cleaving (side view), respectively. The laser wavelength was 515 nm, the pulse duration 450 fs, the repetition rate 500 kHz and an objective with a numerical aperture of 0.55 was used. (b) Optical retardance of nanogratings inscribed with fixed pulse number per laser spot of 10^3 at 1030 nm, 200 kHz repetition rate for different objectives (N.A. - numerical aperture) used in dependence of the laser pulse energy. The dashed lines represent a guide-to-the-eye for the parameter regime where nanostructures can be obtained.

maximal birefringence reached is limited by the size of the focus which primary scales with the focusing. Finally, at high laser pulse energy of a few µJ nanograting formation is prohibited due to strong material damage (e.g. cracks) [103, 104]. This damage comes along with stress-birefringence that scales with the size of the modification (inversely with

the numerical aperture of the focusing objective) explaining the increasing retardance plateau with lower numerical aperture.

The false-color plot in Figure 3.9 (a) depicts the measured optical retardance for nanostructures inscribed at a laser wavelength of 1030 nm, a repetition rate of 200 kHz using a numerical aperture of 0.25. By increasing the laser pulse duration the region of pulse energies, where nanostructure formation occurs, shrinks significantly. For shorter pulse durations the threshold for strong birefringence follows the region of constant peak power and (since the objective remained constant) peak intensity, respectively. Below a peak power of 9 MW (corresponding to a peak intensity of 170 TW/cm^2) the retardance increases with increasing pulse duration up to 250 nm at a pulse duration of 1.8 ps. However, strong damage occurs for ps pulses at high pulse energies most probably due to increased heating of the lattice which in turn leads to higher thermal load of the glass network resulting in accumulation of stress and cracking of the glass. For pulse durations of several ps the lattice is heated more efficient due to the electron-phonon scattering time of about 1 ps [45, 50]. Thus, both the lower intensity as well as pronounced thermalization prohibits nanostructure formation.

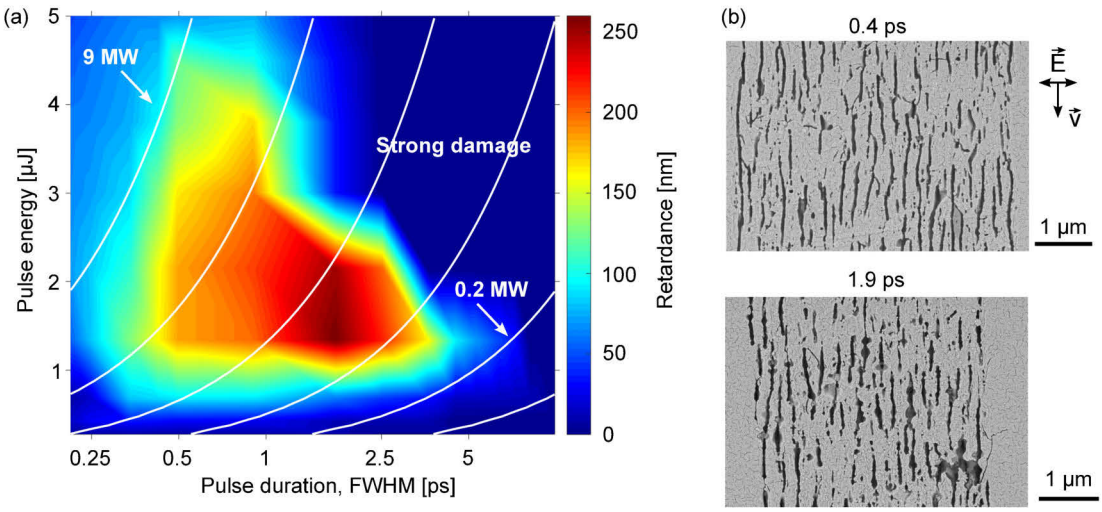

Fig. 3.9: (a) False-color map of the optical retardance of nanogratings in dependence of the laser pulse duration and pulse energy. The laser wavelength was 1030 nm, the repetition rate 200 kHz and the numerical aperture of the focusing objective 0.25. The white lines represent regions of constant laser peak power. (b) SEM images of nanogratings inscribed with a laser wavelength of 1030 nm, a pulse energy of 1.5 µJ and a numerical aperture of 0.55 but different pulse durations.

For smaller pulse durations as 400 fs the generation of free electrons via avalanche ionization becomes less effective and hence due to the reduced heating of free electrons by collisions the efficiency of nanostructure formation drops [105]. As a result the pulse energy threshold increases with decreasing pulse duration (see Fig. 3.9 (a)) [26].
With respect to the structural properties of nanogratings varying the pulse duration does not change the main characteristics such as the period (see Fig. 3.9 (b)). However, due to the reduced intensity at higher pulse duration smaller modification zones are obtained. Thus the optical retardance is lower at 1.9 ps (66 nm) as for 0.4 ps (115 nm). This is in contrast to Figure 3.9 (a) due to the higher numerical aperture of 0.55 and hence higher peak intensity which causes thermal affects to appear earlier.

3.3 Laser-induced defects and temperature stability

Beyond the basic absorption of ultrashort laser pulses, the formation of nanostructures in the bulk of glasses comprises complex mechanisms: Laser-induced bond breaking causes transient and permanent defects while glass chemical processes such as rapid quenching of the glass matrix leads to changes of the glass density (and fictive temperature) as well as stress within the laser affected region and beyond. While defects mediate the feedback process to form a regular nanograting in the first place these also affect optical properties such as losses due to absorption and scattering at the induced nanostructures. These losses have to be taken into account in the framework of photonic applications such as optical components. Furthermore, laser-induced stress both due to the quenched glass matrix as well as induced by nanoscopic voids may influence the mechanical durability of nanogratings.

3.3.1 Point defects

The absorption of ultrahort laser pulses via nonlinear absorption mechanisms is accompanied by the formation of self-trapped excitons (STEs) which form within a few hundred fs [106]. The excited electrons relax into these STEs based on electron-phonon coupling on timescales of a few ten ps [107, 95, 106]. Subsequently, relaxation of the electrons may occur radiatively with a lifetime of ns (at room temperature) or non-radiatively by coupling with lattice phonons. The latter facilitates structural modification such as den-

sification and corresponding changes of the fictive temperature. Another option albeit exhibiting small yield [108] is the relaxation into point defects [95, 99].

To characterize these laser-induced defects the absorption spectra of nanogratings were measured using a commercially available spectrometer (Perkin Elmer Lambda 950). To this end patterns with a size of 5 x 5 mm^2 were inscribed at a laser wavelength of 515 nm, a pulse energy of 200 nJ and 100 kHz repetition rate. Subsequently the samples where annealed 2 h at constant temperature and the transmission as well as reflection spectrum (T_S and R_S) were measured.

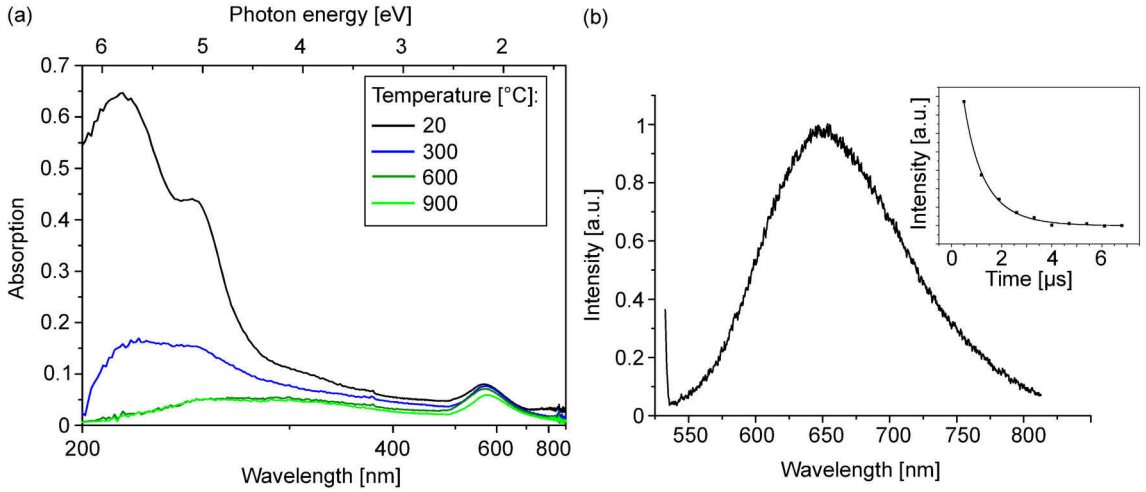

Fig. 3.10: (a) Absorption spectra of laser-induced nanostructures after different annealing steps and (b) photoluminescence (PL) of nanostructures (not annealed) using an excitation wavelength of 532 nm. The inset shows the time-dependent PL decay due to bleaching of NBOHCs. For (a) and (b) the background from the pristine glass was subtracted.

Figure 3.10 shows the absorption spectra (A=1-T_S-R_S) indicating distinct peaks while the pristine glass exhibits no significant features within the investigated range. The peaks can be associated with dangling bond type defects: The first feature at 212 nm (5.85 eV) is due to silicon dangling bonds (so-called $E^{'}$-centers) whereas the peaks at 248 nm (5.1 eV) and 652 nm (1.9 eV) correspond to non-bridging oxygen hole centers (NBOHCs) [109, 110, 111]. The latter are known to exhibit strong photoluminescence (PL) at 650 nm (1.9 eV) as Figure 3.10 (b) shows [112]. By continuous excitation the PL signal decays over time following a stretched exponential distribution $\exp(-(t/\tau)^{\beta})$ as expected for distorted media [113, 114]. The lifetime of NBOHCs is τ =(41 ± 2) µs with a stretching factor β=0.64 ± 0.14 which is larger than the lifetime in pristine silica of 13 µs [115]. The

observation of a non-exponential decay, however, indicates the disordered glass matrix after irradiation reflecting the modified distanced distribution of defects involved [113]. The NBOHCs [≡Si-O•] and E'-centers [≡Si•] may recombine further into peroxy linkage [≡Si-O-O-Si≡], form a peroxy radical [≡Si-O-O•] or end up in an oxygen deficiency center SiODC(II) [=Si••] together with molecular oxygen (O_2) [33, 106, 111]. This oxygen can be captured in small voids or may exist dissolved within the silica network and can be measured by Raman spectroscopy (see Section 3.3.3).
When annealing the laser-irradiated samples mainly the peak attributed to E'-centers at 212 nm decreases which agrees with the temperature decay reported in [116]. NBOHCs remain almost stable after an initial decay due to recombination with hydrogen.

3.3.2 Temperature stability

In contrast to the decay of laser-induced defects the induced nanostructures are highly temperature stable as Figure 3.11 (a) shows. The measured retardance significantly starts to decay after annealing for one hour at 800°C. Even after annealing to 1,100°C one third (depending on the pulse energy) of the initial retardance remains. However, the laser-induced structures such as small voids (see Chapter 4) start to vanish due to microscopic flow of glass above the strain point of fused silica (1000°C [117]) [30]. Thus, less scattering leads to increasing transmission as observed in the microscope images of Figure 3.11 (b).

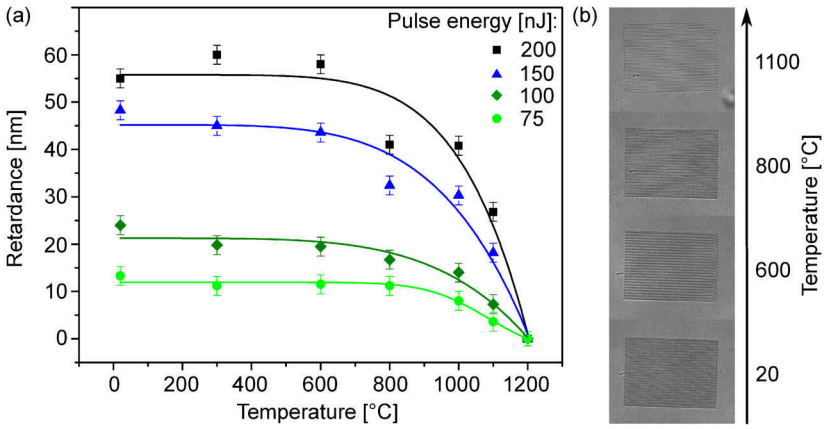

Fig. 3.11: (a) Optical retardance of nanostructures (the solid lines represent a guide-to-the-eye) and (b) bright field microscope images after different annealing steps (the specified temperature was kept constant for 1 h). Please note that the brightness of the background in (b) is the same for all images.

In case of repeated annealing the retardance is stable up to 850°C with respect to the value after single annealing. Since the measured retardance is due to both stress and form-birefringence, most likely stress is annealed while the underlying nanostructure remains stable up to this temperature. Thus, for application purposes single annealing might be preferential to increase the (thermal) durability of photonic functionalities.

3.3.3 Mesoscopic network changes

The local absorption of ultrashort laser pulses and subsequent thermalization leads to increasing temperature which can reach several thousand Kelvins [51, 118]. Due to the short pulse duration the lattice rapidly cools with typical cooling rates > 10^6 K/s increasing the fictive temperature (see Fig. 2.1). This is accompanied by network changes both on mesoscopic, i.e. affecting the ring structure of SiO_4 tetrahedrons, and microscopic length scales such as variations of atomic bond distances. Both affect the nanostructure formation since the density change leads to stress within the heat affected region as well as in the surrounding [119, 97]. Accumulated stress may lead to crack formation prohibiting a regular assembling of nanogratings as obtained e.g. for large pulse durations (see Section 3.2.3).

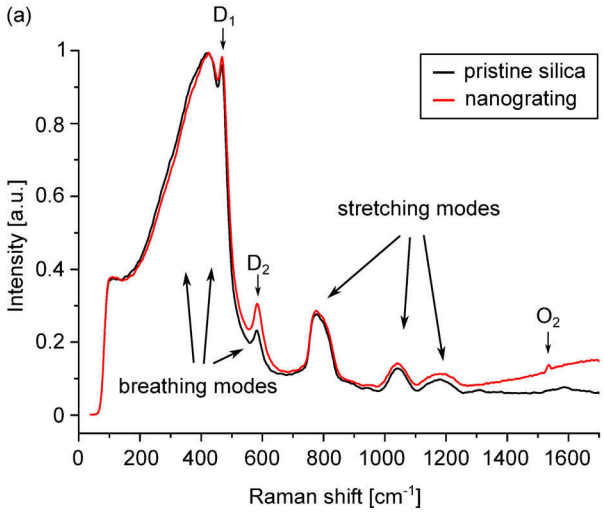

Fig. 3.12: Raman spectrum of pristine fused silica and nanogratings (red) measured with an excitation wavelength of 478 nm. The spectra are normalized to the intensity of the main band at 430 cm^{-1}. At high wavenumbers the increasing background is due to weak photoluminescence excitation of NBOHCs (see Fig. 3.10).

In order to analyze these network changes Raman spectra of irradiated silica were acquired using a commercially available Raman spectrometer (Renishaw, inVia Raman

Spectrometer) with an excitation wavelength of 473 nm and an objective with a NA of 0.4 (magnification 20x). The notch filter had a transmission cut off at 100 cm^{-1}.
The Raman spectrum of pristine silica is shown in Figure 3.12. The 3D arrangement of SiO_4 tetrahedrons forming Si-O-Si bridges exhibits a well-defined vibrational fingerprint [120, 121]. Distinct peaks corresponding to stretching, bending and collective modes exist. The spectrum is characterized by the signature of different membered rings of SiO_4 tetrahedrons and their different number of linkage.
Within the spectrum of pristine silica (see Fig. 3.12) the main band at 430 cm^{-1} is due to Si-O-Si breathing modes of multiple membered silica rings. While the main peak is most likely attributed to six-fold rings, five-, seven- or even higher membered rings broaden this band [122]. The defect bands at 495 cm^{-1} and 605 cm^{-1} are called D_1 and D_2 and correspond to breathing modes of four and three planar silicon-oxygen rings. The Raman bands at higher wavenumbers correspond to stretching modes of the Si-O-Si network.

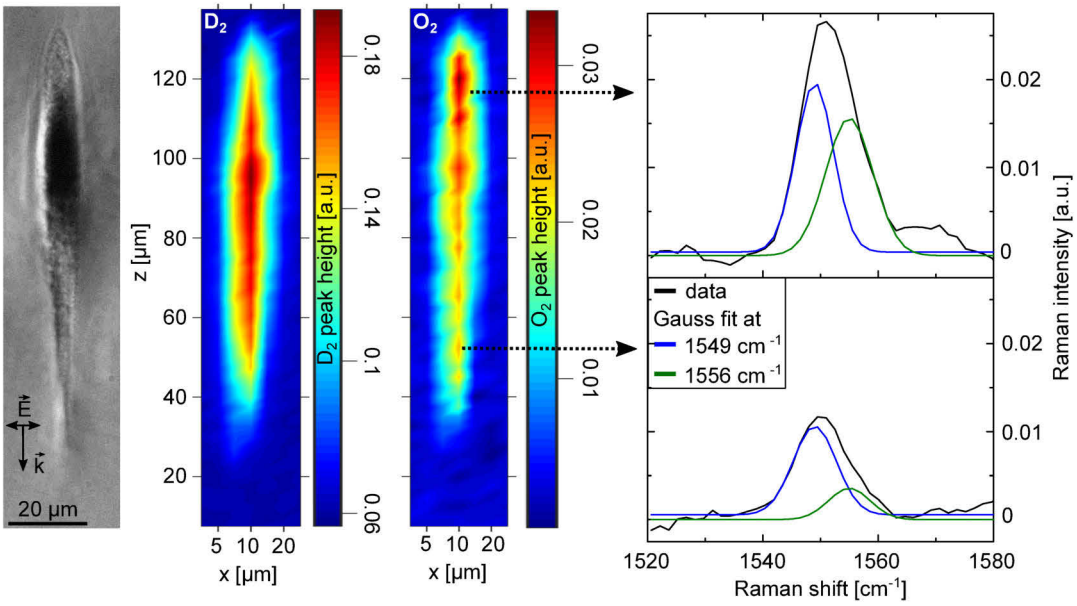

Fig. 3.13: Dark field microscope image of nanogratings and false-color map of the relative peak height of the D_2 and O_2 band. The graph on the right shows the exemplary oxygen signature at two different positions (indicated by the arrows) and the deconvolved Gaussian fits of the dissolved (1549 cm^{-1}) and free (1556 cm^{-1}) oxygen band. For inscribing the nanogratings the laser wavelength was 1030 nm, the repetition rate 200 kHz, the pulse duration 380 fs and the pulse energy 3 µJ.

When irradiating with ultrashort laser pulses only a few features within the spectrum change indicating the slightly modified network arrangement. For the spectrum shown in

Figure 3.12 (red curve) nanogratings were inscribed using a laser wavelength of 1030 nm, a repetition rate of 200 kHz, a pulse energy of 1.3 µJ and a scanning speed of 0.5 mm/s. Most striking is the increase in the D_1 and D_2 defect bands. These are known to increase with fictive temperature [35, 36] and have been measured after irradiation with femtosecond laser pulses [38, 55]. Correspondingly the number of three- and four-fold silicon oxygen rings is increased which comes along with a peak shift to larger wavenumbers and thus a decrease in average bond angle both of D_1 and D_2 [123]. However, due to the Raman beam spot size of about 0.8 µm compared to the feature size of nanogratings (e.g. the period of a few hundred nanometers) no detailed information on the nanoscopic structural modification is gained. Still, the measurement of the defect bands reveal that the nanostructure is embedded in a heat affected and densified glass (since rapidly quenched) with a network structure that is still intact but with larger fictive temperature.
Figure 3.13 shows the spatial distribution of the D_2 peak height (after background subtraction and fit assuming a Gaussian peak shape) for the cross section of a laser modified region. Compared to the microscope cross section D_2 increases towards the center following the tear drop shaped modification region. Within the center the highest temperatures are reached leading to a larger fictive temperature after cooling.

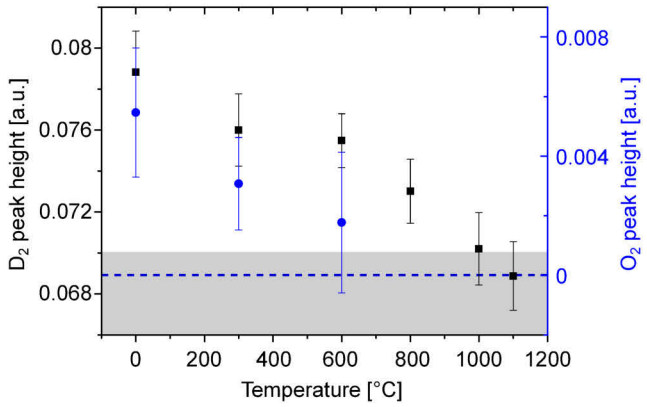

Fig. 3.14: D_2 (black squares, left axis) and O_2 (blue circles, right axis) relative peak height as function of the annealing temperature (the isochrones lasted 1 h). The gray shaded area represents the D_2 band and the blue dashed curve the O_2 value of pristine silica. For inscribing the laser wavelength was 1030 nm, the repetition rate 200 kHz, the pulse duration 380 fs and the pulse energy 3 µJ.

Intriguingly, two close peaks located at 1549 cm^{-1} and 1556 cm^{-1} appear in the spectrum of the irradiated glass (see Fig. 3.12). While the first band is due to dissolved oxygen (O_2) within the silica network [124] the second band can be attributed to free oxygen

(O_2) [125, 95]. The presence of both peaks is a signature of the laser-induced bond breaking and subsequent relaxation process: During the formation of dangling bond type defects oxygen is generated that may recombine to molecular O_2. This oxygen may remain trapped within the silica network or within small cavities - the primary constituents of nanogratings (see Chapter 4). The common Raman band appears along the cross section of the laser modified glass (see Fig. 3.13). However, the largest peak heights are located in the head of the modification zone where nanogratings are found. Within this region both oxygen signatures almost equally contribute to the Raman band. In contrast, mostly dissolved oxygen is measured at the tail of the modification that is most likely due to less nanostructures in this region [95].
When annealing the samples for one hour at constant temperature both the O_2 and D_2 peaks decrease in height as Figure 3.14 shows. Oxygen can be measured until 300 °C while the increasing oxygen mobility with temperature may facilitate the recombination with dangling bonds such as $E^{'}$-centers [≡$Si^{\bullet}$], e.g. to form a peroxy radical [≡Si-O-$O^{\bullet}$]. In contrast, the increased D_2 signal only vanishes at temperatures above 1000 °C where the annealing time is in the range of the glass relaxation time [126].

3.3.4 Network changes on atomic scale: laser-induced strain

Besides the change on mesoscopic length scales rapid quenching of the glass network may also change the atomic rearrangement such as the next neighbor distances. To this end, the shift of average bond distances was measured using wide-angle X-ray scattering (WAXS) at the beamline cSAXS at the Swiss Light Source (PSI Villigen, CH). Within this experiment, the sample is illuminated with an 11.2 keV X-ray beam and scattering is recorded by a pixel detector (Pilatus 300k) in the wide-angle region (scattering vector range from 0.5 to 4 $Å^{-1}$). In fused silica a single correlation peak (atomic pair correlation function) represents the next neighbor distances. While the scattering change in heated or compressed liquids and glasses depends in a nonlinear fashion on applied temperature or pressure [87, 88] atomic-scale strain can be deduced in a simplified fashion through the shift of the correlation peak (at 1.6 $Å^{-1}$). After laser irradiation, the peak position is shifted towards larger bonding distances, which is equivalent to an expansive tensile strain, which could be measured with an accuracy of $2.5 \cdot 10^{-5}$. Calibration of the weak change in scattering has been done at the beamline PDIFF at the radiation source ANKA (KIT Karlsruhe) on a reference sample of fused silica by changing the temperature and

thus provoking expansion. By using a linear coefficient of expansion of $5 \cdot 10^{-7}\,K^{-1}$ [90] the scattering changes in the laser-irradiated samples can be normalized to an absolute strain value within the probed volume.

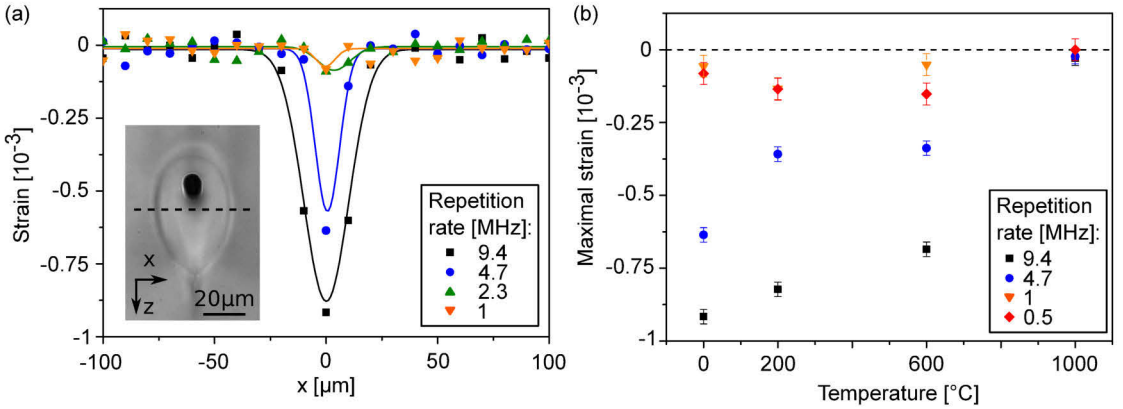

Fig. 3.15: Results of the WAXS measurements. (a) Strain of laser induced modifications for different laser repetition rates. The inset shows an optical micrograph of a modification inscribed with 9.4 MHz and a pulse energy of 150 nJ. (b) Maximal strain of modifications after isochronal annealing as function of the annealing temperature (the isochrones lasted 1 h).

Figure 3.15 (a) shows the measured total strain that appears to be quite localized and can only be obtained within the laser-modified region. In the surrounding region the change of bond distance, if there is any on an atomic scale, could not be resolved. The measured strain scales with the repetition rate and reaches values of $-9 \cdot 10^{-4}$ for 9.4 MHz. Since WAXS averages over the beam spot size (~6 µm) the real strain might be even higher. However, even in the regime of low repetition rates where nanostructures form (1 and 0.5 MHz, respectively) weak strain can be measured.

When the laser-modified glass is annealed the measured strain remains almost constant and only disappears after tempering at 1000 °C (see Fig. 3.15 (b)). This permanent change of bonding distance represents the frozen glass structure after rapid cooling which relaxes only when the temperature is close to the transition temperature of the glass (1100 °C [117]). At this point structural changes on mesoscopic scale (configuration of SiO_4 rings) vanish as well, which is confirmed by Raman measurements. The increased ion mobility leads to a relaxation on short (atomic) and intermediate length scales, the latter allows for the formation of five- or six-fold SiO_4 rings as they are mainly obtained in untreated silica.

The laser-induced strain can be separated into permanent strain (due to the change in density) and elastic strain (material response) [127]. By cleaving the sample, the elastic part near the surface can relax leading to the deformation of the surface (surface displacement). In case of fused silica, the tensile stress inside the center (produced by the permanent contraction after irradiation) relaxes in part resulting in a depression of the surface of both cleaved parts. By using a commercially available laser scanning microscope (Zeiss LSM 700), the height profile was measured for different repetition rates (see Fig. 3.16). For

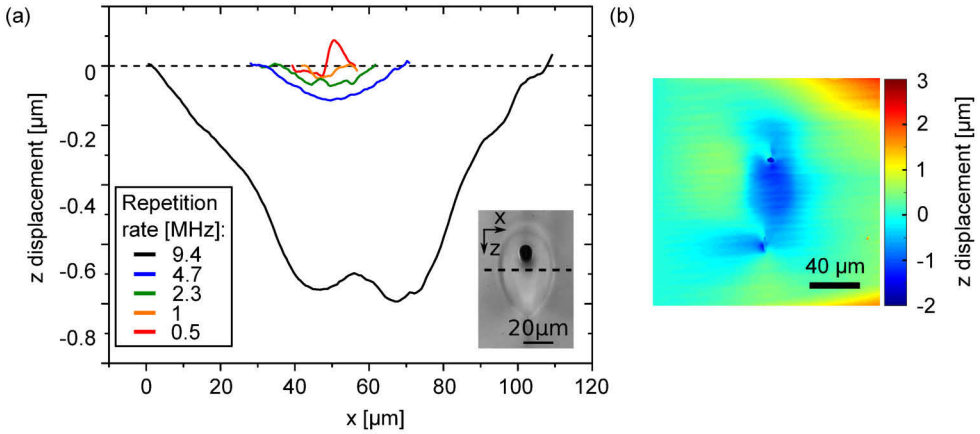

Fig. 3.16: Surface topography measured by laser scanning microscopy (LSM) after cleaving for modifications in fused silica inscribed with different repetition rates. (b) False-color map of a single modifications inscribed with 9.4 MHz, 200 nJ, numerical aperture of 0.4 and speed of the sample movement of 167 µm/s.

image recording a 400 nm cw laser was focused by an objective with a magnification of 50 (NA=0.95) and scanned over the sample surface. By acquiring a stack of images the 3D surface topography is reconstructed.

The depth of the valley is quite small and reaches values of -0.8 µm at 9.4 MHz. The appearance of an indented surface topography at high repetition rates confirms the anomalous expansion behavior of silica. At lower repetition rates, the depth first decreases significantly, and at 1 or 0.5 MHz, where nanostructures form, the valley turns into a bimodal excursion from the flat cleavage. This is due to the appearance of shear forces which result in a complex stress distribution within the laser modified region [119].

3.4 Chapter conclusion

In conclusion, ultrashort laser pulses allow for inscribing nanogratings with tremendous birefringence of up to several hundred nanometer in fused silica. The appearance of nanostructures requires a certain pulse overlap of several ten laser pulses per spot to develop regularly ordered grating bars. These always align perpendicular to the laser polarization. In agreement with the nanoplasmonic theory the period of nanogratings scales linear with the laser wavelength of the inscription laser. However, SEM images highlight that with increasing number of shots the distance of grating bars continuously decreases even below the period $\lambda/2n$ dissenting the nanoplasmonic theory.

By tuning the temporal pulse sequence, e.g. when using femtosecond bursts, pronounced defect-mediated absorption may favor the formation of nanogratings illustrated by increased optical retardance. For large average laser powers, however, heat accumulation leads to glass melting and the erasure of nanogratings.

Moreover basic laser pulse parameters such as the pulse energy, duration as well as the focusing objective define the laser intensity within the focal volume which strongly influences the formation threshold of nanogratings. This is illustrated by the laser-induced modification typically following regions of constant intensity. Consequently, the induced birefringence first increases with pulse energy and finally decreases due to strong material damage at high pulse energies. For pulse durations beyond 1 ps the parameter window where nanostructure formation is obtained shrinks due to thermal effects triggering strong material damage.

The formation of nanostructures is accompanied by the generation of STEs which rapidly decay into dangling bond type defects such as $E^{'}$-centers and NBOHCs. The bond breaking process comes along with the generation of molecular oxygen that exist dissolved within the network and captured in small voids. As micro-Raman measurements show, this oxygen mostly appears in the head of the modification where nanostructures form.

Moreover, the Raman measurements reveal that the laser-induced nanostructures are embedded in glass with higher number of 3-fold and 4-fold SiO_4 rings. This is a result of the rapid quenching leading to higher fictive temperature and increased material density. The lower relative volume corresponds to permanent strain which causes (as direct response) elastic strain within the laser-modified region as well as in the surrounding. By cleaving the laser-modified samples the elastic strain relaxes in part. In case of silica an indented surface topography indicates the anomalous glass density behavior on the fictive tem-

perature. However, the appearance of nanostructures comes along with a complex stress distribution most likely due to the assembling of small voids.
Intriguingly, laser-induced nanogratings exhibit extraordinary temperature stability and only vanish when the temperature reaches the strain point of the glass. Multiple annealing steps reveal that the induced birefringence is stable up to 850 °C. This emphasizes the potential of nanograting-based wave plates making them interesting for usage under harsh conditions.

4 Mechanism of nanostructure formation

Since the first discovery of nanogratings in the bulk of transparent materials the underlying formation process is under intense debate and up to now not fully understood. Thus, in this work several approaches were made to uncover the sequence of grating formation, alignment and their characteristics. First, this chapter covers the in-situ observation of nanogratings using a pump-probe approach. Subsequently, the stepwise nanopore formation, alignment and arrangement in periodic grating planes is studied by combining small-angle X-ray scattering (SAXS), focused ion beam milling (FIB) and SEM imaging. In the following, this approach is used to analyze intriguing phenomena such as the rewriting of an existing nanograting and the transition of bulk nanogratings to laser-induced periodic surface structures (LIPSS). Thereafter the formation of nanogratings in different glasses is comprehensively investigated. Finally, the results are summed up to develop a new model of the nanograting formation.

4.1 In-situ observation of nanograting formation

Diffraction of light provides a noninvasive and simple approach to record the formation and evolution of nanogratings. In this case, short wavelengths are required due to the fine periods. To this end, an ultrashort laser source (Smart Light 50, Raydiance) emitting pulses at a wavelength of λ=1550 nm (pulse duration 800 fs) served to inscribe nanogratings. The long wavelength and correspondingly large grating period ($\Lambda=\lambda/2n=$ 538 nm) facilitate the inspection by diffraction. Figure 4.1 (a) shows the stationary diffraction spot of nanogratings illuminated by probe light with 473 nm wavelength. Since the nanograting period is close to the probe wavelength only the first order diffraction signal can be obtained. However, both images depict the wide first order diffraction signal which is

much more pronounced if nanogratings are inscribed with 10^4 pulses per spot instead of 50. Most likely this is due to well-defined grating bars (see Section 3.2.1). When mapping the spot position in dependence of the number of laser pulses used a small shift directly reveals the change in the underlying grating period.

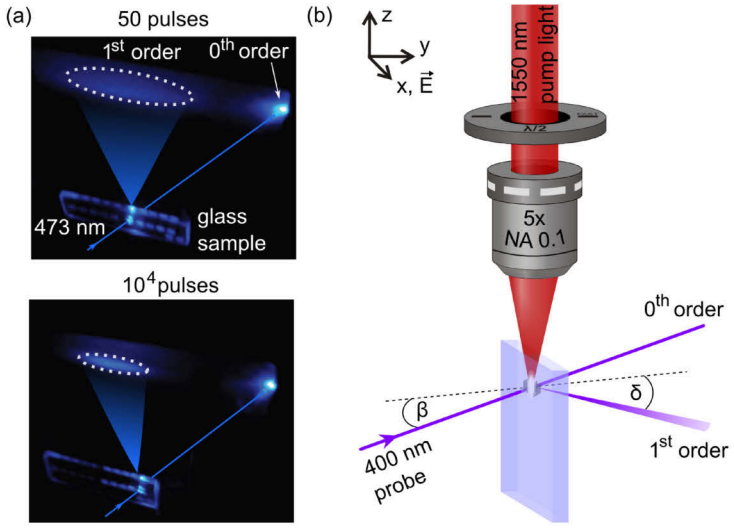

Fig. 4.1: (a) Image of a stationary diffraction measurement of nanogratings inscribed with 50 pulses per spot (upper) and 10^4 pulses per spot (lower). The dashed ellipse marks the corresponding first order diffraction spot. Please note that the transmitted and diffracted beam is illustrated. (b) Sketch of the in-situ measurement. During the nanograting inscription the first order diffraction signal (within the x-y-plane) is mapped using a triggered iCCD camera. The dashed line indicates the normal of the glass surface.

In order to reveal the sequential grating formation an in-situ setup was built up to measure the first order diffraction during inscription. To this end, a cw laser with a laser wavelength of λ_p=400 nm was used to probe individual laser spots as shown in Figure 4.1 (b). A triggered ICCD camera (4-Picos-Digital, Stanford Computer Optics) served to record the first order signal. Due to the weak diffraction signal an integration time of 5 µs was used while the measurement was repeated up to 5 times and the resulting images were averaged. Strong fluorescence due to laser-induced defects was cut away by a narrow-band filter.

Calibration of the diffraction angle was done using gratings with defined period fabricated by electron-beam lithography. To maximize the covered angle distribution imaged on the camera an incidence angle β=40° of the probe beam was chosen resulting in an exit angle δ=0° for a grating period of 600 nm. Refraction at the entrance at exit sur-

face was taken into account but cancels out when calculating the period of the grating $\Lambda^* = \lambda_p/(sin(\beta) - sin(\delta))$ (assuming first order diffraction). Based on the small distance of the sample and detector of a few centimeters periods from 490 nm up to 820 nm could be resolved. For larger input angles the diffraction efficiency clearly drops most likely due to both, pronounced Fresnel losses and the fact that the optical thickness of the grating increases. To maximize the spot size and hence the number of coherently arranged grating bars the inscription by the pump beam was done using a pulse energy of 8.4 µJ, a repetition rate of 50 kHz and an microscope objective with a numerical aperture of 0.1. Figure 4.2 shows the measured period in dependence of the applied laser pulses while the period measured by SEM after polishing and etching is shown for comparison.

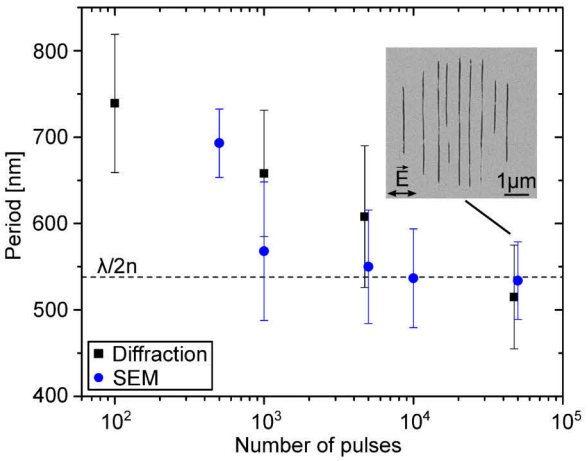

Fig. 4.2: Period of nanogratings measured in-situ by optical diffraction (at 400 nm) and with SEM (after polishing and etching the irradiated samples). The inset shows an SEM image of an irradiated laser spot with $5{\cdot}10^4$ laser pulses (otherwise same laser parameters).

The measured period continuously decreases from about 750 nm at 100 pulses to 500 nm at $5{\cdot}10^4$ pulses and agrees with the period measured by SEM. Although in principle the reduction of the periodicity agrees with the previously obtained trend (see e.g. Fig. 3.3) the actual slope is more shallow. This is due to the point-wise inscription resulting in a less efficient seeding of the nanograting (see Section 4.2.5, [128]). However, the in-situ measurement reveals a clear signature of periodic grating bars already a few µs after the laser pulse was incident indicating that the imprinting of the grating structure occurs on shorter time scales. However, the reducing error bars of the measured period denote the better quality of the grating with ongoing irradiation. This is most likely due to both a

higher filling fraction of grating bars (see Section 4.2.5) and based on the reduced period an increase in the number of grating bars resulting in a stronger diffraction signal.

As shown by Mauclair et al. the diffraction signal of nanogratings can be further improved by using double pulses with short temporal separation below one ps [105]. However, in this study the diffraction signal was analyzed by inscribing multiple nanograting traces with large overlap to increase the diffraction efficiency. In contrast, for time-resolved studies of a single spot X-rays may be better suited since they reveal kinetic information in the millisecond range as well as structural features statistically averaged over the whole probe volume [129].

4.2 Stepwise pore formation and alignment

Despite the period of nanogratings can be mapped by diffraction of light within the visual wavelength range the underlying substructure remains elusive. Actually, this issue remained unanswered for a long period due to invasive sample preparation techniques such as polishing and etching erasing fine structural details [53]. First studies in 2008 discovered that nanogratings are composed of self-aligned nanocracks [15]. Subsequently Lancry et al. reported that nanogratings evolve from nanoplanes into nanocracks with typical diameters of 20 nm [29] while Raman measurements suggest that these cracks are filled with oxygen [130]. However, these studies rely on mechanical cleaving and subsequent imaging by SEM. While cleaving irrevocably destroys the sample, material within the voids maybe lost. Moreover, these time-consuming sample preparation and imaging techniques provide two-dimensional cross sections at arbitrary horizons and can hardly address the evolution of cracks depending on various laser parameters.

To address these issues small angle X-ray scattering (SAXS) in combination with FIB milling and subsequent SEM imaging was used in this work. One of the key advantages of SAXS is to measure the scattering response of particle ensembles without any sample preparation techniques. Due to the short measurement time needed SAXS is used to map structural features such as the three-dimensional size, shape and number of nanoscopic voids in dependence of crucial laser and process parameters while the nanostructures are still buried within the bulk.

4.2.1 Experimental approach

For the SAXS measurements non-overlapping traces with a total size of 120 x 200 μm^2 where inscribed in the bulk of fused silica. The inscribing wavelength was 515 nm, the pulse energy 150 nJ, the pulse duration 450 fs and the numerical aperture of the focusing objective 0.55. The repetition rate was decreased to 10 kHz avoiding heat accumulation effects. To keep absorption losses of the X-ray beam low the samples where laterally polished down to a thickness of 300 µm. Care has been taken not to harm the buried nanograting structures.

The SAXS measurements were performed at the beamline cSAXS of the Swiss Light Source (PSI Villigen, Ch). Within this setup the nanograting samples were illuminated with an 11.2 keV X-ray beam (corresponding photon wavelength of 0.11 nm) exhibiting asymmetric beam shape with dimensions of 30 x 5 μm^2. The scattered rays were recorded by a large direct-converting pixel detector (Pilatus 2M) after the main beam was blocked (see Fig. 4.3 (a)). The propagation direction of the X-ray beam was either parallel to the direction of the inscribing laser (z) to obtain (transversal) scattering features (along x and y direction) or perpendicular to also reveal longitudinal information (along z) of the induced nanostructures. Moreover, rotation of the sample was done to uncover the transversal shape of the induced nanostructures [61]. Due to the large sample-detector distance of 7.2 m and the high beam brilliance maximum feature sizes of up to 400 nm could be resolved. Exposure times of 0.1 s until a few seconds were sufficient in order to obtain significant scattering signal.

For data analysis the background from the pristine background material was subtracted before the scattering signal was integrated along the main axis (e.g. x and y) to obtain the scattered intensity I(q). Figure 4.3 (b) shows an exemplary Kratky plot $I(q)\cdot q^2$ of the scattering intensity I(q) which qualitatively allows to distinguish multiple size hierarchies [131]. Along the x-direction (parallel to the polarization of the inscribing laser) a broad peak indicates nanoscopic sheets while their periodical alignment is indicated by distinct diffraction peaks (first and second order is visible) in the low-q range. The position of the diffraction peaks (e.g. first order peak at q_0) directly yield the average distance of small sheets $p = 2\pi/q_0$. Quantitative information of particular feature sizes is gained by the unified fit (see Section 3.1.3). Along the x-direction a single size population is sufficient to represent the scattered intensity in the high-q range. In vertical direction (y) as well as along the longitudinal direction (z) two size hierarchies have to be assumed. Data analysis

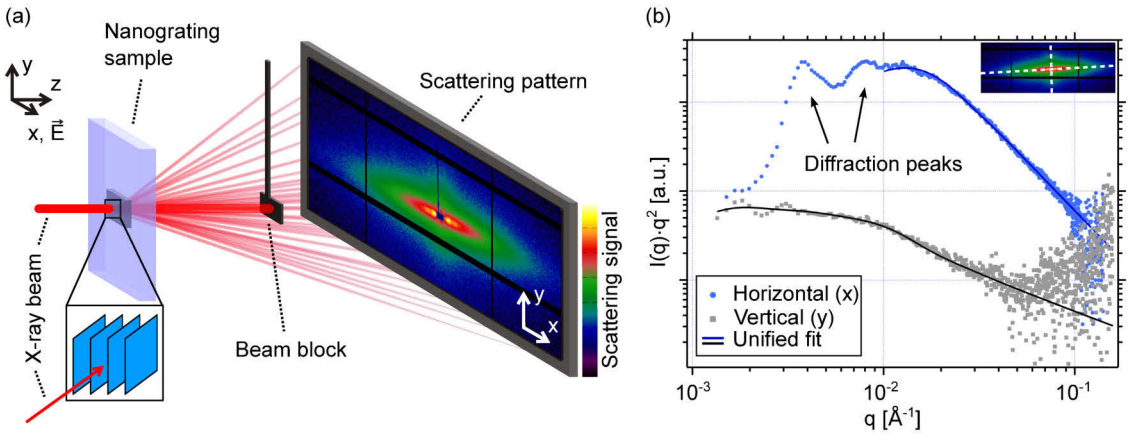

Fig. 4.3: (a) Sketch of the SAXS setup. The black lines are the insensitive areas of the detector. (b) Exemplary Kratky plot $I(q)\cdot q^2$ of the scattered intensity I(q) along the main axis x (streak direction) and y (perpendicular to streak) indicated by the inset. The solid line represents the corresponding unified fit to reveal the underlying feature sizes of nanopores.

of the scattering data was performed using Irena: tool suite for modeling and analysis of small-angle scattering [132].

To compare feature sizes gained by SAXS focused ion beam (FIB) milling in combination with SEM imaging was used. FIB allows to dissect the underlying structure of nanogratings with nanometer precision preventing any large-scale distortions and preserving the integrity of nanogratings. First individual traces of nanogratings were inscribed in shallow material depths and the material was dissected using a commercial FIB device (Zeiss Neon 60) until nanogratings were visible in SEM. Subsequently, a volume containing nanogratings was milled and imaged by SEM simultaneously using a distance of slices of about 30 nm. Afterwards standard image corrections were applied to remove brightness gradients or artifacts in the SEM images. The recorded SEM images served to reconstruct the three-dimensional structure of nanogratings using an implemented MATLAB code.

4.2.2 Morphology of induced nanopores

To uncover the primary constituents of nanogratings as well as their three-dimensional structure FIB milling and simultaneous SEM imaging was used. Figure 4.4 shows the reconstructed nanostructures inscribed with 1, 2, and 500 laser pulses per laser spot (otherwise the same laser parameters as given above in Section 4.2.1) for polarization direction perpendicular to the scan direction.

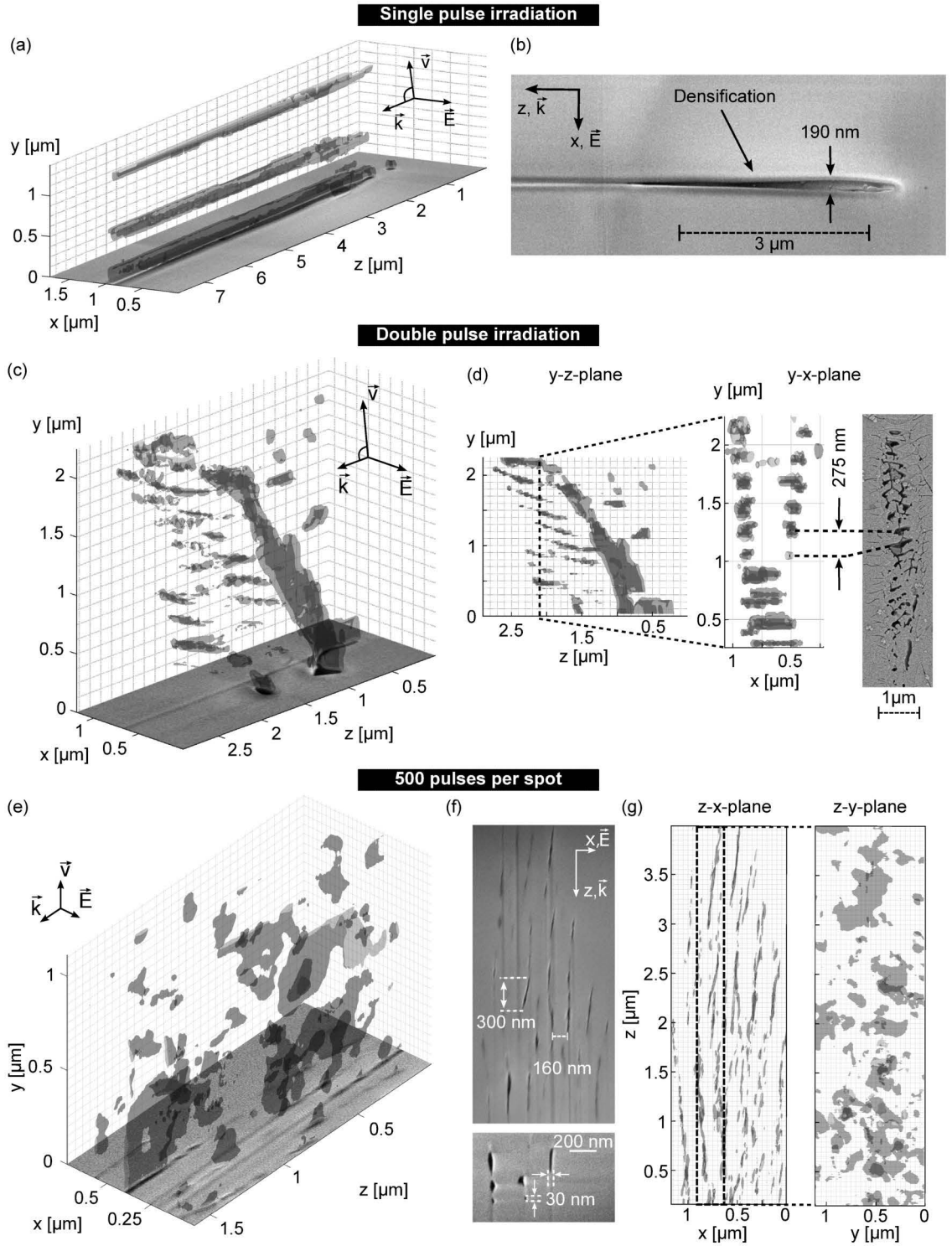

Fig. 4.4: Three-dimensional reconstruction of induced nanostructures inscribed with (a)/(b) 1, (c)/(d) 2 and (e)-(g) 500 laser pulses based on several SEM images after FIB milling. The distance of adjacent slices was 30 nm for 1 and 2 pulses per spot and 12.5 nm for 500 pulses. Exemplary SEM images are shown in (b), (f) as well as in the z-x-plane of (a), (c) and (e).

The exemplary SEM images in Figure 4.4 (b), (c), (e) and (f) confirm that the laser-induced nanostructures consist of hollow voids (dark regions). Single pulse radiation results in voids with transversal diameters of about 190 nm as shown in Figure 4.4 (b). The longitudinal size of several μm, however, is significantly longer which is an artifact of the milling process due to increased milling rate underneath the void. The real length is smaller as it will be shown by SAXS and SEM in the following sections. Moreover, the convex shaped dome in the surrounding of the void (see Fig. 4.4 (b)) points towards a material densification due to the reduced ablation cross section during the milling process. This high-density modification of silica is a result of a laser-driven micro-explosion leading to material compression in the surrounding of the void [9].
The reconstruction in Figure 4.4 (c) illustrates the void structure when inscribing with two laser pulses per spot. First a chain of periodic voids elongated perpendicular to the scanning direction appears. Their period of 275 nm corresponds to the spatial pulse distance (see Fig. 3.6 (d)). Due to the small pulse separation (half spot size) a newly irradiated laser spot squeezes the previous pore adjacent to it to an elliptical shape. In addition, a large crack along the scanning direction appears which points to the accumulation of stress along the scanned path.
After 500 laser pulses a fully established nanograting shows up in Figure 4.4 (e). The reconstructed sub-volume depicts the regular arrangement of individual nanopores which link together to form a common grating plane. This coherent alignment is clearly visible in the z-x-cut of the full reconstructed nanograting volume shown in Figure 4.4 (g). Typical feature sizes are indicate in the exemplary FIB-SEM image of Figure 4.4 (f) allowing to compare with the results gained by SAXS.

4.2.3 Evolutionary dynamic of nanopore formation

The formation and assembling of periodical grating bars due to the cumulative action of several laser pulses is a step-wise process. To map the growth of primary constituents as well as their collective alignment the onset of structure formation is studied. Here the laser focus is scanned through the bulk as is standard practice for direct writing while the spatial pulse overlap is tuned by setting the scan velocity correspondingly. For comparison different laser polarization orientations (0°, 45°, 90° and 135°) relative to the scan direction were studied to disentangle polarization-driven mechanisms from effects due to the uniaxial scanning direction.

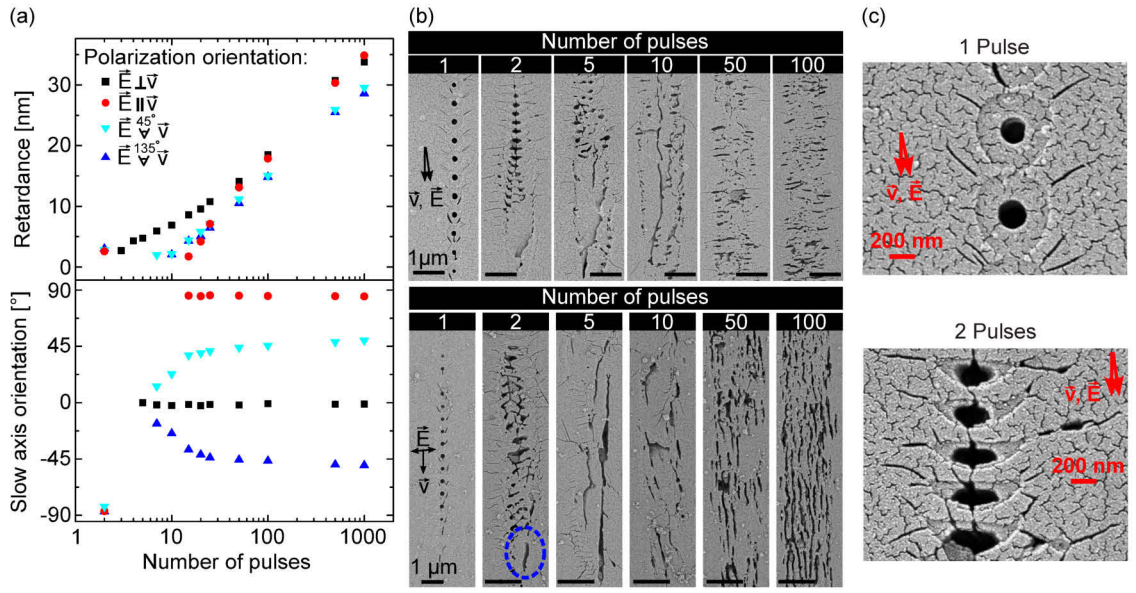

Fig. 4.5: (a) Optical retardance, slow axis orientation and (b) SEM images after polishing and etching in dependence of the number of pulses for different writing regimes. The scale bars in (b) correspond to 1 µm. (c) Zoom of SEM micrographs. The randomly aligned fine scratches are due to the gold coating to prevent charge accumulation.

First the amplitude and orientation of the induced birefringence in dependence of the number of applied pulses was analyzed (see Fig. 4.5 (a)). For all writing regimes the retardance increases monotonically with logarithmic fashion with the number of pulses as found in Figure 3.3 (a). After 1000 pulses both 0 and 90° show the highest birefringence. Up to 50 pulses per spot, however, a faster growth of birefringence is measured for perpendicular writing, i.e. when the polarization is perpendicular to the scan direction. Intriguingly, for two pulses a small retardance is found for all scan regimes except for perpendicular writing. The slow axis orientation in Figure 4.5 (a) is perpendicular to the laser scan direction for the other three polarization orientations.

The SEM micrographs allow to connect the observed retardance behavior with basic structural features (see Fig. 4.5 (b)). After illumination with one pulse per spot only isolated, spherically shaped voids with typical diameters of about 200 nm form in agreement with the FIB-SEM reconstruction in Figure 4.4 (a)/(b). This size is well-defined with only 10 % variations over a broad ensemble as confirmed by SAXS. The zoom in Figure 4.5 (c) illustrates the halo-like surrounding of the voids indicating the densified material modification shown before (see FIB-SEM images in Figure 4.4 (a)/(b)). Little is known about this phase up to now. However, the modified structural composition becomes apparent due

to the change in etching behavior in contrast to the untreated material. Along the longitudinal direction (z-direction) the voids are elongated about 700 nm, visible by the lateral displacement that corresponds to a shift in longitudinal position (depth slope 12 %). This is in the range of the Rayleigh length of the laser beam (0.55 µm) and hence follows the laser intensity distribution as expected from laser-driven micro-explosion theory [9].

By increasing the spatial overlap the voids are still visible in the SEM images but starting to get deformed perpendicular to the scan direction as shown by the zoom in Figure 4.5 (c) and in the 3D reconstruction in Figure 4.4 (c)/(d). This is accompanied by shear forces and the appearance of cracks at the tip of the voids. A slight directionality is visible caused by the writing direction and thus the sequence of fresh to previous voids. Since the directionality can be obtained for both writing regimes in the same way a polarization-driven effect can be excluded. The asymmetric voids with sub-wavelength periodicity are the cause for the two-pulse retardance for almost all writing regimes.

For larger pulse overlap (5 pulses per spot) randomly aligned voids as well cracks along the scanned path remain. Only after ten laser pulses regularly ordered grating bars appear for perpendicular writing leading to significant retardance in contrast to all other writing regimes.

The SAXS measurements give a comprehensive picture for the faster growth when the polarization is perpendicular to the scanning direction. Figure 4.6 shows the SAXS patterns for parallel, 45° tilted and perpendicular writing relative to the scan direction. Single pulse illumination results in an almost symmetric scattering pattern with periodic modulation of the scattering signal on top. The envelope of the scattering signal is mainly defined by the form factor of the voids, which, regardless of the inscribing polarization, exhibit nearly spherical cross section. The periodic modulation stems from the deterministic void arrangement along the scanned path. For 2 (perpendicular writing) or 3 pulses per spot (parallel or tilted writing) the SAXS pattern deforms towards a cross-shape. The fringe spacing of the periodic modulation increases due to smaller spot separation and hence distance of structural features. Based on the reciprocity of the scattering process elongated streaks in the SAXS patterns are typically a signature of structures oriented perpendicular to the streak direction. Thus, the cross shape illustrates two populations of cracks (parallel and perpendicular to the scanning direction) which where found in the SEM images before. At two pulses the horizontal line of the cross is strongly pronounced for perpendicular polarization. Hence the early appearance of the cracks along the scanned

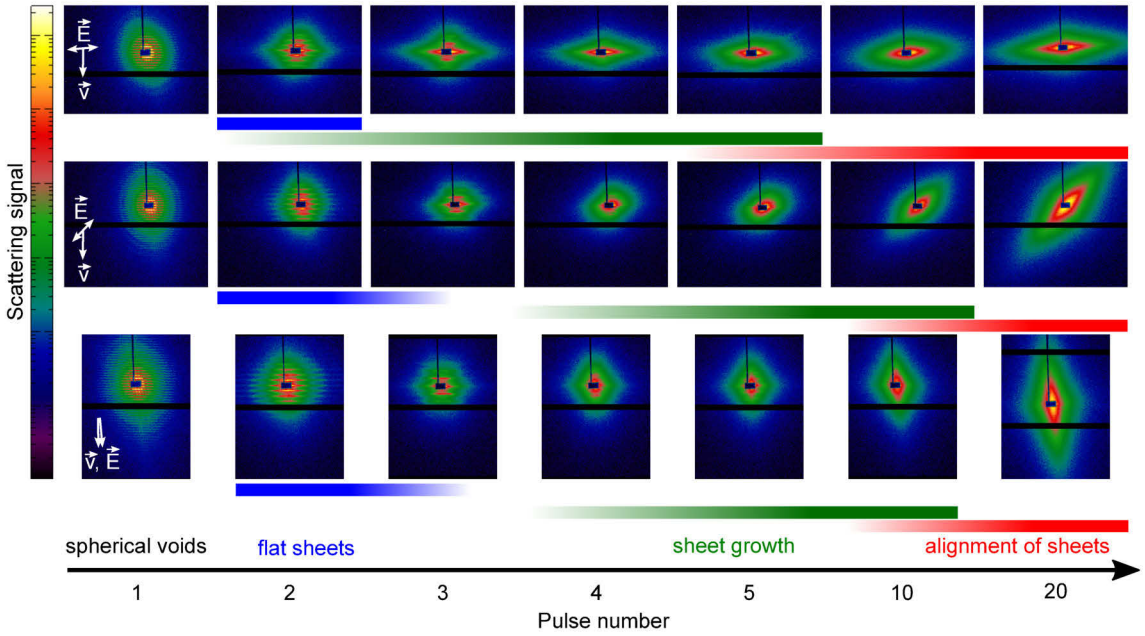

Fig. 4.6: SAXS patterns of nanogratings inscribed with different polarization orientation relative to the scanning direction. The black lines are the insensitive areas of the detector.

path (dashed ellipse in Fig. 4.5 (b)) most likely cause the canceling of both retardance contributions resulting in zero net retardance.

While the early stage of structure formation is deterministic such as the regular arrangement of voids, the subsequent formation of cracks due to the densely packed irradiation spots along the scanned path is slightly enhanced if the polarization direction is perpendicular. Here local field enhancement [73] coincides with the scanning direction which might support crack formation along this path.

The further evolution is accompanied by strong increase of scattering intensity perpendicular to the polarization direction (marked by the green bars). In comparison to the SEM images after 5 to 10 pulses, this indicates the growth of anisotropic sheets. However, the alignment of these early sheets is not well defined in the first place as the streak orientation (azimuthal angle) of the SAXS patterns in Figure 4.7 (a) depicts.

For the perpendicular orientation for instance, the early streak formation comes along with a shift from being strictly perpendicular to the scanning direction to being shifted diagonally. This tilt of 4° occurs in between 5 and 10 pulses. For tilted scanning (135°) the streak position continuously moves about 40° starting at 3 pulses per spot until it stagnates at about 100 pulses.

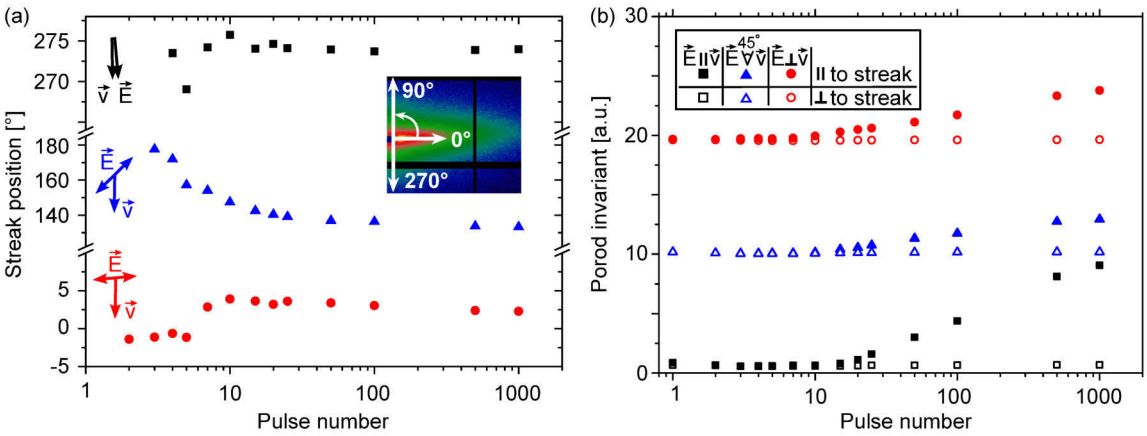

Fig. 4.7: (a) Streak orientation (azimuthal angle, indicated by the inset) for nanostructures inscribed with different polarization orientations relative to the scanning direction. (b) Porod invariant measured along and perpendicular to the streak direction. The different writing regimes are separated by a constant offset.

This trend indicates the transition between two individual mechanisms: The initial cracks oriented parallel and perpendicular to the scanning direction are due to the spatial sequence of densely packed irradiation spots. Only after a large number of laser pulses incident the polarization-controlled nanograting (sheet growth and alignment) develops. Since the laser polarization and scan direction do not exactly match the shift of streak position thus illustrates the transition from one regime into another, i.e. from strain to polarization driven. This explains the continuous rotation of the slow axis orientation in Figure 4.5 (a) for nanogratings inscribed with 45° and 135° tilted polarization orientation. Moreover, the initial cracks act as seed for the growth of anisotropic sheets as the Porod invariant (along the streak direction) in Figure 4.7 (b) indicates. The invariant represents the total pore volume (number of pores) and increases similar to the optical retardance in a logarithmic fashion with the number of pulses [133]. In case of perpendicular polarization the invariant starts to grow earlier while the final invariant for the 135° orientation lags behind. Even in this plot the transition from irregular cracks to aligned sheets is visible. While the cracks do not grow in number the final sheets do, driven by a feedback process which sets in after a few tens of laser pulses. This feedback might be mediated by the excitation of surface plasmon-polaritons leading to a coherent assembling of individual nanopores as described in [134]. However, within this model the cavity-like amplification mechanism is only present if the distance of adjacent plasma planes is between λ/n and $\lambda/2n$ while significantly smaller periods have been measured yet (see Section 3.2.1). As

proposed in [96] the scattered light at individual grating planes may favor an ongoing reduction of the average distance of grating planes.

SAXS allows for quantitatively evaluate the three-dimensional size and shape of pores and thus provide access to microscopical properties noninvasively. Figure 4.8 (a) shows the measured nanograting period (p) as well as the thickness of pores (along the polarization direction (x), see Fig. 4.3) for the case when the polarization direction is perpendicular to the scanning direction.

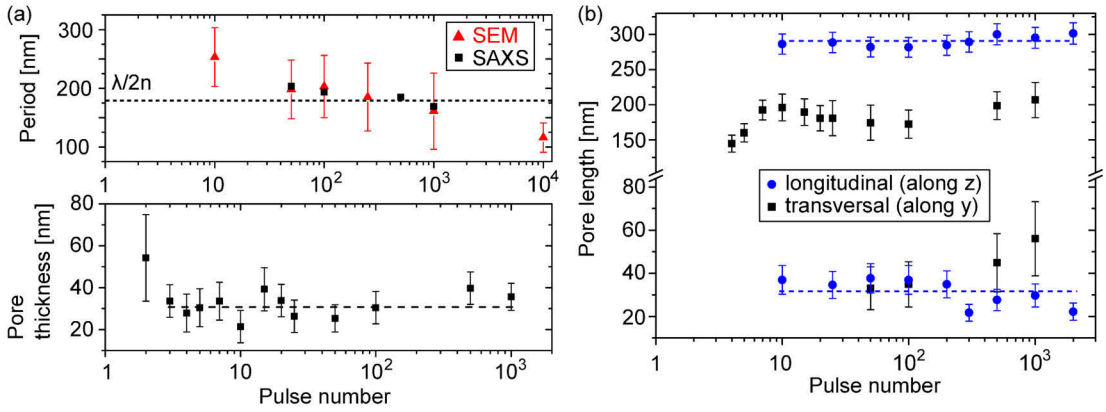

Fig. 4.8: Results of the SAXS measurements. (a) Nanograting period and pore thickness (along x, polarization direction). (b) Pore length in transverse (along y) and longitudinal direction (along z).

The thickness of pores of about 28 nm barely changes over the illumination and agrees well with the thickness found in the FIB-SEM images of Figure 4.4 (f) as well as with the values reported from other groups [29, 15, 135]. Only at two pulses larger thickness is measured reflecting the flat sheets found by FIB-SEM. However, the mean distance of pores (period) continuously decreases as obtained in SEM images of etched samples (see Fig. 4.5 (b) and 3.3 (b)) or measured by diffraction (see Fig. 4.2).

The length of pores along y (laser polarization direction) first increases to about 200 nm at 10 pulses before reaching a plateau. After 50 pulses per spot best fits to the SAXS data were obtained by introducing a second size distribution with similar dimension as the sheet thickness. However, this is not correlated to new features in SEM images but rather reflects the growing porosity of the glass by repeated heating and quenching. Similar values were found by TEM measurements of Sharma et al. [135] confirming the multi-size hierarchy of nanopores.

Along the laser propagation direction (z) constant feature sizes of 30 nm and 300 nm are measured which are confirmed by the FIB-SEM images in Figure 4.4 (f). In contrast to the constant average feature size, the size distribution broadens with irradiation as indicated by the growing polydispersity index (PDI, see Section 3.1.3) from 2 (10 pulses) to 8 (2000 pulses). This illustrates that with rising number of pulses incident, the total number of pores increases resulting in the assembling of small pores to larger structures and hence a broader distribution of available feature sizes.

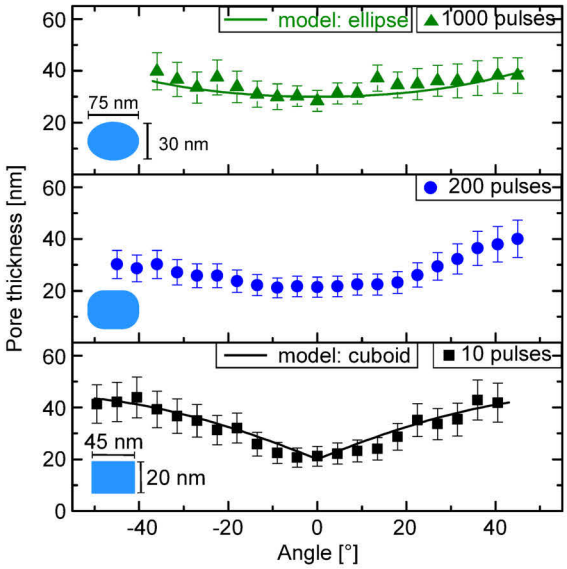

Fig. 4.9: Pore thickness measured by SAXS when rotating the nanograting sample around the z axis and analyzing along x. For comparison, the effective length (persistence length) was calculated under assumption of cuboidal or ellipsoidal shape of the nanopores (full lines; assumed shape and semi axes illustrated by the blue insets).

To uncover the shape of small pores the nanograting sample was rotated with respect to the z axis from -45° up to 45° in steps of 4.5° and the corresponding SAXS pattern was studied along the x direction (see Fig. 4.9). After 10 pulses a strong angle dependence is measured. The effective diameter increases from 20 nm (at 0°) to 43 nm (41°) which can be nicely reproduced assuming a cuboidal structure with semi axes of 20 nm and 45 nm. When increasing the pulse number the absolute variation of diameters decreases. Good agreement with the measured diameters is achieved by assuming an ellipsoidal shape with semi axes of 30 nm and 75 nm at 1000 pulses. This matches the increased pore length shown in Figure 4.8 (b).

4.2.4 Influence of relevant laser parameters

The sequential formation mechanism of nanogratings occurs in general in the same way when varying basic laser parameters. However, principle characteristics of the induced nanostructures such as period or thickness of the induced nanopores might significantly change. For the sake of clarity a simplified overview on the changes of optical retardance, Porod invariant, pore distance (period) and pore thickness is given by Table 4.1.
First, the measured Porod invariant always coincides with the optical retardance indicating a link between macroscopical birefringence and microscopical properties in terms of the number of induced nanostructures. This reflects that the small voids constitute the primary component of nanogratings.

Tab. 4.1: Nanograting properties measured by optical retardance, SEM and SAXS in dependence of the laser pulse number per spot (N_P), pulse energy (E_P), pulse duration (τ_P) and repetition rate (R).

Laser parameter	Retardance	Porod invariant	Period	Pore thickness
N_P (10 - 10^3)	↑	↑	↓	const.
E_P (50 - 200 nJ)	↑	↑	↓	const.
τ_P (0.4 - 2 ps)	↓	↓	const.	↑
R (0.01 - 1 MHz)	↓	↓	const.	↓

An intuitive picture for this link can be given when increasing the laser pulse energy from 50 to 200 nJ. This leads to a larger modification zone with more grating planes and consequently a larger amount of pores, which cause increased birefringence (see e.g. Fig. 3.8). Similar to the dependence on the pulse number the period decreases slightly [98, 61] while the thickness of pores remains constant.
When increasing the laser pulse duration from 0.4 until 2 ps the pore thickness increases from about 32 ± 8 nm to 66 ± 4 nm. Larger feature sizes at higher pulse duration can be obtained in the SEM images of Figure 3.9 (b) as well although care has to be taken evaluating absolute feature sizes due to the preceding etching process. The larger pore thickness might be a hint for the underlying process of pore growth. For larger pulse duration the intensity (and electron density) decreases while the material is heated more efficient when the pulse duration exceeds 1 ps [50]. This might impede the growth of highly anisotropic pores. In addition, the coherent assembling of grating planes is prohibited illustrated by larger irregularity of grating planes shown in Figure 3.9 (b). Another consequence of the

smaller pulse intensity is the shrinkage of the overall modification zone (see Fig. 3.9). Thus, although the period remains constant and the filling ratio (ratio between pore thickness and period) increases lower retardance is measured.
Moreover, the influence of thermal effects on the microscopical structure is depicted by increasing laser repetition rate from 0.01 to 1 MHz. Again, the optical retardance and the invariant decreases. However, increasing temperatures and subsequent higher viscosity of the glass within the focal region results in decreasing feature sizes from 36 ± 4 nm to 26 ± 3 nm [136].

4.2.5 4-phase model

Combining the results of the SAXS, FIB-SEM and retardance measurements a detailed picture of the primary constituents of nanogratings, their growth and periodic assembling can be developed. The stepwise evolution as function of the number of laser pulses can be described in 4 individual phases (see Fig. 4.10).

1. Single pulse irradiation, i.e. illuminating with spatially isolated laser pulses, results in isotropic cylindrical voids. Their dimensions are determined by the laser intensity distribution within the focal region. No preexisting defects (seeds) are needed while the formation of these voids is intrinsically deterministic.

2. When scanning the laser focus through the glass increasing pulse overlap (lower scan velocity) first leads to flattening of these voids perpendicular to the scanning direction triggered by the laser-induced micro-explosion (see [9]) of the subsequent laser pulse. The voids are surrounded by a shell of densified material while the closely arranged irradiation spots promote the accumulation of stress. Consequently, when increasing the pulse overlap further, cracks along the scanned path appear.

3. These cracks as well as randomly aligned voids nucleate the formation of anisotropic pores which grow to a size of about (200 x 30 x 300) nm^3. This growth is mediated by a feedback mechanism from pulse to pulse firstly driven by field enhancement perpendicular to the laser polarization [15] mediated by localized defect formation (bond breaking and oxygen migration) [95] reducing the ionization cross section for the subsequent laser pulse [24]. However, symmetry breaking between polarization parallel and perpendicular to the scanning direction is observed since the

cracks along the scanned path favor the pore growth along this path. Consequently the retardance increases faster for perpendicular writing. In contrast, an orientation of 45° is the least favorable case since no suitable seeds are available.

4. After a multitude of anisotropic pores have formed these align exactly perpendicular to the polarization direction and their number strongly increases. This could be driven by a cavity-like amplification process as suggested in [15] while the final period (Λ), however, can be below $\lambda/2n$ dissenting the nanoplasmonic model. In addition, due to the repeated heating and quenching a more porous glass matrix is formed. Due to the lack of seeds lowest retardance is obtained for 45 degree orientation.

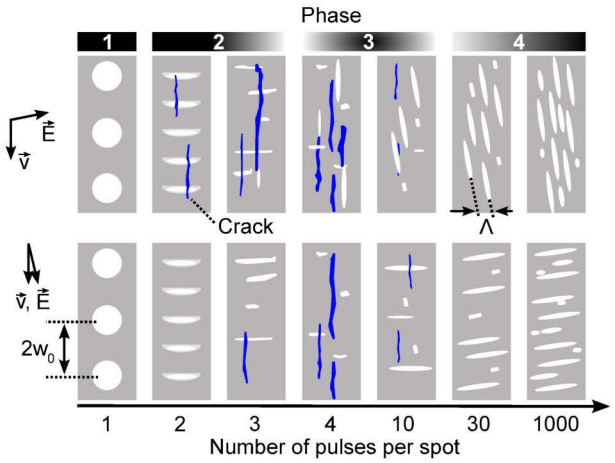

Fig. 4.10: Principle sketch of nanograting formation for two different writing regimes.

The presented formation sequence explains several aspects of nanogratings. First, one of the key findings is that nanogratings consist of hollow voids which link together to form coherently ordered grating planes. Thus, based on the large index contrast between the voids and the surrounding glass huge birefringence of several hundred nanometers can be induced despite the small size of the laser-induced modifications (typically a few µm) [28, 69, 137]. Due to the fact that the grating planes are composed of hollow pores the etch rate perpendicular to the polarization direction is much higher than in the parallel case [26]. When imaging nanogratings with lower resolution the index contrast blurs and apparently continuous index modulations are obtained [12]. Moreover, the finding of molecular oxygen in the top of laser-induced modifications (see Fig. 3.13; [95]) suggests

that this oxygen is captured within the small pores - the primary constituents of nanogratings.

The stepwise evolution of nanostructures directly links the formation of voids, typically obtained when using large pulse energies in single shot experiments, with the formation of nanogratings. Hence for glasses where void formation is hardly obtained, such as borosilicate [138], also nanograting formation is hindered [61]. This means that thermomechanical properties such as viscosity or Young's modulus influence the formation of nanogratings and not only single pulse voids [9]. A more detailed view of the dependence of nanostructure formation on the material composition will be given in Section 4.5. In addition, when scanning the laser focus through the bulk, directional crack formation mediates the formation of anisotropic pores. In contrast, when inscribing point-wise (see e.g. the in-situ measurements in Section 4.1) or with spatially uncorrelated spots (see Fig. 3.7) the formation is strongly delayed due to the absence of seeds.

Additionally, the results give prospects for functionalized photonic devices. As shown before, by tailored scanning of the focus through the glass, spherical voids are deformed perpendicular to the scanning direction. Due to the sub-wavelength periodicity and anisotropic shape birefringence is induced which could be optimized by adapted process parameters.

4.3 Rewriting of laser-induced nanostructures

The local inscription of strong birefringence within an otherwise isotropic host material offers broad potential for manifold applications. Even more, in 2007 it has been demonstrated that an existing nanograting can be erased and newly arranged by inscribing again at the same position with differently oriented laser polarization [20]. This is in particular interesting for data storage purposes [67] since imprinted information (data voxels) can be easily corrected or updated as needed. To uncover the formation of rewritten nanograting structures SAXS, SEM and optical retardance was utilized.

Within this experiments laser pulses with a pulse duration of 450 fs (laser wavelength of 515 nm), a pulse energy of 150 nJ at a pulse repetition rate of 500 kHz served to induce consecutive nanograting traces in fused silica. The pulses were focused in shallow material depths using an aspheric lens (New Focus 5722) with a numerical aperture of 0.55. The distance of adjacent traces was 0.5 µm covering an area of (100 x 100) μm^2. To an-

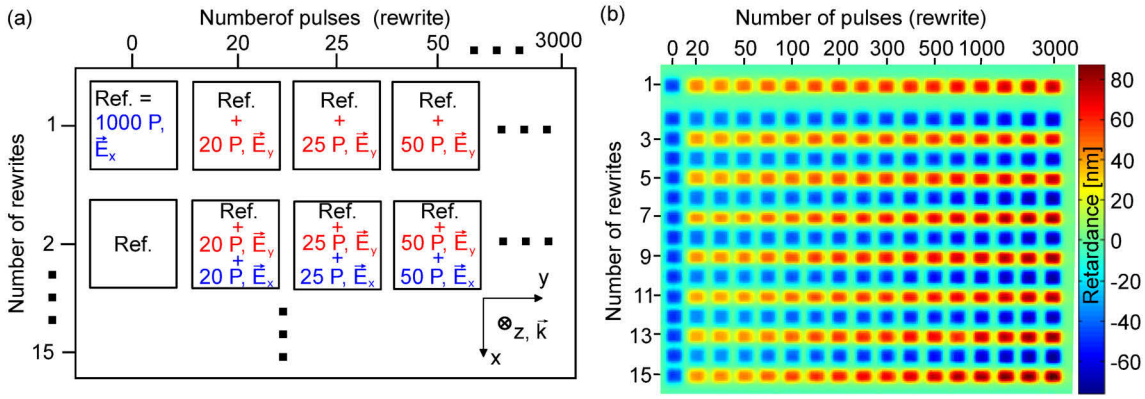

Fig. 4.11: (a) Sketch of the nanogratings sample showing a reference field (Ref.) that is rewritten up to 15 times, every time with 90° rotated polarization while the pulse number increases from 20 up to 3000. (b) False-color plot of the retardance of inscribed nanograting fields. The sign of the retardance marks the two distinct slow axis orientations.

alyze the evolution of the rewriting process a reference field (inscribed with 1000 pulses per spot, polarization along x) was rewritten up to 15 times (each time with 90° rotated polarization). At the same time the pulse number was varied from 20 up to 3000 (see Fig. 4.11 (a)).

The birefringence of the corresponding fields is shown in Figure 4.11 (b) while the different slow axis orientations ($E_{x/y}$) are encoded by the sign of the retardance (-/+). Hence the micrograph actually indicates the fast and repeated switching of the birefringence orientation after multiple rewrite steps. After single rewriting with 20 pulses per spot, a change in retardance from -50 nm to 40 nm is measured. Higher pulse numbers lead to a continuous increase of retardance. Intriguingly, further studies revealed that the directional information of birefringence can be deleted by 5 pulses per spot only. This fast switching process has been obtained for single spot illumination by Taylor et al. [20].

A microscopic view is gained by SEM images after polishing and etching of rewritten nanograting structures. Already after 5 pulses large cracks with irregular alignment along the scanned path appear (see Fig. 4.12 (a)). Simultaneously the old grating is partially blurred which, together with the anisotropic cracks, results in zero net retardance. The observation of cracks indicates the strain-driven regime at the early stage of nanograting evolution and coincides with the formation mechanism reported before. Subsequently, regular grating planes according to the new polarization direction grow with ongoing illu-

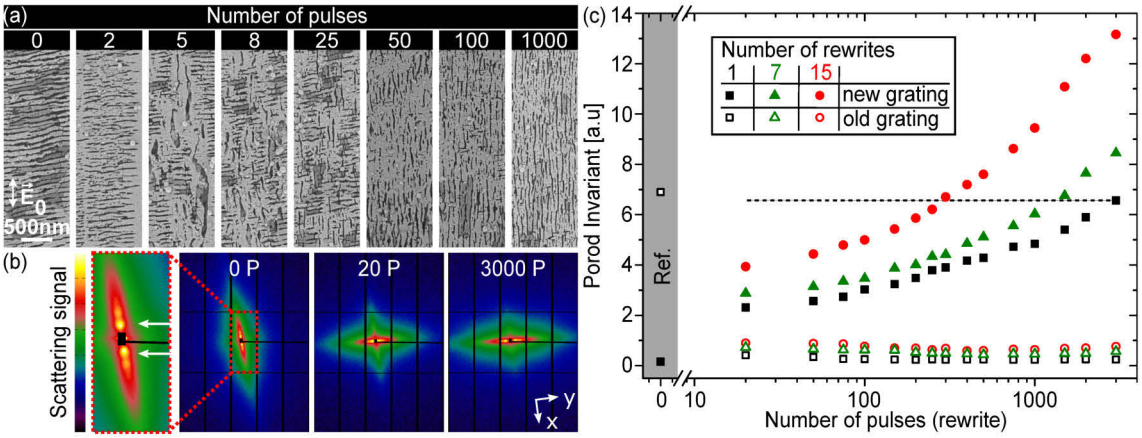

Fig. 4.12: (a) SEM images after polishing and etching and (b) SAXS patterns of nanogratings rewritten with different number of pulses. The inset in (b) shows a zoom of the central scattering plot of the initial nanograting indicating distinct diffraction peaks. (c) Porod invariant for single and multiple (7,15) rewritten nanogratings. Both the erasure of the old grating (open symbols) and the formation of the new grating (full symbols) is shown. The gray shaded area marks the values of the initial nanograting.

mination. Although the new grating replaces the old over its entire volume the rewriting process is not ideal since features of the old grating remain even after 1000 laser pulses.

A detailed picture of the rewriting process is given by SAXS. Figure 4.12 (b) shows the false-color plots of the scattering distribution in the detector plane. The anisotropic streak marks the short axis of elongated pores (laser polarization direction). A number of diffraction peaks are superimposed for the initial grating or the rewritten grating with large number of pulses. After 20 pulses these peaks vanish and the streak of the initial grating shrinks indicating the erasure of both the shape and alignment of pores. This is confirmed by the decreased Porod invariant of the old grating shown in Figure 4.12 (c). The invariant along the direction of the new grating increases with irradiation together with the strong change in birefringence. Still, some scattering features of the old grating remain and can be observed even after 3000 pulses.

This process holds true after multiple rewrites while interestingly the invariant as well as the retardance even becomes stronger after the 7th (or 15th) rewrite step. A direct comparison between even (E_x) and odd rewrite (E_y) is nevertheless hindered due to a difference in absolute retardance (see Fig. 4.13 (a)). This larger birefringence for odd rewrites might emerge due to the initial cracks along the scanning direction supporting the formation of the grating planes if the polarization is along y analogue to the single

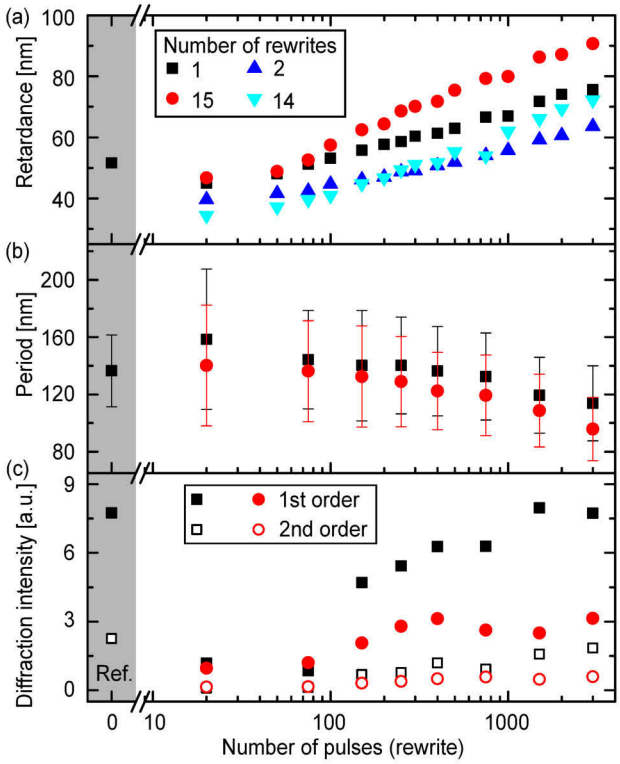

Fig. 4.13: (a) Optical retardance, (b) grating period and (c) intensity of the first- and second-order diffraction peak of nanogratings after various rewriting steps. The error bars in (b) account for the diffraction peak width (1/e of the maximum intensity). The gray shaded area marks the region of the reference field.

inscription reported previously (see Section 4.2). Looking more closely, two regimes in the evolution of the invariant and the retardance with a transition at about 100 pulses can be seen.

When rewriting several times (14/15) the retardance in the beginning ($\leq$ 100 pulses) is still small but strongly increases afterwards to reach significant larger birefringence as for single rewriting. During the first shots of the rewriting the old grating prevails and newly shaped pores are still irregularly arranged. Based on these early pores the new grating forms with further illumination. The relative enhancement for multiple rewrite steps, however, is caused by repeated annealing and quenching resulting in a more porous glass with new inhomogeneities.

The repeated rewriting also affects the underlying distance of pores (period) and the diffraction intensity gained by SAXS (see Fig. 4.13 (b) and (c)). While the diffraction peak width remains almost unchanged the final period decreases as function of the num-

ber of rewrites most likely as a result of an increasing number of inhomogeneities that trigger a pronounced seeding of pores [77]. In contrast, the diffraction intensity does not overlap as the retardance does. Due to a more perturbed glass with more disordered pores the regularity of the final nanograting is disturbed. On the contrary optical retardance is more related to the absolute number and elongation of pores, which is pronounced by repeated rewriting.

In summary, rewriting illustrates the strong action of the polarization driven feedback mechanism that even allows for the formation of a regular nanograting emerging from a strongly disturbed glass morphology. In this regard, the underlying grating formation including the growth of anisotropic pores, their alignment and period reduction occurs in the same way for numerous rewrite steps. The final birefringence of the rewritten grating (after 1000 pulses), however, increases with multiple rewrites. Thus, for applications such as nanograting-based encoding (e.g. for data storage applications) an intermediate regime of pulses incident is beneficial to avoid a drift in birefringence during multiple rewrites. The degradation of grating quality, in contrast, might lead to ambiguity of data bits after numerous rewrites.

4.4 Relation to periodic surface ripples

In contrast to bulk nanogratings, laser-induced periodic surface structures (LIPSS) are well known since the 1960s [13] and can be induced using cw or pulsed laser irradiation [74]. Typically two different periodicities with periods in the range of the inscription wavelength (coarse ripples or low spatial frequency (LSF) LIPSS) or below (fine ripples or high spatial frequency (HSF) LIPSS) are distinguished. While fine ripples are most prominent at the surface of transparent materials their alignment can be parallel [139, 140] or perpendicular [141, 142] to the polarization of the inscription laser.

To compare the formation of ripples and nanogratings SEM images of laser inscribed traces at the surface of silica were acquired. For inscription laser pulses with a pulse duration of 450 fs (wavelength of 515 nm), a pulse energy of 100 nJ at a repetition rate of 100 kHz were focused with an NA of 0.55 (magnification 40x) on the surface. Subsequently the samples were etched using the same etching parameter as for the bulk gratings: 90 s in 1 % hydrofluoric acid at room temperature.

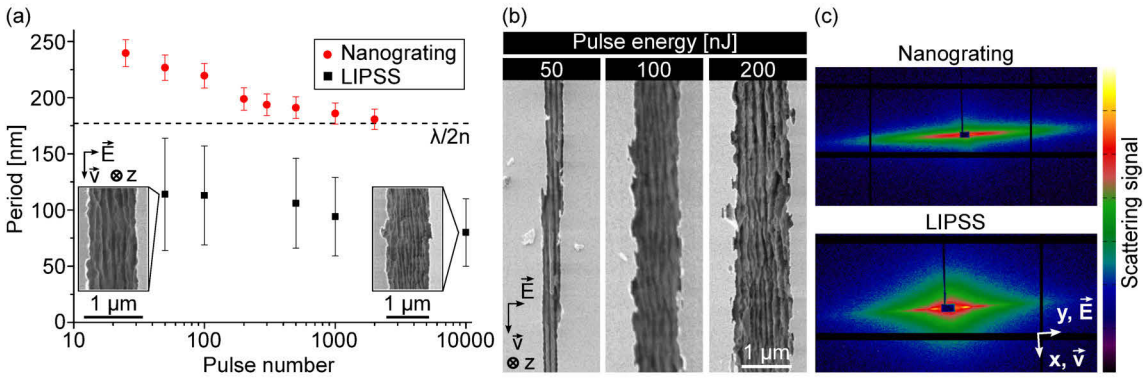

Fig. 4.14: (a) Period of LIPSS and nanogratings gained by SEM in dependence of the number of pulses per spot. The inset shows two SEM images of ripple structures after etching inscribed with 50 and 10000 pulses per spot. (b) SEM images of etched ripple structures at different pulse energies (at 10^3 pulses) and (c) SAXS patterns of nanogratings and ripples (pulse energy of 50 nJ).

Figure 4.14 (a) shows the measured period of the ripple structure obtained (exemplary SEM images shown in the inset). Compared to the bulk nanogratings the measured period is much smaller and clearly below $\lambda/2n$. Hence these ripples correspond to the most commonly reported fine ripples (HSF-LIPSS) [143, 144]. However, distinct similarities to bulk nanogratings such as the decrease in periodicity with increasing number of pulses (although considering with care due to the error of measurement) are obtained. Moreover when keeping the number of pulses per spot fixed (at 10^3) and increasing the laser pulse energy the size of the modified trace increases without significant change of periodicity (see Fig. 4.14 (b)). The growing extend of surface feature is similar to laser ablation while incubation from pulse to pulse leads to a decrease of the ablation threshold with increasing pulse overlap [145].

Having a closer look at the SAXS pattern of nanogratings and surface ripples in Figure 4.14 (c) qualitative differences in the scattering response appear. First the streak of the surface ripples is well aligned perpendicular to the laser polarization but with less anisotropy in contrast to nanogratings. By analyzing the feature sizes a thickness of grating planes of about (40 ± 3) nm is found. Perpendicular to the laser polarization (or streak direction) feature sizes of about (185 ± 9) nm are measured. This corresponds to an aspect ratio of 4.6 in contrast to the aspect ratio of pores found in the bulk of silica of about 7 [146]. Moreover, at this low pulse energy of 50 nJ the surface grating is well established with regularly ordered planes as the clearly visible diffraction peaks indicate (yellow spots

close to the beam stop). The peak position corresponds to a mean period of (130 ± 5) nm. Contrary to this, diffraction peaks are hardly visible in the scattering pattern of nanogratings while the grating planes itself are well aligned as the anisotropic streak indicates. However, the low pulse energy is close to the nanograting threshold in the bulk resulting in a low number of coherently ordered grating planes (see e.g. Fig. 3.8 (a)) which in turn prohibit strong diffraction.

While the differences in grating quality may be due to the smaller modification threshold at the surface of about one order of magnitude [147, 46, 148], the results indicate similarities in the morphology and evolution of periodic structures within the bulk and at the surface of silica. In agreement with bulk nanogratings the formation of fine ripples is typically ascribed to the nanoplasmonic theory [149, 74]. However, the deviation of the measured ripple period from the proposed value of $\lambda/2n$ found here and by other groups [143, 150] suggests to refine theoretical considerations. A recent publication links the formation of fine ripples to the coherent superposition between the scattered near field (evanescent field) and the refracted field provoking the initial energy absorption while the subsequent growth of ripples is triggered by a feedback-driven evolution of the surface topography [151]. By involving similar physics such as interference between incident and scattered waves together with an increase in number of laser-induced inhomogeneities from pulse to pulse an explanation for the continuous reduction of the period of volume nanogratings was proposed lately [77].

4.5 Nanostructures in different glasses

Since the first discovery of nanogratings most studies were performed in fused silica where the underlying nanograting structure was obtained first [12]. Only a few report on nanogratings in different materials such as doped silica [152] or even crystals [153]. Recently also nanogratings in semiconductors with indirect bandgap [154, 155] were observed.

To gain a deeper insight in the formation of nanogratings in dependence of the material composition at first common glasses such as ULE (Corning), which is silica glass with a fraction of TiO_2 providing a low thermal expansion, and the borosilicate glasses BK7 (Schott) and Borofloat 33 (Schott) are studied. Subsequently, the nanostructure emergence

and characteristics in doped glass samples with stepwise increasing doping percentage are investigated.

4.5.1 Common glasses

When the material composition changes both the different electronic recombination times as well as thermal properties of the glass may influence the principal formation threshold as well as the characteristics of nanostructures. Thus various glasses were illuminated with pulses of different pulse duration provided by a tunable laser oscillator (Femtosource XL 500, Femtolasers GmbH) emitting pulses at a laser wavelength of 800 nm. An aspheric lens (Thorlabs C230 TME-B, NA - 0.55) served to focus the pulses in the bulk using a pulse energy of 400 nJ and a pulse repetition rate of 100 kHz. The speed of the sample movement was 1.7 mm/s and the beam spot size 1.3 µm resulting in an overlap of about 800 pulses per spot. By tuning the position of the compressor prisms, the pulse duration was varied from 50 fs up to 450 fs which has been confirmed by FROG (Grenouille, Swamp Optics) measurements.
The measured optical retardance (at 633 nm) together with the standard deviation gained by repeated writing with the same laser parameters is shown in Figure 4.15 (a). In contrast to the increasing retardance for fused silica, ULE shows only a weak dependence on the pulse duration. When the pulse duration is larger than 150 fs almost the same retardance is measured for ULE and pristine silica. However, the borosilicate glasses (BK7, Borofloat 33) show significantly smaller birefringence. Both exhibit their maximum birefringence between 120 fs and 200 fs.
An explanation for the about 10 times smaller birefringence is given by the SEM images after polishing and etching in Figure 4.15 (b) and (c). The nanograting in ULE (pulse energy 200 nJ, pulse duration 120 fs) is characterized by regular and well established grating planes with a period of about 250 nm matching the prediction by the nanoplasmonic theory of 270 nm (n=1.48). In contrast, the period in Borofloat 33 is only about 60 nm while the grating planes are quite thin and barely established. This results in a reduced filling fraction between the grating planes and the surrounding material which, together with the reduced period explains the small retardance. In addition, the reduced presence of color centers [156] might impede the feedback process during the inscription.
When changing the material composition the different thermal properties are expected to change the nanostructure formation in dependence of the temporal pulse sequence. For

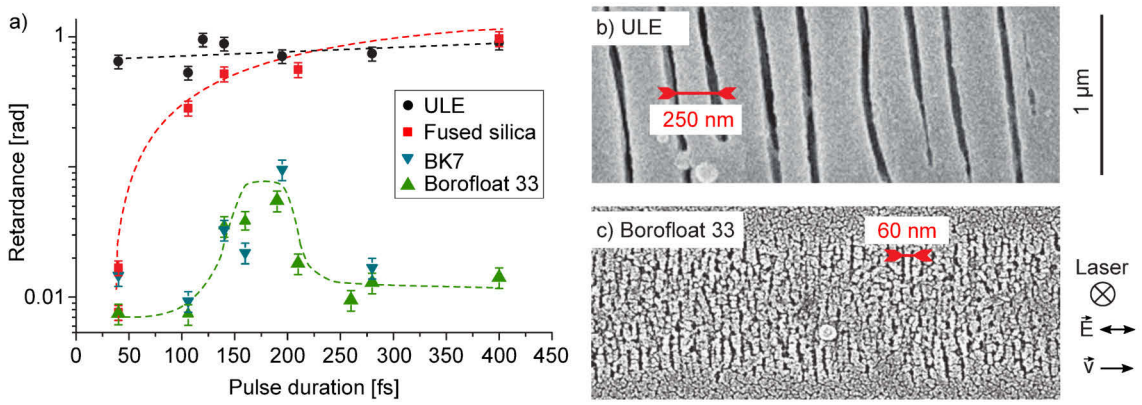

Fig. 4.15: (a) Retardance as function of the pulse duration for various glasses. The dashed lines represent a guide-to-the-eye. SEM images after polishing and etching of (b) ULE (pulse duration of 120 fs, pulse energy of 200 nJ) and (c) Borofloat 33 (pulse duration of 400 fs and pulse energy of 400 nJ).

instance, the smaller softening point of Borofloat 33 (820 °C [39]) and reduced thermal conductivity in contrast to fused silica leads to larger heat affected regions [157] while the smaller viscosity during processing prohibits the formation of microscopic disruptions [138]. To this end, inscription was performed using the frequency-doubled light (wavelength of 515 nm) of a mode-locked oscillator (Amplitude Systemes, t-pulse 500) emitting pulses with a pulse duration of 450 fs at a repetition rate of 9.4 MHz. Different laser repetition rates were set using an external acousto-optical modulator. The pulse overlap was kept constant (10^3 pulses per spot) by adjusting the speed of the sample movement correspondingly. Figure 4.16 depicts the measured retardance for nanogratings inscribed with a pulse energy of 150 nJ and an aspheric lens with a numerical aperture of 0.55. In addition to the previously studied glasses germanium doped silica (doping concentration 19 wt.%) was analyzed which is a commonly used glass for optical fiber applications such as highly doped multimode fibers or dispersion compensation.

At low repetition rates the measured retardance barely changes for all glasses. The highest retardance is observed for germanium doped silica which will be studied in more detail in Section 4.5.4.

When increasing the repetition rate all glasses show strongly decreasing retardance due to heat accumulation. However, the exact repetition rate were the optical retardance vanishes differs strongly. A large influence on this threshold is given by the thermal properties of the glass such as the material density, heat capacity and thermal conductivity defining the

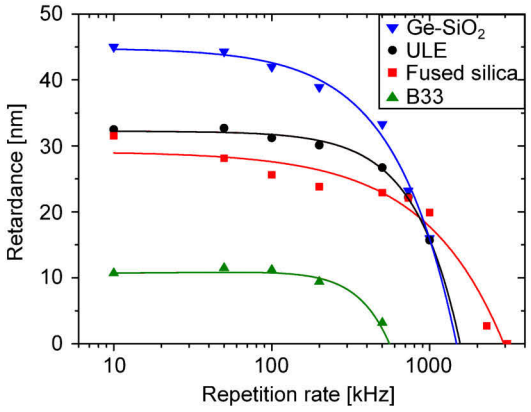

Fig. 4.16: Measured retardance as function of the repetition rate for germanium doped silica (doping concentration 19 wt.%), ULE, fused silica and Borofloat 33 (B33). The solid lines represent a guide-to-the-eye.

thermal diffusivity (D) of the glass (see Section 2.3). While fused silica exhibits a diffusivity of $8.1{\cdot}10^{-7}\,\frac{m^2}{s}$, ULE and Ge-doped silica show values of $7.7{\cdot}10^{-7}\,\frac{m^2}{s}$ and $7.3{\cdot}10^{-7}\,\frac{m^2}{s}$ [40, 117, 158]. The lowest diffusivity of $6.1{\cdot}10^{-7}\,\frac{m^2}{s}$ is given for Borofloat 33 [39], while, when comparing with Figure 4.16, heat accumulation sets in at lower repetition rate for Borofloat 33 in contrast to the other glasses. This indicates that the particular thermal diffusivity of the glasses reflect the upper threshold for nanograting formation in dependence of the laser repetition rate [136]. However, the particular effect of heat accumulation also depends on other parameters, in particular on the absorption of the individual laser pulses [52, 97].

In summary, the material properties strongly influence both the laser parameter region where nanogratings form as well as their actual morphology (filling fraction, pore dimension and period) which in turn lead to macroscopic birefringence. The latter will be studied in more detail in the following section.

4.5.2 Nanostructure formation in borosilicate glass

To uncover the underlying structure of nanostructures induced in the bulk of borosilicate glass SAXS and FIB-SEM were utilized. Due to the narrow parameter window (see Fig. 4.15(a)) inscription was performed with a regeneratively amplified Ti:sapphire laser system (Coherent Mira/RegA) operating at 800 nm laser wavelength delivering pulses with a pulse duration of 150 fs at 100 kHz repetition rate. A microscope objective (NA 0.35, spot diameter 1.5 µm) served to focus the pulses in the bulk of Borofloat 33 (Schott). By

stacking of 5 individual layers with a layer distance of 3 µm ensured sufficient scattering signal in the SAXS measurements. In addition, exposure times in SAXS had to be set to several tens of seconds to obtain significant scattering signal reflecting less scattering features within the probed volume.

The resulting false-color map of birefringence is shown in Figure 4.17 (a) showing the dependence on pulse number and pulse energy, respectively. The retardance strongly grows as function of the pulse number as known from fused silica. However, the maximal total retardance of about 30 nm (for 5 layers) corresponds to only 6 nm retardance per layer and is maximal at a pulse energy of 165 nJ. For larger pulse energies the birefringence gradually decreases in accordance with the Porod invariant measured by SAXS (see Fig. 4.17 (b)). Simultaneously, the number of sheets found in SEM (see Fig. 4.17 (c)) reduces. This trend is even more visible at low overlap (50 pulses) where no retardance above 230 nJ is measured.

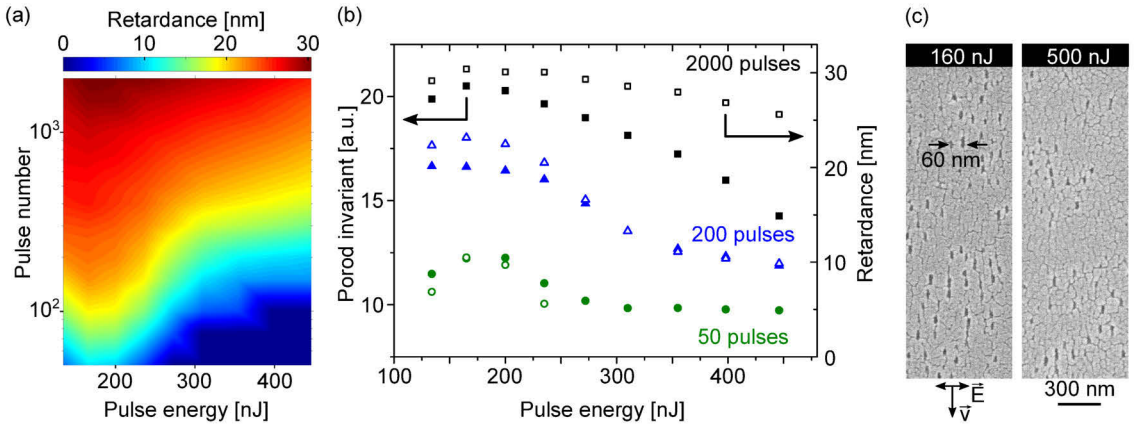

Fig. 4.17: (a) False-color plot of the measured optical retardance. (b) Porod invariant (full symbols, left axis) and retardance (empty symbols, right axis) of nanogratings in Borofloat 33 for different pulse numbers. (c) SEM images after polishing and etching after 2000 pulses per spot. Please note that fine and randomly aligned scratches in the SEM images are due to the gold coating applied for the SEM imaging.

A detailed view on the laser-induced morphology is given by the SAXS pattern in Figure 4.18 (a) and (b). First of all, a ring of intensity maxima (C) exists around the position of the direct beam. This ring describes a correlation of objects within a distance of 32 nm. Since it appears already in the untreated glass and does not change with illumination it points towards natural glass inhomogeneities presumably as a result of the glass fabrication process [30]. This is confirmed by further SAXS measurements of the same glass

type but from a different charge which do not show this feature (C). However, these inhomogeneities strongly affect the induced nanostructure and will be discussed in more detail below.

Along the horizontal direction of the pattern (y) the main streak accounts for the well-known vertical sheets of pores (S). Close to center (and the beam stop), the decreasing intensity (L) in particular in vertical direction (x) describes large features with lengths of several hundred nanometers. The SEM image in Figure 4.18 (c) allows to identify the length scales in etched cross sections to about 400 nm.

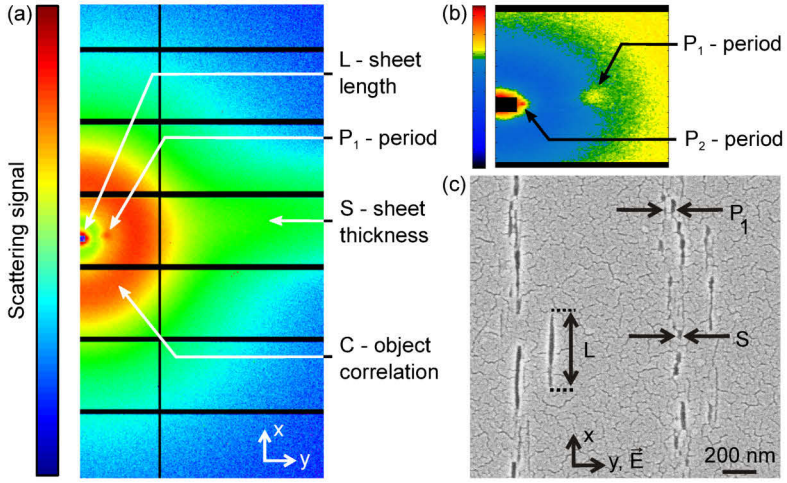

Fig. 4.18: (a) Scattering pattern and (b) corresponding zoom and (c) SEM image after polishing and etching for nanogratings (2000 pulses, pulse energy 130 nJ); typical features are marked.

Applying several hundreds of laser pulses, two sharp peaks close to the center show up (see Fig. 4.18 (b)). These confirm the assembling of periodic grating planes P_1 and P_2. The characteristic diffraction peak P_1 corresponds to a period of about 50 nm and appears after about 300 pulses (see Fig. 4.19 (a)). When the laser exposure continues, the period slightly increases and saturates at 57 nm while becoming more distinct. Remarkably, this periodicity is in the range of $\lambda/10n$ (here 55 nm) and has never been measured for bulk nanogratings before. The FIB-SEM image in Figure 4.19 (c) and the SEM image after etching (see Fig. 4.17 (c)) confirm the period found.

In contrast, the large period P_2 is much weaker and appears only at higher number of pulses (> 500) and low pulse energies. In addition, the period could not be obtained in SEM images. However, the period of about 300 nm is in the range of $\lambda/2n$ (273 nm) and slightly decreases with illumination as known for fused silica. P_1 can not be a higher order

(e.g. 5th order) of the peak P_2 since it appears first, is more distinctive and no intermediate peaks are found. The weak appearance of the P_2 period together with the strongly reduced period P_1 is a result of the fact that the glass itself exhibits intrinsic inhomogeneities. This is confirmed by further SAXS measurements as well as studies of other groups using the same glass type which reveal the conventional periodicity only (in the range of λ/2n) as known from silica [136]. As recently proposed in [77] when the concentration of inhomogeneities increases the periodicity of the imprinted grating structure decreases significantly (e.g. period of λ/4n at a concentration of 5 %). This together with the modified periodicity measured here is a hint that intrinsic structural properties dictate the assembling of anisotropic pores.

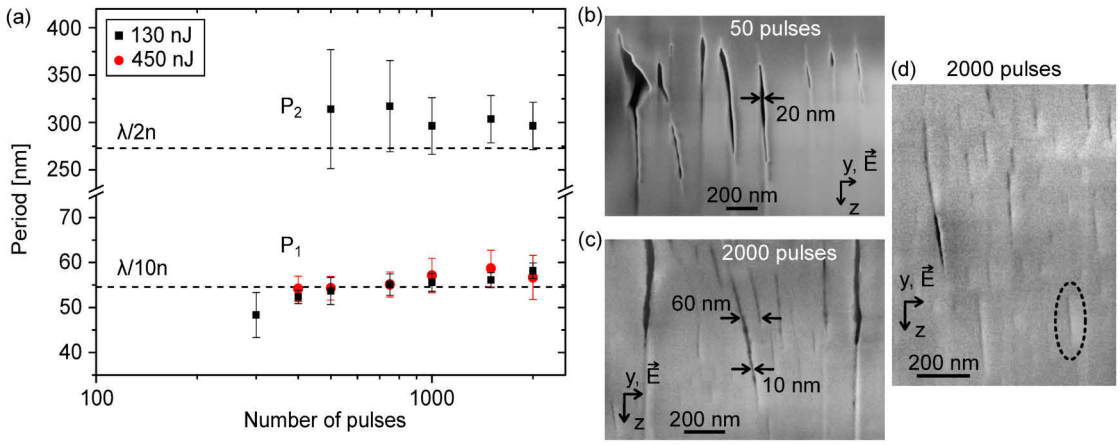

Fig. 4.19: (a) Period of nanogratings measured by SAXS for a pulse energy of 130 nJ and 450 nJ. SEM image in the z-y-plane after FIB-milling for nanogratings inscribed with 500 nJ and (b) 50 pulses and (c), (d) 2000 pulses per spot. Typical feature sizes are marked.

The strongly different thermomechanical properties of Borofloat 33 influence the dimensions of the laser-induced pores. When analyzing the streak (S) using the unified scattering intensity feature sizes of 10 nm are found which remain constant independent of the applied laser pulses as well as of the pulse energy. In the SEM images of Figure 4.19 (b) and (c) pores with diameters of 10-20 nm are found for all stages of the grating formation. With ongoing irradiation small sheets with a thickness of 10 nm and even below add. These fine scratches can be obtained in Figure 4.19 (c) and (d) (e.g. marked by the dashed ellipse). This is in contrast to the pore thickness of 28 nm found in fused silica. With its lower melting point and thus lower viscosity during heating (10^2 Pa·s at 2000 °C in contrast to 10^8 Pa·s for fused silica [159]) borosilicate reacts plasticly on thermoelastic forces.

Hence the decomposition of the glass into a porous structure is hindered [152] leading to a strong reduction of the number of pores and hence lower retardance in contrast to silica. The thickness of pores, however, is barely influenced by the inhomogeneities as confirmed by SAXS measurements of Borofloat 33 from a different charge (without isotropic feature C) [136]. These samples show slightly larger values for the pore thickness of 15 nm.
Large-scale structures (L in Fig. 4.18) were obtained in SAXS for all pulse energies (130-450) nJ at high pulse numbers (≥ 1500). The length of 400 nm agrees with the extension of cracks in the SEM image in Figure 4.18. For larger pulse energies than 250 nJ the sheet length measured by SAXS slightly decreases to 360 nm which might be a result of larger temperatures resulting in pronounced reflow during solidification [160, 138]. Thus, large sheets are barely found at high pulse energies in the SEM image of Figure 4.17 (b).

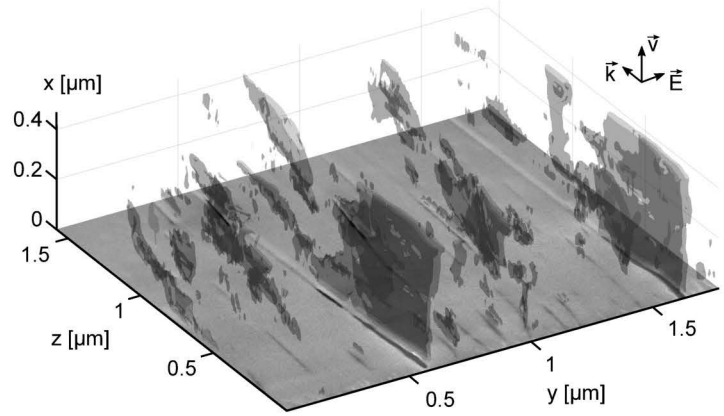

Fig. 4.20: 3D reconstruction of 31 SEM images after FIB milling. One exemplary SEM image is shown in the z-y-plane

To visualize the 3D alignment of nanogratings (inscribed with 2000 pulses per spot and a pulse energy of 500 nJ) a volume of (1.8 x 1.8 x 0.5) μm^3 was dissected by FIB using a slice thickness of 15 nm. The reconstruction in Figure 4.20 shows thin and extended sheets aligned perpendicular to the laser polarization. Due to the small feature size close to the image resolution (pixel size 3.7 nm) mostly pores with some 10-20 nm thickness are reconstructed. Along the x direction the pores are extended up to 400 nm in agreement with the SAXS measurements.
In summary, several outcomes for the material dependence of laser-induced nanogratings are gained by the investigation of laser-induced nanostructures in borosilicate. First, the cumulative effect of several hundreds of laser pulses does not affect the size of the pores while the formation of the grating occurs by continuous increase of the pore number

similar to fused silica. In contrast, the actual size of pores of about (10-20) nm and lengths up to 400 nm differs. In addition, the different characteristics of the glass such as the lower viscosity and hence weaker contraction during cooling impedes the decomposition into a porous structure. Thus the less pores and smaller filling fraction of the grating planes result in strongly reduced birefringence in contrast to fused silica. Remarkably, the laser-induced nanograting exhibits a strongly reduced periodicity in the range of 55 nm (λ/10n) that coexists with the predicted period of λ/2n within a certain laser parameter regime. The appearance of the small period is linked to intrinsic inhomogeneities within the glass matrix. This is a hint for the proposed connection between inhomogeneities and the feedback process [77].

4.5.3 Nanostructure formation in ULE glass

In contrast to borosilicate ULE is a binary glass that consists of SiO_2 with a TiO_2 fraction of about 7.5 wt% resulting in a thermal expansion coefficient close to zero in a temperature range from 5-35 °C [161]. Due to this property ULE has become an interesting material for applications where ultra-high geometrical stability is needed during operation such as substrates, supports or blanks. Moreover when processing ULE with ultrashort laser pulses strong form-birefringence as well as darkening, i.e. an increased absorption over the entire visual spectral range is obtained [162]. The latter is due to a photo-reduction of TiO_2 agents while the level of darkening can be set by tuning the laser parameters making ULE an interesting material for data storage purposes.

To explore the differences of nanostructure formation and their characteristics fields of (100 x 100) μm^2 were inscribed using a laser wavelength of 515 nm, a pulse duration of 450 fs, a repetition rate of 500 kHz and a focusing objective with a numerical aperture of 0.55. Figure 4.21 (a) shows the measured retardance comparing with nanogratings inscribed with the same laser parameters in fused silica.

Analogue to silica the retardance increases with the laser pulse energy. Comparing the influence of the number of pulses applied the birefringence grows in a logarithmic fashion but with a steeper slope which might be due to a change in the underlying grating structure during the cumulative action of several laser pulses.

Having a closer look to the microscopic properties, the induced nanogratings show similar characteristics as fused silica. Figure 4.21 (b) shows the thickness of pores as well as their mean distance (period) measured by SAXS. The measurements confirm that the nanograt-

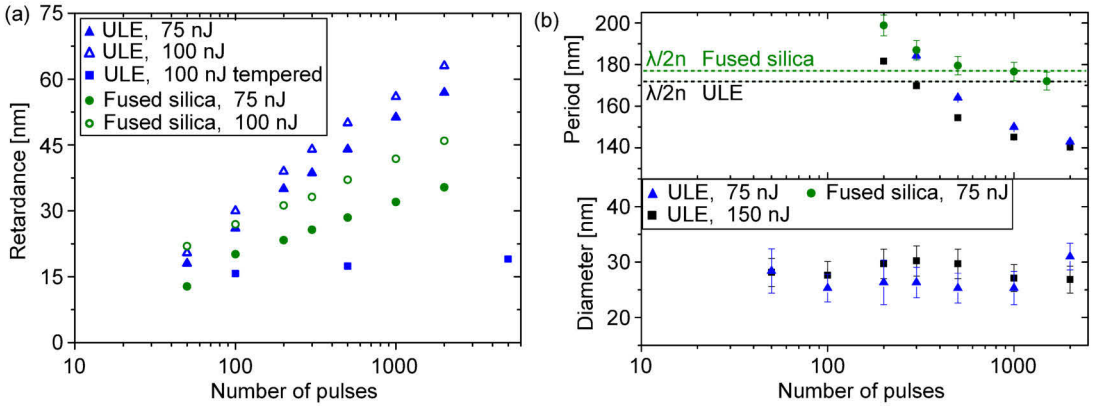

Fig. 4.21: (a) Optical retardance of nanogratings in ULE for different pulse energies. The green markers denote the retardance measured for fused silica using the same laser parameters. The blue squares mark the retardance of laser-irradiated ULE after annealing for 600 s at 1200 °C. (b) Results of the SAXS measurements showing the period (upper) and thickness of pores in ULE (lower).

ings are composed of voids which explains the remaining optical retardance after annealing the laser-irradiated sample far above the annealing point of the glass (1000 °C [158]) where strain relaxes rapidly (see Fig. 4.21 (a)). The laser-induced pores exhibit a typical thickness of 30 nm remaining constant during illumination. This matches the thickness of pores measured in fused silica. The transversal length of pores (along x in Fig. 4.22) is 269 nm and 33 nm resulting in a slightly increased aspect ratio of 9 in contrast to 7 for silica (compare with Fig. 4.8 (b)). However, the length of pores remains constant during illumination and hence can not explain the strong increase in birefringence. Most likely the number of pores increases faster as for fused silica which is illustrated by the steeper slope of optical retardance that scales with the Porod invariant (see Fig. 4.17 (b), [61]). In addition, the period decreases with increasing number of laser pulses and approaches 140 nm after 2000 shots. This is well below λ/2n (173 nm with n=1.49 at 515 nm [158]) with a more faster decrease as in silica. Based on the faster increase in number of pores, the higher filling fraction of grating planes could influence the reduction of the period. This might be due to pronounced scattering at existing grating planes mediating smaller periods below λ/2n as proposed in [96].

Complementary analysis of the microscopic characteristics was performed by acquiring FIB-SEM images for nanogratings inscribed with a pulse energy of 150 nJ (otherwise same laser parameters as before) and a pulse overlap corresponding to 50 and 2000 pulses per spot. Figure 4.22 shows the reconstructed nanograting structure (volume of (1 x 1 x

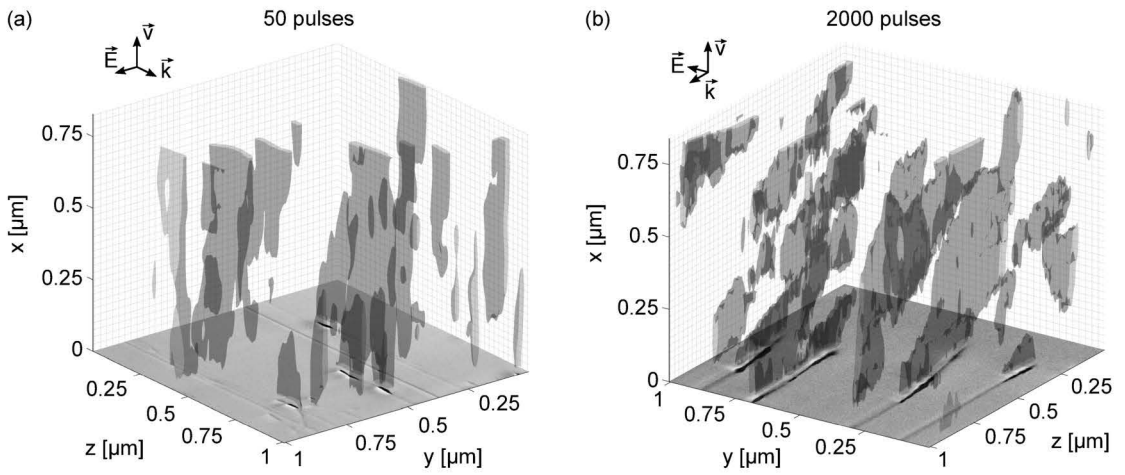

Fig. 4.22: Reconstruction of nanogratings in ULE inscribed with (a) 50 pulses and (b) 2000 pulses per spot. One exemplary SEM image is shown in the z-y-plane.

0.8) μm^3) for (a) 50 and (b) 2000 pulses while the distance of adjacent slices was 23 nm (50 pulses) and 28 nm (2000 pulses).

When comparing the reconstructed pore topology the number of pores increases with illumination as expected. The pores link together to form individual grating planes with a period of about 150 nm after 2000 pulses. The width of pores is about 30 nm and several hundreds of nanometers along the other dimensions. Compared with nanogratings in silica (see Fig. 4.4 (e)) the pores are significantly larger along x in agreement with the SAXS measurements.

The structure of ULE is similar to fused silica, with titanium atoms replacing some silicon which adds disorder. Laser-irradiation leads to bond breaking of Ti-O-Si bonds reducing the number of TiO_4 tetrahedra. Similar to vitreous silica oxygen recombines and is kept within microscopic voids [162]. However, some oxygen ions of the glass network are oxidized while a photo-reduction Ti^{4+} to Ti^{3+} occurs during illumination. This trivalent titanium is responsible for the darkening of the glass since it exhibits a broad absorption band at 790 nm. Under the cumulative action of several hundreds of laser pulses this broad absorption may mediate the feedback process triggering a faster increase in the number of anisotropic voids which presumably affects the resulting periodicity. Due to the larger filling fraction of grating planes the birefringence is increased in contrast to silica.

4.5.4 Glass density behavior on fictive temperature

The previous results of nanogratings in ULE or borosilicate demonstrate that the formation of anisotropic pores as well as their alignment depends on glass structural properties (e.g. intrinsic inhomogeneities), defect-assisted absorption as well as thermomechanical properties such as the viscosity or Young's modulus of the glass. In addition, the particular effect of the thermomechanical properties on the imprinted grating structure may also be influenced by the structural relaxation of the glass in terms of the glass density behavior on the fictive temperature (T_f) [95]. As shown in Figure 2.1 rapid cooling may result in strongly different glass density behavior in contrast to the unmodified material (e.g. in the surrounding of the laser focus). In case of silica the increase in material density is accompanied by tensile stress which was assumed to cause the formation of microscopic pores [21, 40]. Thus, to determine the influence of the glass density behavior on the fictive temperature on the induced nanostructure, laser-irradiated silica glasses with stepwise increasing germanium percentage (each exhibiting different expansion behavior) were studied.

To this end, several kinds of germanium-doped silica glass samples ($xGeO_2$-(1-x)SiO_2, x denotes the GeO_2 content) were produced by Chemical Vapor Deposition (PCVD) with different doping percentage varying from 2.2, 5.3, 12.5, to 19 wt.% of germanium. These samples are optical fiber preforms with standard compositions typically used for optical fiber applications, i.e. photosensitive optical fibers for gain flattening, highly doped multimode fibers, dispersion compensation or Bragg filters. Their density dependence on T_f has been reported in [40]. While pristine silica and 2.2 wt.% Ge-doped silica follow an anomalous trend, a fraction of 5.3 wt.% or higher leads to normal behavior, i.e. higher density with lower fictive temperature. After cutting and polishing the glass samples multiple lines with a distance of 3 µm were inscribed using pulses with a duration of 450 fs (laser wavelength of 515 nm), a pulse energy of 150 nJ and a focusing objective with a numerical aperture of 0.55. The photo-induced birefringence in dependence of the repetition rate and pulse number is shown in Figure 4.23.

When increasing the repetition rate and keeping the number of pulses per spot constant at 10^3, the retardance continuously decreases due to heat accumulation. Comparing different doping concentrations the relative retardance decay increases with the germanium content leading to smaller birefringence at 1 MHz for higher doping. Presumably this is due to increasing glass density from 2200 kg/m^3 for pure silica to 2450 kg/m^3 for 19 wt.%

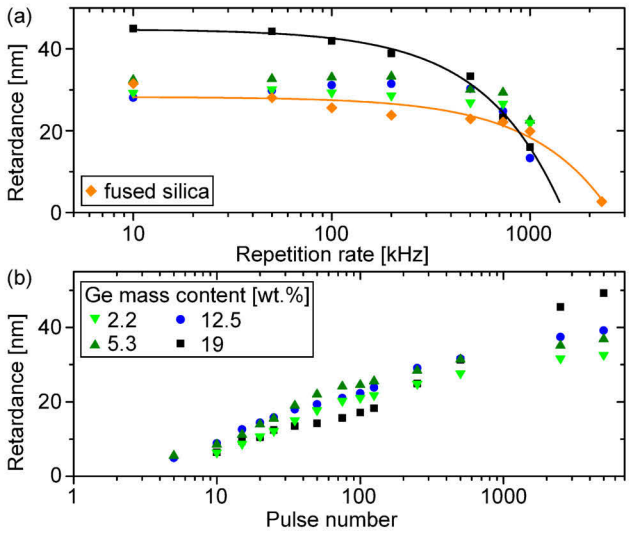

Fig. 4.23: Retardance of nanogratings inscribed in Ge-doped glasses (0 wt.% corresponds to fused silica). (a) Dependence on the repetition rate (with guide-to-the-eye for 0 and 19 wt.%) for 10^3 pulses per laser spot and (b) on the pulse number (repetition rate 50 kHz).

doped glass. In contrast, the slight increase in both heat capacity and thermal conductivity is negligible. Thus the thermal diffusivity (see Section 2.3) decreases with increasing doping. This leads to stronger accumulation of heat in between two consecutive pulses. Still, increasing doping leads to stronger birefringence as measured at low repetition rate (e.g. 50 kHz). This trend is also visible in Figure 4.23 (b) for high number of pulses (> 500).

The difference in birefringence is directly linked to different grating structures. Figure 4.24 (a) shows the results of the SAXS measurements, which reveal that the period significantly decreases from about 165 nm to 120 nm for rising doping concentration. Simultaneously the error bars shrink as well, reflecting better order of the grating planes. The reduction in period can not be explained by a change in refractive index of the bulk glass due to the doping, which only changes from 1.46 (2.2 wt.%) to 1.49 (19 wt.%) at a wavelength of 515 nm. This trend is confirmed by other groups [163]. However, the SAXS measurements reveal that the period starts with almost the same value of 210 nm ± 15 nm (at 100 pulses per spot). Thus, the shift is due to the cumulative action of several hundreds of consecutive laser pulses. During this evolution the retardance increases stronger for larger doping concentration. Both the higher retardance (and hence number of pores [133]) and reduced periodicity in contrast to silica agree with observations of

nanogratings in ULE (see Section 4.5.3) affirming the link between the filling fraction of grating planes and their mean distance (period).

When increasing the doping concentration the aspect ratio of pores increases from 7 (for fused silica) to 17 (at 19 wt.%). The pore thickness decreases from 28 nm to 18 nm at 12.5 wt.%. This is in agreement with the pore thickness found by FIB-SEM in Figure 4.24 (b). Comparing with pristine GeO_2, Asai et al. measured an even smaller pore size of 10 nm [164] as well as an increased filling factor compared to fused silica. Here the

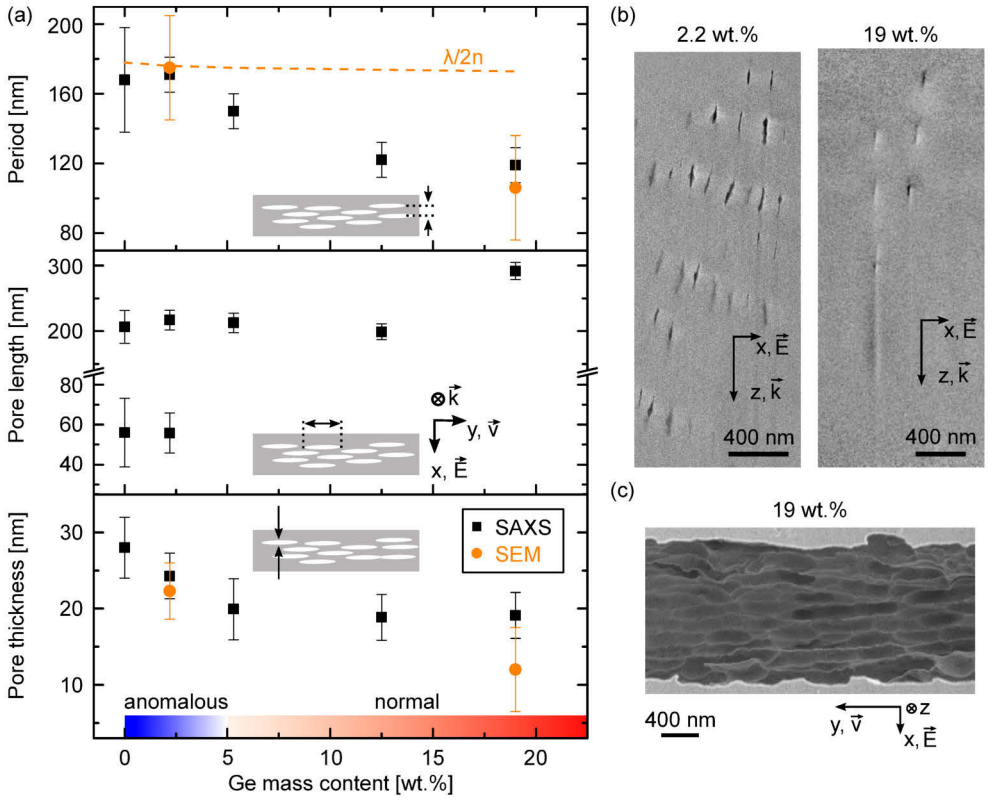

Fig. 4.24: (a) Results of the SAXS measurements: period, pore length and pore thickness as function of the doping concentration. The corresponding regime of density behavior on T_f (normal or anomalous) is indicated by the colorbar. 0 wt.% corresponds to fused silica. The dashed line indicates the predicted period taking the change in refractive index into account. (b) FIB-SEM images of nanogratings inscribed with a pulse energy of 150 nJ, a repetition rate of 50 kHz and 5000 pulses per spot in Ge-doped silica with 2.2 and 19 wt.% doping concentration. (c) SEM image after polishing and etching (in 1 % hydrofluoric acid for 90 s) of silica with a fraction 19 wt.% germanium.

length of pores increases to about 300 nm for high germanium doping. In addition, at high doping concentration the scattering signal in SAXS is reproduced by one single size

distribution, while at low concentration a second size is needed for quantitative fits (see Fig. 4.24 (a)). This points to a more dense grating structure with large pores resulting in higher form-birefringence.
In summary, when increasing the germanium doping concentration a modified pore morphology with larger aspect ratio and a stronger decomposition of the glass under laser-irradiation is obtained. The change in glass density behavior on the fictive temperature is associated with the different doping concentrations does not change the nanostructure occurrence in a general term. This is confirmed by the emergence of nanogratings in Borofloat 33 which exhibits normal behavior as well. Correspondingly the nanopores may form and grow (as obtained in Chapter 4) on shorter timescales as the heating and quenching of the lattice [8, 52]. The rapid ionization is accompanied by bond breaking and dissociation of silica and the formation of molecular oxygen as measured in Section 3.3. As a result the refractive index decreases which can be interpreted as irreversible volume expansion leading to a rarefied glass matrix. Due to the opposite response of elastic strain compressive stress in the focal volume is generated.
Another scenario that results in a refractive index decrease may be that the matter in between the nanopores is composed of silica with a significant amount of Frenkel oxygen defects $O_0^x \rightarrow V_0^{2+} + O_i^{2-}$ (a vacancy and an interstitial oxygen). This process is assumed to be enhanced in Ge-doped silica since it is much easier to induce these defect centers during reduction. In order to confirm their occurrence optical absorbance UV-Vis spectroscopy is used.
Figure 4.25 shows the recorded absorbance spectra (log(1/T), where T denotes the transmission) from 190 nm to 2000 nm after subtracting the background from the pristine host material. After irradiation the signature of different point type defects dominate the spectra [33]. The spectrum of modified silica shows distinct bands which can be attributed to SiE'- centers and NBOHC's as obtained in Figure 3.10 (a). However, by increasing the doping concentration silicon is replaced by germanium acting as a glass former in the network. Consequently, laser-irradiation leads to bond breaking of GeO_4 tetrahedrons resulting in point defects analogue to pristine silica but with slightly different characteristics.
Most obviously a band due to Ge-ODC(II) (oxygen deficiency center) around 5 eV (240 nm) [165] adds to the spectrum of modified silica. In contrast, the peak at 6.3 eV (196 nm) which is due to GeE'- centers can hardly be resolved because of the increasing absorbance in the VUV range that is close to the band edge. By increasing the doping concentration

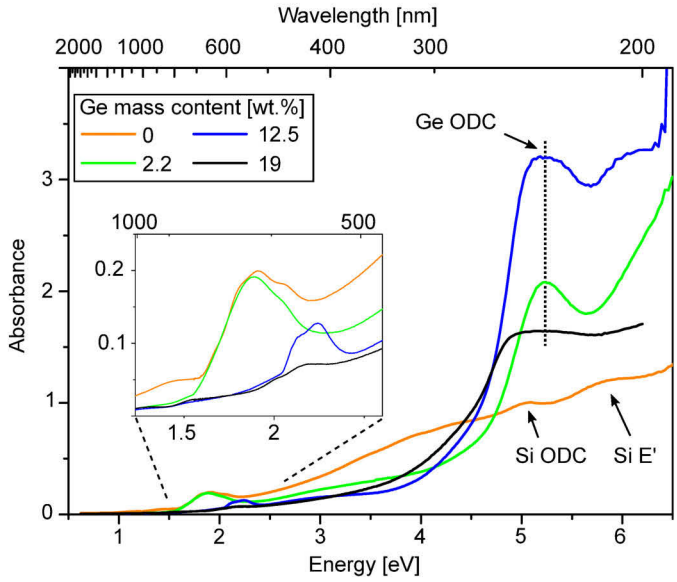

Fig. 4.25: Optical absorbance spectra of laser modified regions (background corrected) in glasses with different doping concentrations. The inset shows a zoom of the spectra.

the low-energy band due to NBOHC's (for pristine silica at 1.9 eV (652 nm)) blue shifts while decreasing in signal. The NBOHC's gives rise to strong photoluminescence (PL) as shown for fused silica in Figure 3.10 (b). However, the PL signal of NBOHC's red shifts from 650 nm (fused silica) to 689 nm (for 19 wt.%) which together with the shift of the absorption band reflects the change in network environment [165].

The observation of bond type defects confirm the decomposition of Ge-doped silica into under-stochiometric silica. These defects mediate the feedback process towards a regular grating structure but do hardly affect the actual morphology of nanopores. However, for applications such as photonic functionalities within optical fibers the optical attenuation mainly in the UV range has to be taken into account.

4.6 New model of nanograting formation

To summarize, the formation of nanogratings is a step-wise process from pulse to pulse while the particular laser-driven excitation as well as the subsequent evolution resulting in permanent material modifications are equally important. Combining SAXS, FIB-SEM and optical retardance measurements uncover that nanogratings consist of sheet-like cavities which form, increase in number and assemble in regular grating bars during ongoing illumination. The sequential formation mechanism of nanogratings can be described by four distinct phases.

1. Focused single ultrashort laser pulses result in isotropic cylindrical voids which emerge entirely deterministic without the need for preexisting seeds or material inhomogeneities. Their shape and size is given by the laser intensity distribution. However, thermomechanical properties such as viscosity and Young's modulus of the glass influence the occurrence as reported by Gamaly et al. [9]. Thus, for glasses where void formation is hardly obtained, such as borosilicate [138], also nanograting formation is hindered [61].

2. With ongoing irradiation repeated heating and quenching of the glass as well as material deformation due to laser-induced micro-explosions occurs. As a result randomly aligned inhomogeneities embedded in a modified glass matrix (e.g. densified in case of fused silica) form.

3. These inhomogeneities allow to nucleate the formation of small anisotropic pores which grow to a size of about (200 x 30 x 300) nm^3 in fused silica. The growth is driven by field enhancement perpendicular to the laser polarization mediated by defect formation reducing the ionization threshold from pulse to pulse [15, 95, 24]. The polarization-driven feedback is quite strong and even allows for inscribing a new grating over an already existing nanograting.

4. After a multitude of anisotropic pores have formed these align exactly perpendicular to the polarization direction and strongly increase in number. This process is most likely driven by a cavity-like amplification process as suggested in [73, 15]. Based on repeated heating and quenching a more porous glass is formed. The continuous reduction of the period (even below λ/2n) occurs due to alternative effects such as the coherent superposition of the scattered field from existing grating planes

which may lead to the emergence of a new grating plane in between [96]. Hence the average distance of grating planes continuously decreases. A higher number of pores and thus a larger filling fraction of grating planes favor this process due to pronounced scattering leading to smaller periods. This is confirmed by repeated rewriting of nanogratings. Since rewriting is no ideal process remaining pores or glass inhomogeneities add with increasing number of rewrites resulting in smaller periods. In addition, the glass ability to decompose regulates the speed of the period reduction as observed for nanogratings in ULE and germanium doped glasses.

The formation sequence is basically independent of the inscription regime (e.g. point-wise or scanning the laser focus) following the same path from stress-driven (phase 1 and 2) to polarization-driven (phase 3 and 4). However, when scanning the laser focus through the glass less pulses are required to form a regular nanograting in contrast to point-wise inscription. During phase 2 stress along the scanned path increases leading to the formation of cracks. These cracks favor the formation of anisotropic pores in particular when the polarization is perpendicular to the scanning direction resulting in increased retardance in contrast to all other polarization directions. Thus, for point-wise inscription more pulses are required to form a regular nanograting due to the absence of seeds (no elongated cracks appear) which is confirmed by the in-situ measurements of the optical diffraction.

Nanogratings induced by ultrashort laser pulses can be induced in various glasses ranging from multicomponent glasses such as Borofloat 33 up to silica glasses, pristine or doped with germanium or titanium. In all of the investigated glasses a porous nanostructure builds the primary constituents of nanogratings independent of the glass density behavior on the fictive temperature. First, this confirms that nanogratings are no special feature of fused silica. Moreover, the grating formation occurs analogue to pristine silica via increasing number of pores while the size of the pores (after their initial formation) barely changes during illumination.

Basic glass properties, however, were found to influence both the formation threshold as well as the microscopic features of the induced nanopore morphology and thus the macroscopical birefringence. Thermomechanical properties (thermal conductivity, glass density and heat capacity) define the threshold for heat accumulation and so the upper threshold for nanograting formation in dependence of the laser repetition rate. The actual size of pores as well as their number is influenced by the glass viscosity and mechanical proper-

ties (e.g. shear modulus [136]) defining the glass ability to decompose. This explains in part the significantly reduced retardance in Borofloat 33. The absorption of the individual laser pulses leads to rapid ionization and bond breaking defects which in turn mediate the formation of the grating via ongoing decomposition. Thus, a lower nanograting threshold (as it is the case for Ge-doped silica) or the photo-reduction of titanium agents (ULE) can support the formation of a more porous glass structure and hence a faster reduction of the period even below λ/2n.

Intriguingly, given a glass structure with a certain amount of inhomogeneities the average distance of the nanopores induced by ultrashort laser pulses may strongly change as observed for Borofloat 33 in this work and proposed in [77]. This agrees with observations of rewritten nanogratings in fused silica where remaining pores or glass inhomogeneities promote the nanograting formation and facilitates smaller periods after multiple rewrites. In addition, this proves the formation of feature sizes far below the wavelength of light and opens the door for vast (rewritable) photonic applications by tailoring the underlying grating characteristics and thus the optical response.

The formation of the pores themselves, however, is not fully understood yet and may happen via two scenarios. First, the decomposition of the glass under ultrashort laser irradiation may occur due to Coulombian nano-explosion [8]. This is based on the migration of oxygen due to Coulomb forces between highly ionized oxygen ions leading to fast volume expansion creating the pores [95]. However, the observation of nanogratings in normal glasses presumes that the process of oxygen migration is faster than the volume expansion of the glass given by the glass density behavior on the fictive temperature. The in-situ measurements of the optical diffraction give a hint for this revealing that the imprinting of the grating structure occurs on short temporal time scales below a few µs after the laser pulse was incident. An alternative approach describes the reduced density of the solid due to a laser-induced reduction of the average number of oxygen in the first silicon coordination shell [40]. To satisfy the lower coordination of silicon a porous glass structure forms even for glasses with normal glass density behavior on the fictive temperature. To obtain a deeper insight in the temporal sequence of pore formation, time-resolved measurements (within the X-ray regime) could be used to gain kinetic and structural information of the probed particle ensemble.

5 Application of laser-induced nanostructures

The local inscription of strong-form birefringence based on an anisotropic structure with feature sizes smaller than the wavelength of light opens up manifold prospects for tailored photonic functionalities. In particular, the direct writing approach together with the fact that basic grating properties such as the refractive index contrast (filling factor of the grating planes) or the period can be set by the laser parameters allow for implementing wave plates for almost arbitrary polarization manipulation, rewritable optical data storage devices or applications in the broad field of microfluidics just to name a few. Moreover, by combining with isotropic refractive index changes waveguide-based guiding and manipulation of light allows for complex photonic networks within one single glass chip.

This chapter first addresses the inscription of wave plates for polarization manipulation and the generation of optical vortices. Subsequently, applications in the field of structured illumination microscopy using polarization encoded lighting are presented.

5.1 Wave plates for polarization control

Starting with a simple approach, the laser-induced form-birefringence can be used for controlling the state of polarization when matching the induced optical retardance with respect to (e.g. the quarter or half of) the wavelength the wave plate is desired for. In this regard the spatially homogeneous polarization state of the input beam can be transferred to e.g. circular or (rotated) linear polarization depending on the input polarization [16]. In addition, achromatic wave plates can be fabricated by stacking of individual nanograting layers [166] which could enable broad band applications such as imaging at multiple wavelengths in the field of biomedicine [167].

Beyond wave plates with a fixed optical axis, sub-wavelength structures can be used for the transformation of incident linear or circular polarized light into radial or azimuthal polarization [168]. Radial polarization, for instance, provides a smaller transverse focal diameter ($0.16\lambda^2$) in contrast to linear ($0.26\lambda^2$) or circular polarization ($0.22\lambda^2$) [169, 170] enabling various applications in the field of microscopy [171, 172]. These so-called vector beams show polarization symmetry to the optical axis and exhibit a helical phase front resulting in a phase singularity on the axis. Thus, destructively interfering light components generate a dark central spot.

While first ideas for fabricating these sub-wavelength structures were based on metal-stripe gratings the basic concept can be applied to a special arrangement of nanogratings [66, 173]. In principle two types of polarization converters can be fabricated (see Fig. 5.1) depending on the the input polarization (circular (quarter-wave plate) or linear (half-wave plate), see Fig. 5.1 (a)). The quarter-wave plate transforms an incoming circularly polarized beam into a radially or azimuthally polarized optical vortex with orbital angular momentum (OAM) l=±2 [66]. In contrast, the half-wave plate generates either pure radial or azimuthal polarization (without OAM) for linear input polarization or an optical vortex (with OAM of l=±1) when illuminating with circular polarized light.

For the inscription of the quarter-wave plate the laser focus was scanned through the glass (line separation 0.4 µm) while the sample was rotated and simultaneously translated with a constant translation speed resulting in a spiral arrangement of the nanograting planes. The nanogratings were inscribed using a laser wavelength of 515 nm, a repetition rate of 500 kHz, a pulse energy of 150 nJ and an aspheric lens with a NA of 0.4. To keep the pulse overlap constant (translation velocity of 1.7 mm/s, 500 pulses per spot) the rotation speed needs to decrease, the larger the distance from the center becomes. Due to the limitations of the rotation axis this results in a small region with weak retardance in the center of the wave plate as Figure 5.1 (b) shows. However, this approach provides a fast and reliable way instead of point-wise inscription [17] resulting in a high beam quality.

The measured slow axis distribution is illustrated in Figure 5.1 (c) and indicates the spatially varying nanograting orientation. In addition, the SEM image after polishing and etching (see Fig. 5.1 (d)) of a wave plate inscribed with a repetition rate of 1 MHz, a pulse energy of 170 nJ, a line separation of 0.2 µm in combination with an aspheric lens with NA of 0.55 (otherwise same laser parameter as before) reveals an intriguing feature of nanogratings. Based on the spatial pulse overlap of about 67 % the grating planes continuously bend due to the varying polarization direction. These small and smoothly bended

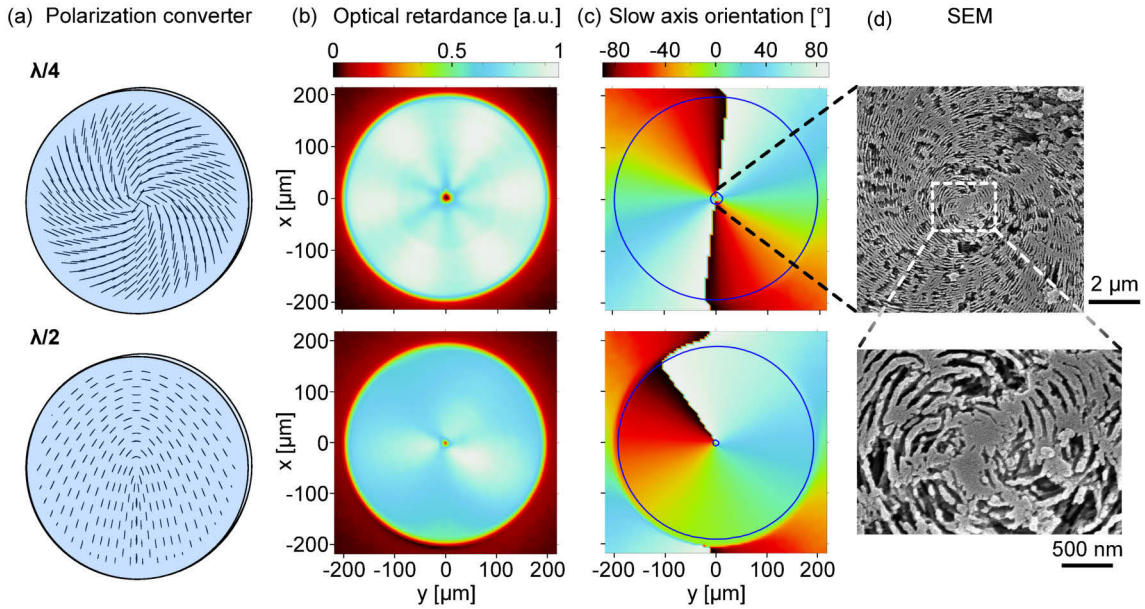

Fig. 5.1: Polarization converter for the generation of optical vortices. (a) Principle sketch of the nanograting orientation, (b) measured optical retardance and (c) slow axis orientation in quarter-wave (upper) and half-wave design (lower). The blue lines in (c) indicate the region of the wave plate in terms of iso-retardance lines. (d) SEM image of the nanograting structure of a quarter-wave plate after polishing and etching.

features can barely be fabricated by other methods such as electron beam lithography. Moreover, this approach can even be extended for the generation of vortices with higher optical charge [174].

In the case of the half-wave plate the sample and the input polarization is rotated simultaneously providing a rotation of the slow axis from -90° to 90° of the induced nanogratings as shown in Figure 5.1 (c) (lower). Due to the smaller rotation speed the area with reduced retardance in the center is smaller.

To evaluate the optical performance of the nanograting-based wave plates several nanograting layers were inscribed in order to match the optical retardance for the desired wavelength (633 nm). Figure 5.2 (a) shows the measured far-field patterns for the fabricated converter in half-wave (upper) and quarter-wave design (lower) when illuminating with linear and circular polarization, respectively. Both converters generate a ring-shaped intensity distribution with azimuthal (upper) and radial (lower) polarization while the corresponding polarization can be switched by the direction of the incident linear and handedness of the circular polarization. When introducing a polarizer in front of the camera the pure azimuthal polarization generated by the wave plate in half-wave design results in

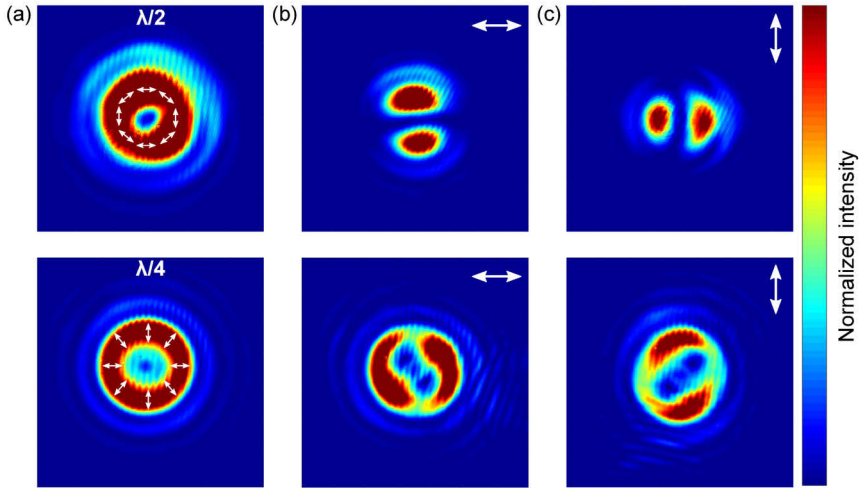

Fig. 5.2: Far-field pattern of fabricated wave plates in half-wave (upper) and quarter-wave design (lower) when illuminating with linear and circular polarization at a wavelength of 633 nm. The sub-figures show the (a) transmitted beam, with (b) horizontal and (c) vertical polarizer in between the converter and the camera (indicated by the white arrows). The white arrows in (a) illustrate the electromagnetic field-orientation.

a typical dumbbell shape that rotates with respect to the direction of the analyzer position (upper sub-figure of 5.2 (b) and (c)). In contrast, the optical vortex produced by the wave plate in quarter-wave design shows an 's' - shape as expected for double-charged optical vortices [66].

The results demonstrate the feasibility of nanograting-based wave plates for polarization manipulation and the generation of optical vortex beams. Moreover, the nanograting-based wave plates exhibit a high damage threshold of about 23 J/cm^2 (at a laser wavelength of 1064 nm and a pulse duration of 3.5 ns) [175] which, together with the high temperature stability of nanogratings, promotes the usage under harsh conditions. However, for applications e.g. in the field of high power lasers the losses of the wave plates (here 68 % for the half-wave and 50 % for the quarter-wave plate) might be critical. Although intrinsic scattering losses due to the porous grating structure can not be avoided completely, losses due to dangling bond type defects can be reduced by annealing the wave plates (see Section 3.3) while anti-reflection coatings may serve to lower Fresnel losses.

The generated beams can be used e.g. as vortex tweezers with tunable orbital angular momentum for controlling the torque transferred to the trapped particles [176]. In addition,

the concept of tailored birefringence can be used for even more sophisticated polarization distribution in the field of high-resolution microscopy.

5.2 Application for high-resolution microscopy

In order to image material or biological tissue conventional wide-field microscopy usually serves as method of choice. In this approach sample features within the focal plane as well as out-of-focus features are uniformly illuminated. This leads to basic restrictions in performance since the contribution of the non-focal planes disturb the image quality due to blurring effects and low signal-to-noise ratio.
Optical sectioning methods such as structured illumination microscopy (SIM), in contrast, aim to eliminate the out-of-focus contributions to exclusively provide focal plane information yielding a gain in resolution [177]. However, the need to (mechanically or electronically) move a transmission grating in order to acquire at least three images for different grating positions limits the acquisition speed.

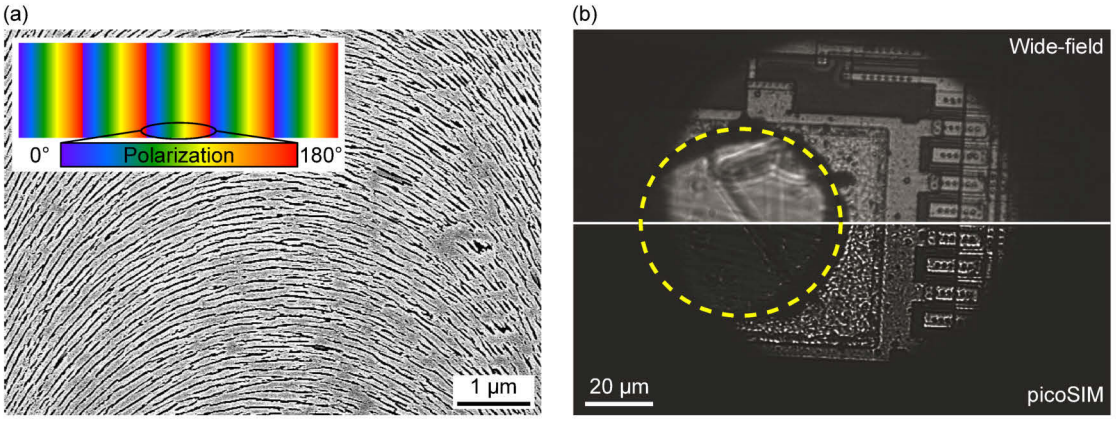

Fig. 5.3: (a) SEM image of a nanograting-based wave plate after polishing and etching and (inset) sketch of the (total) desired polarization distribution. (b) Wide-field and picoSIM image of a ceramic chip (separated by the white line). The dashed circle marks the out-of-focus region that is strongly suppressed in the case of picoSIM.

To overcome this drawback a homogeneous but polarization encoded structured illumination (polarized-illumination-coded SIM, short: picoSIM) allows for optical sectioning in a single exposure revealing high spatial and temporal resolution [19]. In this approach, a polarization coded illumination is generated by a (nanograting-based) wave plate. The wave plate basically acts as quarter-wave plate while the incident beam changes its polar-

ization state from circular to linear but with spatially dependent orientation of the linear polarization (see inset in Fig. 5.3 (a)). This is realized by setting the slow axis orientation of the nanogratings correspondingly. Laser inscription was done using a wavelength of 515 nm, a laser repetition rate of 1 MHz, a pulse energy of 170 nJ, a line separation of 0.2 µm and a speed of the sample movement of 1.7 $\frac{mm}{s}$. The change of the nanograting orientation was 0.5 degree per line. Figure 5.3 (a) shows a SEM image of an inscribed wave plate after polishing and etching. The smooth bending of the grating planes without the indication of individual scans confirms the continuous and coherent alignment corresponding to the previously imprinted structure.

This periodically modulated direction of the incident polarization pattern is imaged in the back-focal plane of the microscope objective. While the polarization pattern is only present in the focal plane its contrast vanishes in the out-of-focus region. Thus, only the polarization in the focal region is effectively modulated. Subsequently, the back reflected light is transmitted through a 3-way beam splitter followed by differently aligned analyzers generating 3 individual pictures. These pictures are used for reconstruction to generate an optically sectioned image with suppressed out-of-focus blur.

This concept was used to image a ceramic chip sample with height differences of about 6 µm (see Fig. 5.3 (b)). Compared to the wide-field image the reconstructed picoSIM image exhibits strongly reduced out-of-focus blur and improved lateral resolution. In addition, due to the single exposure within 1 ms fast mechanical or biological processes such as cellular movement could be investigated by this technique. Moreover, also incoherent light can be used for illumination extending the application range of picoSIM [178].

6 Conclusion and Outlook

The functionalization of glasses in order to make use of their outstanding optical, chemical and mechanical properties was revolutionized by the development of ultrashort pulse laser systems. In this framework manifold solutions e.g. in the field of laser bonding, deep hole drilling or laser cutting with extraordinary precision came up during recent years. One of the key aspects of ultrashort laser processing is the localized interaction within the bulk of transparent materials based on nonlinear absorption mechanisms [1, 2].

Fused silica with its simple composition and well-known characteristics served as material of choice to study the basic types of modifications induced by focused ultrashort laser pulses. Most intriguingly highly anisotropic structures with feature sizes far below the wavelength of light can be induced in an otherwise isotropic host material. These so-called nanogratings form during the cumulative action of several hundreds of laser pulses and always align perpendicular to the laser polarization [12, 15, 16]. Known for their tremendous form-birefringence the formation process of the imprinted sub-wavelength grating is still elusive in particular due to the short timescales, complex physical mechanisms involved as well as the buried absorption volume. In particular, it was not clear whether nanogratings consist of a merely continuous change of the material density or microscopic voids that arrange in periodic grating bars [53, 130]. Moreover, nanogratings were found in diverse glasses [152], crystals [153] and recently even in the bulk of semiconductors [155] indicating that a general mechanism dictates their formation.

Within the frame of this thesis, the primary characteristics of nanogratings, their stepwise formation sequence and their material composition dependence were investigated. The results presented give novel insights in the complex interaction process during the rapid ionization, defect formation, carrier relaxation and resulting material modification.

First, nanogratings in fused silica were studied. These require a certain laser pulse overlap while the pulse number per laser spot denotes the key parameter for the step-wise formation sequence. In contrast, basic laser pulse parameters such as the pulse duration, energy and focusing define the laser pulse intensity and so the formation threshold. The

nanostructure inscription is accompanied by bond breaking of the silica matrix and related bond-type defects (NBOHCs, E' centers) that mediate the feedback process reducing the ionization threshold from pulse to pulse [15, 95, 24]. As a result of the bond breaking molecular oxygen forms that is kept in microscopic pores. Moreover, the nanostructure is embedded in densified glass which is a result of the rapid heating and quenching leading to higher fictive temperature and increased material density. The lower relative volume corresponds to permanent strain which causes (as direct response) elastic strain within the laser-modified region as well as in the surrounding. As confirmed by wide-angle X-ray scattering the modified region exhibits tensile strain that scales with the laser repetition rate. When cleaving the sample the elastic strain relaxes in part resulting in a bimodal surface deformation that indicates a complex stress distribution due to the laser-induced nanostructure.

Combining small-angle X-ray scattering, FIB-SEM imaging and optical retardance measurements reveal that nanogratings consist of sheet-like cavities which form and assemble in regular grating bars during the action of multiple laser pulses. The formation of these pores, the increase in number and alignment could be imaged and systematically studied for the first time. This mechanism was found to occur within 4 distinct phases from stress-driven (phase 1 and 2) to polarization-driven (phase 3 and 4):

Focused single ultrashort laser pulses result in isotropic cylindrical voids which emerge entirely deterministic without the need for preexisting seeds (phase 1). Increasing pulse overlap leads to the deformation of these voids and the formation of randomly aligned inhomogeneities (phase 2). For ongoing irradiation these inhomogeneities nucleate the formation of anisotropic pores driven by field enhancement perpendicular to the laser polarization mediated by defect-assisted ionization from pulse to pulse (phase 3). When a multitude of anisotropic pores have formed these align exactly perpendicular to the polarization direction and their number strongly increases forming a more porous glass (phase 4). While in the first place the alignment of pores might be driven by a cavity-like amplification process as suggested in [15, 24] alternative effects such as the coherent superposition of the scattered field at nanoscopic pores could promote the formation of new grating planes and so dictate the continuous reduction of the period even below $\lambda/2n$ [96]. Thus, pronounced scattering due to a higher number of anisotropic pores (filling fraction of grating planes) facilitates smaller periods as observed for repeated rewriting of nanogratings.

The findings explain several aspects associated with nanogratings. First, nanogratings consist of hollow pores which link together forming regular grating planes. Thus, based on the large index contrast between the pores and the surrounding glass strong form-birefringence is induced despite the small feature size of the modification. Given that the grating is composed of hollow voids explains the highly anisotropic etch rate with respect to the polarization direction [26]. Moreover, the nanostructure formation is directly linked to the formation of voids induced by single ultrashort laser pulses. Thus, for glasses where void formation is hardly obtained (e.g. borosilicate [138]) also nanograting formation is hindered [61]. In addition, when scanning the laser focus through the glass less pulses are needed to form a regular nanograting due to the formation of cracks along the scanned path. These cracks promote the growth of anisotropic pores in particular when the polarization is perpendicular to the scanning direction resulting in pronounced retardance compared with all other polarization directions. Consequently, when using point-wise inscription the formation of nanogratings is strongly delayed due to the absence of seeds (cracks along the scanned path) which is proven by in-situ measurements of the optical diffraction. In addition, the process of period reduction due to influence of the scattered field resembles recent theoretical studies on the formation of laser-induced periodic surface structures (LIPSS) [151] which could explain the fine periods of LIPSS found in this work.

Nanogratings can be induced in the bulk of different glasses. The results reveal that nanogratings are no special feature of silica and are not linked to the anomalous glass density dependence on the fictive temperature. The formation sequence in doped silica glasses (ULE or germanium doped silica) as well as in Borofloat 33 occurs (as found before) via pore formation, subsequent increase in number of pores and alignment of those. Basic thermomechanical properties of the glass dictate its ability to decompose and thus define the formation threshold of nanogratings but also influence the microscopic features of the induced nanopores such as their thickness. A pronounced decomposition of the glass, e.g. due to a lower modification threshold can support the grating formation which is linked to the reduction of the period. In addition, the analysis of nanogratings in Borofloat 33 reveal that given a glass structure with a certain amount of inhomogeneities the average distance of nanopores may strongly change in agreement to recent theoretical studies [77]. For the first time a reduced periodicity of nanogratings down to 60 nm ($\approx \lambda/10n$) was found highlighting the ability for vast photonic applications based on tailoring the underlying grating characteristics and so the optical response.

Intriguingly, nanogratings can be rewritten, i.e. an existing nanograting is erased and newly arranged by inscribing again at the same position with differently oriented laser polarization which was comprehensively investigated here, too. The results show that the grating formation basically occurs in the same way for multiple rewrite steps. Repeated heating and quenching during the individual rewrite steps promotes the decomposition in a porous glass resulting in larger birefringence for high pulse overlap. Despite the grating quality may degrade during multiple rewrite steps it allows for various applications such as rewritable optical data storage with tremendous data densities [67].
Finally, it has been demonstrated that nanograting-based wave plates enable diverse applications for almost arbitrary polarization manipulation. On the one hand wave plates for the generation of radially or azimuthally polarized vortex beams can be realized that may serve as optical vortex tweezers with tunable orbital angular momentum [176]. On the other hand a polarization coded illumination was realized which provides structured illumination microscopy within one single exposure. Thus, the gain in acquisition speed enables the imaging of fast mechanical or biological processes which can even be extended for the usage of incoherent light. Due to the high temperature stability of nanogratings with stable retardance of up to 850°C the wave plates can be used under harsh conditions. Annealing at low temperatures can even be beneficial to reduce defect-assisted losses and increase the transmission of photonic functionalities.
Further investigations may address the pore formation itself or the continuous reduction of the period (due to e.g. splitting of grating planes [96]) by the help of time-resolved X-ray imaging during simultaneous laser-inscription. For the latter a pulse-to-pulse time resolution would be sufficient to image structural changes of a given nanograting volume.

Bibliography

[1] R. R. Gattass and E. Mazur. Femtosecond laser micromachining in transparent materials. *Nat. Photon.*, 2(4):219–225, 2008.

[2] K. Itoh, W. Watanabe, S. Nolte, and C. B. Schaffer. Ultrafast processes for bulk modification of transparent materials. *MRS Bull.*, 31:620–625, 2006.

[3] K. M. Davis, K. Miura, N. Sugimoto, and K. Hirao. Writing waveguides in glass with a femtosecond laser. *Opt. Lett.*, 21(21):1729–1731, 1996.

[4] A. Szameit and S. Nolte. Discrete optics in femtosecond-laser-written photonic structures. *J. Phys. B - At. Mol. Opt.*, 43(16):163001, 2010.

[5] S. Nolte, M. Will, J. Burghoff, and A. Tuennermann. Femtosecond waveguide writing: a new avenue to three-dimensional integrated optics. *Appl. Phys. A - Mater*, 77(1):109–111, 2003.

[6] G. D. Marshall, A. Politi, J. C. F. Matthews, P. Dekker, M. Ams, M. J. Withford, and J. L. O'Brien. Laser written waveguide photonic quantum circuits. *Opt. Express*, 17(15):12546–12554, 2009.

[7] E. N. Glezer and E. Mazur. Ultrafast-laser driven micro-explosions in transparent materials. *Appl.Phys. Lett.*, 71(7):882–884, 1997.

[8] S. Juodkazis, H. Misawa, T. Hashimoto, E. G. Gamaly, and B. Luther-Davies. Laser-induced microexplosion confined in a bulk of silica: Formation of nanovoids. *Appl. Phys. Lett.*, 88(20):201909–201909–3, 2006.

[9] E. G. Gamaly, S. Juodkazis, K. Nishimura, H. Misawa, B. Luther-Davies, L. Hallo, P. Nicolai, and V. T. Tikhonchuk. Laser-matter interaction in the bulk of a transparent solid: Confined microexplosion and void formation. *Phys. Rev. B*, 73(21):214101, 2006.

[10] K. Sugioka and Y. Cheng. Ultrafast lasers-reliable tools for advanced materials processing. *Light. Sci. Appl.*, 3:e149, 2014.

[11] P. G. Kazansky, H. Inouye, T. Mitsuyu, K. Miura, J. Qiu, K. Hirao, and F. Starrost. Anomalous anisotropic light scattering in ge-doped silica glass. *Phys. Rev. Lett.*, 82(10):2199–2202, 1999.

[12] Y. Shimotsuma, P. G. Kazansky, J. Qiu, and K. Hirao. Self-organized nanogratings in glass irradiated by ultrashort light pulses. *Phys. Rev. Lett.*, 91:247405, 2003.

[13] M. Birnbaum. Semiconductor surface damage produced by ruby lasers. *J. Appl. Phys.*, 36(11):3688–3689, 1965.

[14] L. Sudrie, M. Franco, B. Prade, and A. Mysyrowicz. Writing of permanent birefringent microlayers in bulk fused silica with femtosecond laser pulses. *Opt. Commun.*, 171:279 – 284, 1999.

[15] R. Taylor, C. Hnatovsky, and E. Simova. Applications of femtosecond laser induced self-organized planar nanocracks inside fused silica glass. *Laser Photon. Rev.*, 2(1-2):26–46, 2008.

[16] L. P. R. Ramirez, M. Heinrich, S. Richter, F. Dreisow, R. Keil, A. V. Korovin, U. Peschel, S. Nolte, and A. Tünnermann. Tuning the structural properties of femtosecond-laser-induced nanogratings. *Appl. Phys. A - Mater*, 100:1–6, 2010.

[17] M. Beresna, M. Gecevičius, and P. G. Kazansky. Polarization sensitive elements fabricated by femtosecond laser nanostructuring of glass. *Opt. Mater. Express*, 1(4):783–795, 2011.

[18] W. Cai, A. R. Libertun, and R. Piestun. Polarization selective computer-generated holograms realized in glass by femtosecond laser induced nanogratings. *Opt. Express*, 14(9):3785–3791, 2006.

[19] K. Wicker and R. Heintzmann. Single-shot optical sectioning using polarization-coded structured illumination. *J. Opt.*, 12(8):084010, 2010.

[20] R. S. Taylor, C. Hnatovsky, E. Simova, P. P. Rajeev, D. M. Rayner, and P. B. Corkum. Femtosecond laser erasing and rewriting of self-organized planar nanocracks in fused silica glass. *Opt. Lett.*, 32(19):2888–2890, 2007.

[21] B. Poumellec, M. Lancry, A. Chahid-Erraji, and P. G. Kazansky. Modification thresholds in femtosecond laser processing of pure silica: review of dependencies on laser parameters. *Opt. Mater. Express*, 1(4):766–782, 2011.

[22] Y. Shimotsuma, K. Hiroa, J. Qiu, and P. Kazansky. Nano-modification inside transparent materials by femtosecond laser single beam. *Mod. Phys. Lett. B*, 19(05):225–238, 2005.

[23] D. Wortmann, J. Gottmann, N. Brandt, and H. Horn-Solle. Micro- and nanostructures inside sapphire by fs-laser irradiation and selective etching. *Opt. Express*, 16(3):1517–1522, 2008.

[24] P. P. Rajeev, M. Gertsvolf, E. Simova, C. Hnatovsky, R. S. Taylor, V. R. Bhardwaj, D. M. Rayner, and P. B. Corkum. Memory in nonlinear ionization of transparent solids. *Phys. Rev. Lett.*, 97(25):253001, 2006.

[25] M. Beresna, M. Gecevicius, P. G. Kazansky, T. Taylor, and A. V. Kavokin. Exciton mediated self-organization in glass driven by ultrashort light pulses. *Appl. Phys. Lett.*, 101(5):053120, 2012.

[26] C. Hnatovsky, R. S. Taylor, E. Simova, V. R. Bhardwaj, D. M. Rayner, and P. B. Corkum. Polarization-selective etching in femtosecond laser-assisted microfluidic channel fabrication in fused silica. *Opt. Lett.*, 30(14):1867–1869, 2005.

[27] S. Ho, M. Haque, P. R. Herman, and J. S. Aitchison. Femtosecond laser-assisted etching of three-dimensional inverted-woodpile structures in fused silica. *Opt. Lett.*, 37(10):1682–1684, 2012.

[28] E. Bricchi, B. G. Klappauf, and P. G. Kazansky. Form birefringence and negative index change created by femtosecond direct writing in transparent materials. *Opt. Lett.*, 29(1):119–121, 2004.

[29] M. Lancry, F. Brisset, and B. Poumellec. In the heart of nanogratings made up during femtosecond laser irradiation. *Proc. of Bragg gratings, photosensitivity, and poling in glass waveguides (BGPP), Karlsruhe, Germany, paper BWC3*, 2010.

[30] J. E. Shelby. *Introduction to glass science and technology*. The royal society of chemistry, 2 edition, 2005.

[31] H. Scholze. *Glas*. Springer Berlin / Heidelberg, 1988.

[32] W. H. Zachariasen. The atomic arrangement in glass. *J. Am. Chem. Soc.*, 54:3841–3851, 1932.

[33] L. Skuja, M. Hirano, H. Hosono, and K. Kajihara. Defects in oxide glasses. *Phys. Stat. Solidi. C*, 2(1):15–24, 2005.

[34] R. Brückner. Das thermische ausdehnungsverhalten von kieselgals als funktion der thermischen vorgeschichte. *Naturwissenschaften*, 49:150–152, 1962.

[35] L. Bressel, D. de Ligny, C. Sonneville, V. Martinez, V. Mizeikis, R. Buividas, and S. Juodkazis. Femtosecond laser induced density changes in geo2 and sio2 glasses: fictive temperature effect [invited]. *Opt. Mater. Express*, 1(4):605–613, 2011.

[36] A. E. Geissberger and F. L. Galeener. Raman studies of vitreous sio_2 versus fictive temperature. *Phys. Rev. B*, 28(6):3266–3271, 1983.

[37] F. L. Galeener. Effects of modes of formation on the structure of glass raman and esr studies of the thermal history of amorphous sio2. *J. Non-Cryst. Solids*, 71(1):373–386, 1985.

[38] J. W. Chan, T. Huser, S. Risbud, and D. M. Krol. Structural changes in fused silica after exposure to focused femtosecond laser pulses. *Opt. Lett.*, 26(21):1726–1728, 2001.

[39] http://www.us.schott.com/tubing/english/download/schott-brochure-technical glasses_us.pdf, access on 16.02.2016.

[40] M. Lancry, J. Canning, K. Cook, M. Heili, D. R. Neuville, and B. Poumellec. Nanoscale femtosecond laser milling and control of nanoporosity in the normal and anomalous regimes of geo2-sio2 glasses. *Opt. Mater. Express*, 6(2):321–330, 2016.

[41] I. Mingareev. *Ultrafast dynamics of melting and ablation at large laser intensities*. PhD thesis, Technische Hochschule Aachen, 2009.

[42] S. K. Sundaram and E. Mazur. Inducing and probing non-thermal transitions in semiconductors using femtosecond laser pulses. *Nat. Mater.*, 1(4):217–224, 2002.

[43] C. B. Schaffer, A. Brodeur, and E. Mazur. Laser-induced breakdown and damage in bulk transparent materials induced by tightly focused femtosecond laser pulses. *Meas. Sci. Technol.*, 12(11):1784, 2001.

[44] S. C. Jones, P. Braunlich, R. T. Casper, X.-A. Shen, and P. Kelly. Recent progress on laser-induced modifications and intrinsic bulk damage of wide-gap optical materials. *Opt. Eng.*, 28(10):281039–281039, 1989.

[45] B. C. Stuart, M. D. Feit, S. Herman, A. M. Rubenchik, B. W. Shore, and M. D. Perry. Nanosecond-to-femtosecond laser-induced breakdown in dielectrics. *Phys. Rev. B*, 53(4):1749–1761, 1996.

[46] M. Lenzner, J. Krüger, S. Sartania, Z. Cheng, Ch. Spielmann, G. Mourou, W. Kautek, and F. Krausz. Femtosecond optical breakdown in dielectrics. *Phys. Rev. Lett.*, 80(18):4076–4079, 1998.

[47] L.V. Keldysh. Ionization in the field of a strong electromagnetic wave. *Zh. Eksperim. i Teor. Fiz.*, Vol: 47, 1964.

[48] M. Beresna, M. Gecevicius, and P. G. Kazansky. Ultrafast laser direct writing and nanostructuring in transparent materials. *Adv. Opt. Photon.*, 6(3):293–339, 2014.

[49] M. D. Perry, B. C. Stuart, P. S. Banks, M. D. Feit, V. Yanovsky, and A. M. Rubenchik. Ultrashort-pulse laser machining of dielectric materials. *J. Appl. Phys.*, 85(9):6803–6810, 1999.

[50] C. Corbari, A. Champion, M. Gecevičius, M. Beresna, Y. Bellouard, and P. G. Kazansky. Femtosecond versus picosecond laser machining of nano-gratings and micro-channels in silica glass. *Opt. Express*, 21(4):3946–3958, 2013.

[51] C. B. Schaffer, J. F. Garcia, and E. Mazur. Bulk heating of transparent materials using a high-repetition-rate femtosecond laser. *Appl. Phys. A - Mater*, 76(3):351–354, 2003.

[52] S. Eaton, H. Zhang, P. Herman, F. Yoshino, L. Shah, J. Bovatsek, and A. Arai. Heat accumulation effects in femtosecond laser-written waveguides with variable repetition rate. *Opt. Express*, 13(12):4708–4716, 2005.

[53] C. Hnatovsky, R. S. Taylor, P. P. Rajeev, E. Simova, V. R. Bhardwaj, D. M. Rayner, and P. B. Corkum. Pulse duration dependence of femtosecond-laser-fabricated nanogratings in fused silica. *Appl. Phys. Lett.*, 87(1):014104, 2005.

[54] A. Pasquarello and R. Car. Identification of raman defect lines as signatures of ring structures in vitreous silica. *Phys. Rev. Lett.*, 80(23):5145–5147, 1998.

[55] J. W. Chan, T. R. Huser, S. H. Risbud, and D. M. Krol. Modification of the fused silica glass network associated with waveguide fabrication using femtosecond laser pulses. *Appl. Phys. A - Mater*, 76(3):367–372, 2003.

[56] K. Miura, J. Qiu, H. Inouye, T. Mitsuyu, and K. Hirao. Photowritten optical waveguides in various glasses with ultrashort pulse laser. *Appl. Phys. Lett.*, 71(23):3329–3331, 1997.

[57] Y. Nasu, M. Kohtoku, and Y. Hibino. Low-loss waveguides written with a femtosecond laser for flexible interconnection in a planar light-wave circuit. *Opt. Lett.*, 30(7):723–725, 2005.

[58] M. Haque, K. K. C. Lee, S. Ho, L. A. Fernandes, and P. R. Herman. Chemical-assisted femtosecond laser writing of lab-in-fibers. *Lab Chip*, 14(19):3817–3829, 2014.

[59] E. N. Glezer, M. Milosavljevic, L. Huang, R. J. Finlay, T.-H. Her, J. P. Callan, and E. Mazur. Three-dimensional optical storage inside transparentmaterials. *Opt. Lett.*, 21(24):2023–2025, 1996.

[60] T. Hashimoto, S. Juodkazis, and H. Misawa. Void formation in glasses. *New J. Phys.*, 9(8):253, 2007.

[61] F. Zimmermann, A. Plech, S. Richter, S. Döring, A. Tünnermann, and S. Nolte. Structural evolution of nanopores and cracks as fundamental constituents of ultrashort pulse-induced nanogratings. *Appl. Phys. A - Mater*, 114(1):75–79, 2014.

[62] A. Champion, M. Beresna, P. Kazansky, and Y. Bellouard. Stress distribution around femtosecond laser affected zones: effect of nanogratings orientation. *Opt. Express*, 21(21):24942–24951, 2013.

[63] M. Born and E. Wolf. *Principles of Optics*. Pergamon Press, Oxford, 1984.

[64] E. Bricchi and P. G. Kazansky. Extraordinary stability of anisotropic femtosecond direct-written structures embedded in silica glass. *Appl. Phys. Lett.*, 88(11):111119, 2006.

[65] M. Lancry, R. Desmarchelier, K. Cook, B. Poumellec, and J. Canning. Compact birefringent waveplates photo-induced in silica by femtosecond laser. *Micromachines*, 5(4):825, 2014.

[66] M. Beresna, M. Gecevicius, P. G. Kazansky, and T. Gertus. Radially polarized optical vortex converter created by femtosecond laser nanostructuring of glass. *Appl. Phys. Lett.*, 98(20):201101, 2011.

[67] J. Zhang, M. Gecevicius, M. Beresna, and P. G. Kazansky. Seemingly unlimited lifetime data storage in nanostructured glass. *Phys. Rev. Lett.*, 112:033901, 2014.

[68] C. Hnatovsky, R. S. Taylor, E. Simova, P. P. Rajeev, D. M. Rayner, V. R. Bhardwaj, and P. B. Corkum. Fabrication of microchannels in glass using focused femtosecond laser radiation and selective chemical etching. *Appl. Phys. A - Mater*, 84:47–61, 2006.

[69] P. G. Kazansky and Y. Shimotsuma. Self-assembled sub-wavelength structures and form birefringence created by femtosecond laser writing in glass: properties and applications. *J. Ceram. Soc.*, 116(1358):1052–1062, 2008.

[70] N. M. Bulgakova, V. P. Zhukov, and Y. P. Meshcheryakov. Theoretical treatments of ultrashort pulse laser processing of transparent materials: toward understanding the volume nanograting formation and quill writing effect. *Appl. Phys. B - Lasers O.*, 113(3):437–449, 2013.

[71] R. Buschlinger, S. Nolte, and U. Peschel. Self-organized pattern formation in laser-induced multiphoton ionization. *Phys. Rev. B*, 89(18):184306, 2014.

[72] S. R. J. Brueck and D. J. Ehrlich. Stimulated surface-plasma-wave scattering and growth of a periodic structure in laser-photodeposited metal films. *Phys. Rev. Lett.*, 48(24):1678–1681, 1982.

[73] V. R. Bhardwaj, E. Simova, P. P. Rajeev, C. Hnatovsky, R. S. Taylor, D. M. Rayner, and P. B. Corkum. Optically produced arrays of planar nanostructures inside fused silica. *Phys. Rev. Lett.*, 96:057404, 2006.

[74] R. Buividas, M. Mikutis, and S. Juodkazis. Surface and bulk structuring of materials by ripples with long and short laser pulses: Recent advances. *Prog. Quant. Electron.*, 38(3):119–156, 2014.

[75] Y. Liao, J. Ni, L. Qiao, M. Huang, Y. Bellouard, K. Sugioka, and Y. Cheng. High-fidelity visualization of formation of volume nanogratings in porous glass by femtosecond laser irradiation. *Optica*, 2(4):329–334, 2015.

[76] F. Liang, J. Bouchard, S. Leang Chin, and R. Vallee. Defect-assisted local field rearrangement during nanograting formation with femtosecond pulses. *Appl. Phys. Lett.*, 107(6):061903, 2015.

[77] A. Rudenko, J.-P. Colombier, and T. E. Itina. From random inhomogeneities to periodic nanostructures induced in bulk silica by ultrashort laser. *Phys. Rev. B*, 93(7):075427, 2016.

[78] A. Guinier and G. Fournet. *Small-Angle Scattering of X-rays*. John Wiley & Sons, New York, 1955.

[79] M. Sztucki, T. Narayanan, and G. Beaucage. In situ study of aggregation of soot particles in an acetylene flame by small-angle x-ray scattering. *J. Appl. Phys.*, 101(11):114304, 2007.

[80] J. J. Thomson. *Conduction of electricity through Gases*. Cambridge University Press, UK, 1903.

[81] P. Debye. Zerstreuung von röntgenstrahlen. *Annalen der Physik*, 46:809, 1915.

[82] A. Plech, P. Leiderer, and J. Boneberg. Femtosecond laser near field ablation. *Laser Photon. Rev.*, 3(5):435–451, 2009.

[83] A. Plech, V. Kotaidis, A. Siems, and M. Sztucki. Kinetics of the x-ray induced gold nanoparticle synthesis. *Phys. Chem. Chem. Phys.*, 10:3888–3894, 2008.

[84] G. Beaucage. Approximations Leading to a Unified Exponential/Power-Law Approach to Small-Angle Scattering. *J. Appl. Crystallogr.*, 28(6):717–728, 1995.

[85] H. K. Kammler, G. Beaucage, D. J. Kohls, N. Agashe, and J. Ilavsky. Monitoring simultaneously the growth of nanoparticles and aggregates by in situ ultra-small-angle x-ray scattering. *J. Appl. Phys.*, 97(5):054309, 2005.

[86] O. Glatter and O. Kratky. *Small-angle X-ray Scattering*. Academic, London, 1982.

[87] A. Plech, V. Kotaidis, M. Lorenc, and M. Wulff. Thermal dynamics in laser excited metal nanoparticles. *Chem. Phys. Lett.*, 401:565–569, 2005.

[88] M. Cammarata, M. Lorenc, T. K. Kim, J. H. Lee, Q. Y. Kong, E. Pontecorvo, M. Lo Russo, G. Schiro, A. Cupane, M. Wulff, and H. Ihee. Impulsive solvent heating probed by picosecond x-ray diffraction. *J. Chem. Phys.*, 124(12):124504, 2006.

[89] R. Jenkins and R. L. Snyder. *Introduction to X-Ray Powder Diffractometry*. Wiley, New York, 1996.

[90] Y. Kikuchi, H. Sudo, and N. Kuzuu. Thermal expansion of vitreous silica: Correspondence between dilatation curve and phase transitions in crystalline silica. *J. Appl. Phys.*, 82(8):4121–4123, 1997.

[91] H. Malitson. Interspecimen comparison of the refractive index of fused silica. *J. Opt. Soc. Am.*, 55:1205–1208, 1965.

[92] M. Beresna, M. Gecevicius, M. Lancry, B. Poumellec, and P. G. Kazansky. Broadband anisotropy of femtosecond laser induced nanogratings in fused silica. *Appl. Phys. Lett.*, 103(13):131903, 2013.

[93] Y. P. Raizer. Breakdown and heating of gases under the influence of a laser beam. *Sov. Phys. Uspekhi*, 8(5):650, 1966.

[94] C.-H. Fan and J. P. Longtin. Modeling optical breakdown in dielectrics during ultrafast laser processing. *Appl. Opt.*, 40(18):3124–3131, 2001.

[95] M. Lancry, B. Poumellec, J. Canning, K. Cook, J.-C. Poulin, and F. Brisset. Ultrafast nanoporous silica formation driven by femtosecond laser irradiation. *Laser Photon. Rev.*, 7(6):953–962, 2013.

[96] Y. Liao, W. Pan, Y. Cui, L. Qiao, Y. Bellouard, K. Sugioka, and Y. Cheng. Formation of in-volume nanogratings with sub-100-nm periods in glass by femtosecond laser irradiation. *Opt. Lett.*, 40(15):3623–3626, 2015.

[97] F. Zimmermann, S. Richter, S. Döring, A. Tünnermann, and S. Nolte. Ultrastable bonding of glass with femtosecond laser bursts. *Appl. Opt.*, 52(6):1149–1154, 2013.

[98] S. Richter, M. Heinrich, S. Döring, A. Tünnermann, and S. Nolte. Formation of femtosecond laser-induced nanogratings at high repetition rates. *Appl. Phys. A - Mater*, 104:503–507, 2011.

[99] S. Richter, F. Jia, M. Heinrich, S. Döring, U. Peschel, A. Tünnermann, and S. Nolte. The role of self-trapped excitons and defects in the formation of nanogratings in fused silica. *Opt. Lett.*, 37(4):482–484, 2012.

[100] G. Petite, P. Daguzan, S. Guizard, and P. Martin. Conduction electrons in wide-bandgap oxides: a subpicosecond time-resolved optical study. *Nucl. Instrum. Meth. B*, 107:97–101, 1996.

[101] J. H. Stathis and M. A. Kastner. Time-resolved photoluminescence in amorphous silicon dioxide. *Phys. Rev. B*, 35(6):2972–2979, 1987.

[102] M. Beresna, R. Drevinskas, A. S. Lipatiev, S. S. Fedotov, S. V. Lotarev, V. N. Sigaev, and P. G. Kazansky. Functional birefringent elements imprinted by femtosecond laser nanostructuring of multi-component glass. In *The European Conference on Lasers and Electro-Optics*, 2015.

[103] L. Sudrie, A. Couairon, M. Franco, B. Lamouroux, B. Prade, S. Tzortzakis, and A. Mysyrowicz. Femtosecond laser-induced damage and filamentary propagation in fused silica. *Phys. Rev. Lett.*, 89(18):186601, 2002.

[104] D. M. Rayner, A. Naumov, and P. B. Corkum. Ultrashort pulse non-linear optical absorption in transparent media. *Opt. Express*, 13(9):3208–3217, 2005.

[105] C. Mauclair, M. Zamfirescu, J. P. Colombier, G. Cheng, K. Mishchik, E. Audouard, and R. Stoian. Control of ultrafast laser-induced bulk nanogratings in fused silica via pulse time envelopes. *Opt. Express*, 20(12):12997–13005, 2012.

[106] S. S. Mao, F. Quere, S. Guizard, X. Mao, R. E. Russo, G. Petite, and P. Martin. Dynamics of femtosecond laser interactions with dielectrics. *Appl. Phys. A - Mater*, 79(7):1695–1709, 2004.

[107] P. Martin, S. Guizard, P. Daguzan, G. Petite, P. D'Oliveira, P. Meynadier, and M. Perdrix. Subpicosecond study of carrier trapping dynamics in wide-band-gap crystals. *Phys. Rev. B*, 55(9):5799–5810, 1997.

[108] S. Guizard, P. Martin, G. Petite, P. D'Oliveira, and P. Meynadier. Time-resolved study of laser-induced colour centres in sio_2. *J. Phys.-Condens. Mat.*, 8(9):1281, 1996.

[109] H.-B. Sun, S. Juodkazis, M. Watanabe, S. Matsuo, H. Misawa, and J. Nishii. Generation and recombination of defects in vitreous silica induced by irradiation with a near-infrared femtosecond laser. *J. Phys. Chem. B*, 104(15):3450–3455, 2000.

[110] A. Zoubir, C. Rivero, R. Grodsky, K. Richardson, M. Richardson, T. Cardinal, and M. Couzi. Laser-induced defects in fused silica by femtosecond ir irradiation. *Phys. Rev. B*, 73(22):224117, 2006.

[111] M. Lancry, B. Poumellec, R. Desmarchelier, and B. Bourguignon. Oriented creation of anisotropic defects by ir femtosecond laser scanning in silica. *Opt. Mater. Express*, 2(12):1809–1821, 2012.

[112] L. Skuja. Optically active oxygen-deficiency-related centers in amorphous silicon dioxide. *J. Non-Cryst. Solids*, 239:16–48, 1998.

[113] M. Watanabe, S. Juodkazis, H.-B. Sun, S. Matsuo, and H. Misawa. Luminescence and defect formation by visible and near-infrared irradiation of vitreous silica. *Phys. Rev. B*, 60(14):9959–9964, 1999.

[114] A. Morana, S. Girard, M. Cannas, E. Marin, C. Marcandella, P. Paillet, J. Perisse, J.-R. Mace, R. Boscaino, B. Nacir, A. Boukenter, and Y. Ouerdane. Influence of neutron and gamma-ray irradiations on rad-hard optical fiber. *Opt. Mater. Express*, 5(4):898–911, 2015.

[115] T. A. Laurence, J. D. Bude, N. Shen, T. Feldman, P. E. Miller, W. A. Steele, and T. Suratwala. Metallic-like photoluminescence and absorption in fused silica surface flaws. *Appl. Phys. Lett.*, 94(15):151114, 2009.

[116] F. Messina and M. Cannas. Stability of e centers induced by 4.7 ev laser radiation in sio2. *J. Non-Cryst. Solids*, 353:522–525, 2007.

[117] https://www.heraeus.com/en/hqs/fused_silica_quartz_knowledge_base/properties/properties.aspx, access on 29.04.2016.

[118] S. Richter, F. Zimmermann, A. Tünnermann, and S. Nolte. Laser welding of glasses at high repetition rates fundamentals and prospects. *Opt. Laser Technol.*, 83:59–66, 2016.

[119] B. Poumellec, L. Sudrie, M. Franco, B. Prade, and A. Mysyrowicz. Femtosecond laser irradiation stress induced in pure silica. *Opt. Express*, 11(9):1070–1079, 2003.

[120] P. Colomban, A. Tournie, and L. Bellot-Gurlet. Raman identification of glassy silicates used in ceramics, glass and jewellery: a tentative differentiation guide. *J. Raman Spectrosc.*, 37(8):841–852, 2006.

[121] D. J. Little, M. Ams, P. Dekker, G. D. Marshall, J. M. Dawes, and M. J. Withford. Femtosecond laser modification of fused silica: the effect of writing polarization on si-o ring structure. *Opt. Express*, 16(24):20029–20037, 2008.

[122] S. K. Sharma, J. F. Mammone, and M. F. Nicol. Raman investigation of ring configurations in vitreous silica. *Nature*, 292(5819):140–141, 1981.

[123] F. L. Galeener. Planar rings in glasses. *Solid State Commun.*, 44:1037–1040, 1982.

[124] L. Skuja and B. Güttler. Detection of interstitial oxygen molecules in sio_2 glass by a direct photoexcitation of the infrared luminescence of singlet o_2. *Phys. Rev. Lett.*, 77(10):2093–2096, 1996.

[125] A. J. Berger, Y. Wang, D. M. Sammeth, I. Itzkan, K. Kneipp, and M. S. Feld. Aqueous dissolved gas measurements using near-infrared raman spectroscopy. *Appl. Spectrosc.*, 49(8):1164–1169, 1995.

[126] S.-R. Ryu and M. Tomozawa. Structural relaxation time of bulk and fiber silica glass as a function of fictive temperature and holding temperature. *J. Am. Ceram. Soc.*, 89:81–88, 2006.

[127] C. Fan, B. Poumellec, R. Desmarchelier, H. Zeng, B. Bourguignon, G. Chen, and M. Lancry. Asymmetric orientational writing dependence on polarization and direction in li2o-nb2o5-sio2 glass with femtosecond laser irradiation. *Appl. Phys. B - Lasers O.*, 117(2):737–747, 2014.

[128] F. Zimmermann, A. Plech, S. Richter, A. Tünnermann, and S. Nolte. The onset of ultrashort pulse-induced nanogratings. *Laser Photon. Rev.*, 10:327–334, 2016.

[129] E. Rebollar, D. R. Rueda, I. Martin-Fabiani, A. Rodriguez-Rodriguez, M.-C. Garcia-Gutierrez, G. Portale, M. Castillejo, and T. A. Ezquerra. In situ monitoring of laser-induced periodic surface structures formation on polymer films by grazing incidence small-angle x-ray scattering. *Langmuir*, 31(13):3973–3981, 2015.

[130] M. Lancry, K. Cook, J. Canning, and B. Poumellec. Nanogratings and molecular oxygen formation during femtosecond laser irradiation in silica. *Proc. of the conference on Lasers and Electro-Optics/Pacific Rim*, page paper C229, 2011.

[131] A. G. Kikhney and D. I. Svergun. A practical guide to small angle x-ray scattering (saxs) of flexible and intrinsically disordered proteins. *FEBS Letters*, 589(19, Part A):2570–2577, 2015.

[132] J. Ilavsky and P. R. Jemian. Irena: tool suite for modeling and analysis of small-angle scattering. *J. Appl. Crystallogr.*, 42(2):347–353, 2009.

[133] F. Zimmermann, A. Plech, S. Richter, A. Tünnermann, and S. Nolte. Ultrashort laser pulse induced nanogratings in borosilicate glass. *Appl. Phys. Lett.*, 104(21):211107, 2014.

[134] P. P. Rajeev, M. Gertsvolf, C. Hnatovsky, E. Simova, R. S. Taylor, P. B. Corkum, D. M. Rayner, and V. R. Bhardwaj. Transient nanoplasmonics inside dielectrics. *J. Phys. B-At. Mol. Opt.*, 40(11):273, 2007.

[135] S. P. Sharma, V. Oliveira, P. Herrero, and R. Vilar. Internal structure of the nanogratings generated inside bulk fused silica by ultrafast laser direct writing. *J. Appl. Phys.*, 116(5):053106, 2014.

[136] M. Lancry, F. Zimmerman, R. Desmarchelier, J. Tian, F. Brisset, S. Nolte, and B. Poumellec. Nanogratings formation in multicomponent silicate glasses. *Appl. Phys. B - Lasers O.*, 122(3):1–8, 2016.

[137] T. Tamaki, W. Watanabe, H. Nagai, M. Yoshida, J. Nishii, and K. Itoh. Structural modification in fused silica by a femtosecond fiber laser at 1558 nm. *Opt. Express*, 14(15):6971–6980, 2006.

[138] S. Richter, S. Döring, F. Burmeister, F. Zimmermann, A. Tünnermann, and S. Nolte. Formation of periodic disruptions induced by heat accumulation of femtosecond laser pulses. *Opt. Express*, 21(13):15452–15463, 2013.

[139] T. Q. Jia, F. L. Zhao, M. Huang, H. X. Chen, J. R. Qiu, R. X. Li, Z. Z. Xu, and H. Kuroda. Alignment of nanoparticles formed on the surface of 6h-sic crystals irradiated by two collinear femtosecond laser beams. *Appl. Phys. Lett.*, 88(11):111117, 2006.

[140] Q. Wu, Y. Ma, R. Fang, Y. Liao, Q. Yu, X. Chen, and K. Wang. Femtosecond laser-induced periodic surface structure on diamond film. *Appl. Phys. Lett.*, 82(11):1703–1705, 2003.

[141] L. Jiang, X. Shi, X. Li, Y. Yuan, C. Wang, and Y. Lu. Subwavelength ripples adjustment based on electron dynamics control by using shaped ultrafast laser pulse trains. *Opt. Express*, 20(19):21505–21511, 2012.

[142] S. Höhm, A. Rosenfeld, J. Krüger, and J. Bonse. Femtosecond laser-induced periodic surface structures on silica. *J. Appl. Phys.*, 112(1):014901, 2012.

[143] F. Liang, R. Vallée, and S. L. Chin. Physical evolution of nanograting inscription on the surface of fused silica. *Opt. Mater. Express*, 2(7):900–906, 2012.

[144] R. Wagner, J. Gottmann, A. Horn, and E. W. Kreutz. Subwavelength ripple formation induced by tightly focused femtosecond laser radiation. *Appl. Surf. Sci.*, 252(24):8576–8579, 2006.

[145] F. Liang, R. Vallee, D. Gingras, and S. L. Chin. Role of ablation and incubation processes on surface nanograting formation. *Opt. Mater. Express*, 1(7):1244–1250, 2011.

[146] S. Richter, A. Plech, M. Steinert, M. Heinrich, S. Döring, F. Zimmermann, U. Peschel, E.Bernhard Kley, A. Tünnermann, and S. Nolte. On the fundamental structure of femtosecond laser-induced nanogratings. *Laser Photon. Rev.*, 6(6):787–792, 2012.

[147] L. Sudrie, M. Franco, B. Prade, and A. Mysyrowicz. Study of damage in fused silica induced by ultra-short ir laser pulses. *Opt. Commun.*, 191:333–339, 2001.

[148] A.-C. Tien, S. Backus, H. Kapteyn, M. Murnane, and G. Mourou. Short-pulse laser damage in transparent materials as a function of pulse duration. *Phys. Rev. Lett.*, 82(19):3883–3886, 1999.

[149] R. Buividas, L. Rosa, R. Sliupas, T. Kudrius, G. Slekys, V. Datsyuk, and S. Juodkazis. Mechanism of fine ripple formation on surfaces of (semi)transparent materials via a half-wavelength cavity feedback. *Nanotechnology*, 22(5fa):055304, 2011.

[150] Z. Fang, Y. Zhao, and J. Shao. Femtosecond laser-induced periodic surface structure on fused silica surface. *Optik*, 127(3):1171–1175, 2016.

[151] H. Zhang, J.-P. Colombier, C. Li, N. Faure, G. Cheng, and R. Stoian. Coherence in ultrafast laser-induced periodic surface structures. *Phys. Rev. B*, 92(17):174109, 2015.

[152] M. Lancry, B. Poumellec, A. Chahid-Erraji, M. Beresna, and P. G. Kazansky. Dependence of the femtosecond laser refractive index change thresholds on the chemical composition of doped-silica glasses. *Opt. Mater. Express*, 1(4):711–723, 2011.

[153] J. Gottmann, D. Wortmann, and M. Hörstmann-Jungemann. Fabrication of subwavelength surface ripples and in-volume nanostructures by fs-laser induced selective etching. *Appl. Surf. Sci.*, 255(10):5641 – 5646, 2009.

[154] M. Mori, Y. Shimotsuma, T. Sei, M. Sakakura, K. Miura, and H. Udono. Tailoring thermoelectric properties of nanostructured crystal silicon fabricated by infrared femtosecond laser direct writing. *Phys. Status Solidi A*, 212(4):715–721, 2015.

[155] Y. Shimotsuma, T. Sei, M. Sakakura, K. Miura, and H. Udono. Nanostructuring in indirect band-gap semiconductor using ir femtosecond double pulses. *J. Laser Micro. Nanoen.*, 11:35–40, 2016.

[156] S. Richter, C. Miese, S. Döring, F. Zimmermann, M. J. Withford, A. Tünnermann, and S. Nolte. Laser induced nanogratings beyond fused silica - periodic nanostructures in borosilicate glasses and ule;. *Opt. Mater. Express*, 3(8):1161–1166, 2013.

[157] S. Richter, F. Zimmermann, S. Döring, A. Tünnermann, and S. Nolte. Ultrashort high repetition rate exposure of dielectric materials: laser bonding of glasses analyzed by micro-raman spectroscopy. *Appl. Phys. A - Mater*, 110(1):9–15, 2013.

[158] https://www.corning.com/media/worldwide/csm/documents/ULE 7973 low expansion glass product information brochure.pdf, access on 16.02.2016.

[159] S. Spinner and R. M. Waxler. Relation between refractive index and density of glasses resulting from annealing compared with corresponding relation resulting from compression. *Appl. Opt.*, 5(12):1887–1889, 1966.

[160] Y. Hayasaki, M. Isaka, A. Takita, and S. Juodkazis. Time-resolved interferometry of femtosecond-laser-induced processes under tight focusing and close-to-optical breakdown inside borosilicate glass. *Opt. Express*, 19(7):5725–5734, 2011.

[161] D. Gerlich, M. Wolf, I. Yaacov, and B. Nissenson. Thermoelastic properties of ule titanium silicate glass. *J. Non-Cryst. Solids*, 21(2):243–249, 1976.

[162] S. Richter, D. Möncke, F. Zimmermann, E. I. Kamitsos, L. Wondraczek, A. Tünnermann, and S. Nolte. Ultrashort pulse induced modifications in ule - from nanograting formation to laser darkening. *Opt. Mater. Express*, 5(8):1834–1850, 2015.

[163] M. Lancry, N. Guth, F. Zimmermann, F. Brisset, S. Nolte, and B. Poumellec. Porous nanogratings and related form birefringence in silicate and germanate glasses. *Proc. of Bragg gratings, photosensitivity, and poling in glass waveguides (BGPP), Barcelona, Spain*, 2014.

[164] T. Asai, Y. Shimotsuma, T. Kurita, A. Murata, S. Kubota, M. Sakakura, K. Miura, F. Brisset, B. Poumellec, and M. Lancry. Systematic control of structural changes in geo2 glass induced by femtosecond laser direct writing. *J. Am. Ceram. Soc.*, 98(5):1471–1477, 2015.

[165] L. N. Skuja. Photoluminescence of intrinsic defects in glassy geo2. *Phys. Status Solidi A*, 114:731–737, 1989.

[166] R. Desmarchelier, M. Lancry, M. Gecevicius, M. Beresna, P. G. Kazansky, and B. Poumellec. Achromatic polarization rotator imprinted by ultrafast laser nanostructuring in glass. *Appl. Phys. Lett.*, 107(18):181111, 2015.

[167] Y. Hiraoka, J. R. Swedlow, M. R. Paddy, D. A. Agard, and J. W. Sedat. Three-dimensional multiple-wavelength fluorescence microscopy for the structural analysis of biological phenomena. *Semin. Cell Biol.*, 2(3):153–165, 1991.

[168] Z. Bomzon, V. Kleiner, and E. Hasman. Formation of radially and azimuthally polarized light using space-variant subwavelength metal stripe gratings. *Appl. Phys. Lett.*, 79(11):1587 –1589, 2001.

[169] Q. Zhan. Cylindrical vector beams: from mathematical concepts to applications. *Adv. Opt. Photon.*, 1(1):1–57, 2009.

[170] R. Dorn, S. Quabis, and G. Leuchs. Sharper focus for a radially polarized light beam. *Phys. Rev. Lett.*, 91(23):233901, 2003.

[171] T. Ehmke, T. H. Nitzsche, A. Knebl, and A. Heisterkamp. Molecular orientation sensitive second harmonic microscopy by radially and azimuthally polarized light. *Biomed. Opt. Express*, 5(7):2231–2246, 2014.

[172] H. Wang, L. Shi, B. Lukyanchuk, C. Sheppard, and C. T. Chong. Creation of a needle of longitudinally polarized light in vacuum using binary optics. *Nat. Photon.*, 2(8):501–505, 2008.

[173] C. Hnatovsky, V. Shvedov, W. Krolikowski, and A. Rode. Revealing local field structure of focused ultrashort pulses. *Phys. Rev. Lett.*, 106:123901, 2011.

[174] R. Drevinskas, M. Gecevicius, M. Beresna, and P. G. Kazansky. Femtosecond laser nanostructuring for high-topological charge vortex tweezers with continuously tunable orbital angular momentum. In *The European Conference on Lasers and Electro-Optics*, 2015. ECBO_2_3.

[175] http://www.altechna.com/download/wop/Operation Manual-_130701.pdf, access on 12.08.2016.

[176] M. Gecevicius, R. Drevinskas, M. Beresna, and P. G. Kazansky. Single beam optical vortex tweezers with tunable orbital angular momentum. *Appl. Phys. Lett.*, 104(23):231110, 2014.

[177] M. A. A. Neil, R. Juskaitis, and T. Wilson. Method of obtaining optical sectioning by using structured light in a conventional microscope. *Opt. Lett.*, 22(24):1905–1907, 1997.

[178] F. Zimmermann, S. Richter, R. Buschlinger, S. Shukla, R. Heintzmann, U. Peschel, and S. Nolte. Ultrashort pulse-induced periodic nanostructures in bulk glass: from fundamentals to applications in high-resolution microscopy. In *Optically Induced Nanostructures: Biomedical and Technical Applications*. De Gruyter, Berlin, 2015.

[179] F. Zimmermann, A. Plech, S. Richter, A. Tünnermann, and S. Nolte. On the rewriting of ultrashort pulse-induced nanogratings. *Opt. Lett.*, 40(9):2049–2052, 2015.

[180] F. Zimmermann, M. Lancry, A. Plech, S. Richter, T. Ullsperger, B. Poumellec, A. Tünnermann, and S. Nolte. Ultrashort pulse laser processing of silica at high repetition rates - from network change to residual strain. *Int. J. Appl. Glass Sci.*, pages 1–8, 2016.

[181] F. Zimmermann, M. Lancry, A. Plech, S. Richter, B. Hari Babu, B. Poumellec, A. Tünnermann, and S. Nolte. Femtosecond laser written nanostructures in ge-doped glasses. *Opt. Lett.*, 41(6):1161–1164, 2016.

Publication in Peer-reviewed Journals

(P1) S. Döring, J. Szilagyi, S. Richter, F. Zimmermann, M. Richardson, A. Tünnermann and S. Nolte. Evolution of hole shape and size during short and ultrashort pulse laser deep drilling. *Opt. Express* 20: 27147-27154, 2012.

(P2) S. Richter, A. Plech, M. Steinert, M. Heinrich, S. Döring, F. Zimmermann, U. Peschel, E. Bernhard Kley, A. Tünnermann, and S. Nolte. On the fundamental structure of femtosecond laser-induced nanogratings. *Laser Photon. Rev.* 6: 787-792, 2012.

(P3) S. Richter, S. Döring, F. Burmeister, F. Zimmermann, A. Tünnermann and S. Nolte. Formation of periodic disruptions induced by heat accumulation of femtosecond laser pulses. *Opt. Express* 21: 15452, 2013.

(P4) S. Richter, C. Miese, S. Döring, F. Zimmermann, M. J. Withford, A. Tünnermann, and S. Nolte. Laser induced nanogratings beyond fused silica - periodic nanostructures in borosilicate glasses and ULE. *Opt. Mater. Express* 3: 1161, 2013.

(P5) S. Richter, F. Zimmermann, S. Döring, A. Tünnermann and S. Nolte. Ultrashort high repetition rate exposure of dielectric materials: laser bonding of glasses by micro-Raman spectroscopy. *Appl. Phys. A - Mater* 110: 9-15, 2013.

(P6) F. Zimmermann, S. Richter, S. Döring, A. Tünnermann, and S. Nolte. Ultrastable bonding of glass with bursts of femtosecond laser pulses. *Appl. Opt.* 52: 1149-1154, 2013.

(P7) F. Zimmermann, A. Plech, S. Richter, A. Tünnermann, and S. Nolte. Ultrashort laser pulse induced nanogratings in Borosilicate glass. *Appl. Phys. Lett.* 104: 211107, 2014.

(P8) F. Zimmermann, A. Plech, S. Richter, S. Döring, A. Tünnermann, and S. Nolte. Structural evolution of nanopores and cracks as fundamental constituents of ultrashort pulse-induced nanogratings. *Appl. Phys. A - Mater* 114: 75-79 (invited), 2014.

(P9) S. Richter, D. Möncke, F. Zimmermann, E.I. Kamitsos, L. Wondraczek, A. Tünnermann and S. Nolte. Ultrashort pulse induced modifications in ULE - from nanograting formation to laser darkening. *Opt. Mater. Express* 5: 1834-1850, 2015.

(P10) F. Zimmermann, A. Plech, S. Richter, A. Tünnermann, and S. Nolte. On the rewriting of ultrashort pulse induced nanogratings. *Opt. Lett.* 40: 2049-2052, 2015.

(P11) S. Richter, F. Zimmermann, R. Eberhardt, A. Tünnermann and S. Nolte. Towards laser welding of glasses without optical contacting. *Appl. Phys. A - Mater* 121: 1-9, 2015.

(P12) D. Guzman-Silva, R. Brüning, F. Zimmermann, C. Vetter, M. Gräfe, M. Heinrich, S. Nolte, M. Duparre, A. Agiello, M. Ornigotti, A. Szameit. Demonstration of local teleportation using classical entanglement. *Laser Photon. Rev.* 10: 317-321, 2016.

(P13) S. Richter, F. Zimmermann, A. Tünnermann, and S. Nolte. Laser welding of glasses at high repetition rates - fundamentals and prospects. *Opt. Laser Technol.* 83: 59-66, 2016.

(P14) M. Lancry, F. Zimmermann, R. Desmarchelier, F. Brisset, S. Nolte and B. Poumellec. Nanogratings formation in multicomponent silicate glasses. *Appl. Phys. B - Lasers O.* 122: 1-8, 2016.

(P15) F. Zimmermann, M. Lancry, A. Plech, S. Richter, B. H. Babu, B. Poumellec, A. Tünnermann, and S. Nolte. Femtosecond laser written nanostructures in Ge-doped glasses. *Opt. Lett.* 41: 1161-1164, 2016.

(P16) F. Zimmermann, A. Plech, S. Richter, A. Tünnermann, and S. Nolte. The onset of ultrashort pulse induced nanogratings. *Laser Photon. Rev.* 10: 327-334, 2016.

(P17) F. Zimmermann, M. Lancry, A. Plech, S. Richter, T. Ullsperger, B. Poumellec, A. Tünnermann, and S. Nolte. Ultrashort pulse laser processing of silica at high repetition rates - from network change to residual strain. *Int. J. Appl. Glass Sci.*, DOI: 10.1111/ijag.12221, 2016.

(P18) S. Richter, F. Zimmermann, A. Tünnermann, and S. Nolte. Fracture toughness of ultrashort pulse bonded fused silica. *Appl. Phys. A - Mater* 122: 1-6, 2016.

Book chapter

(P19) S. Richter, M. Heinrich, F. Zimmermann, C. Vetter, A. Tünnermann, and S. Nolte: Nanogratings in Fused Silica: Structure, Formation and Applications. Book chapter in R. Grunwald - *Linear and Nonlinear Nanooptics*, Springer, Berlin, 2015.

(P20) F. Zimmermann, S. Richter, R. Buschlinger, S. Shukla, R. Heintzmann, U. Peschel and S. Nolte: Ultrashort pulse-induced periodic nanostructures in bulk glass - from fundamentals to applications in high-resolution microscopy. Book chapter in K. König and A. Ostendorf - *Optically Induced Nanostructures: Biomedical and Technical Applications*, De Gruyter, Berlin, 2015.

Conference Contributions

(C1) S. Richter, S. Döring, F. Zimmermann, L. Lescieux, R. Eberhardt, S. Nolte, and A. Tünnermann. Welding of glass with femtosecond laser pulses at high repetition rates. DokDok, Naumburg, Germany, 2011.

(C2) F. Zimmermann, S. Richter, A. Plech, and S. Nolte. Ultrashort pulse induced nanogratings and their fundamental structure. DokDok, Oppurg, Germany, 2012.

(C3) S. Richter, S. Döring, F. Zimmermann, S. Nolte, and A. Tünnermann. Welding of transparent materials with ultrashort laser pulses. Proc. SPIE 8244-1 (invited paper), Photonics West - Laser-based Micro - and Nanopackaging and Assembly VI, San Francisco, USA, 2012.

(C4) C. Vetter, F. Zimmermann, S. Richter, M. Heinrich and S. Nolte. Femtosecond laser-induced nanogratings. DokDok, Oppurg, Germany, 2012.

(C5) S. Richter, F. Zimmermann, S. Döring, A. Tünnermann and S. Nolte. Ultrastable Bonding of glass with femtosecond laser bursts. Proc. SPIE 8611-47, Photonics West - Frontiers in Ultrafast Optics: Biomedical, Scientific, and Industrial Applications XIII, San Francisco, USA, 2013.

(C6) S. Nolte, F. Zimmermann, S. Richter, A. Plech, U. Peschel, A. Tünnermann. Ultrashort pulse induced nanogratings. MATEC Web of Conferences 8, 03001, Cargese, France, 2013.

(C7) F. Zimmermann, A. Plech, S. Richter and S. Nolte. On the evolution of primary constituents of ultrashort pulse-induced nanogratings. DokDok, Suhl, Germany, 2013.

(C8) F. Zimmermann, S. Richter, A. Plech, M. Steinert, M. Heinrich, S. Döring, U. Peschel, E. B. Kley, A. Tünnermann, and S. Nolte. The underlying structure of ultrashort pulse-induced nanogratings. Proc. SPIE 8611, Photonics West - Frontiers in Ultrafast Optics: Biomedical, Scientific, and Industrial Applications XIII, San Francisco, USA, 2013.

(C9) F. Dreisow, S. Richter, F. Zimmermann, R. Keil, M. Heinrich, R. Heilmann, A. Szameit, S. Nolte. Ultrafast laser processing of transparent materials. EuroMat, Sevilla, Spain, 2013.

(C10) F. Zimmermann, A. Plech, S. Richter, S. Döring, A. Tünnermann and S. Nolte. Morphological evolution of nanopores and cracks as fundamental components of ultrashort pulse laser-induced nanogratings. Proc. SPIE. 8972, Photonics West - Frontiers in Ultrafast Optics: Biomedical, Scientific, and Industrial Applications XIV, San Francisco, USA, 2014.

(C11) M. Lancry, N. Guth, R. Desmarchelier, F. Zimmerman, F. Brisset, S. Nolte and B. Poumellec. Porous nanogratings existence and related form birefringence in glasses. Proceedings of Bragg gratings, photosensitivity, and poling in glass waveguides (BGPP), Barcelona, Spain, 2014.

(C12) F. Zimmermann, A. Plech, S. Richter, A. Tünnermann and S. Nolte. Formation and evolution of ultrashort pulse-induced nanogratings in Borofloat glass. Proc. SPIE 9126, Photonics Europe - Nanophotonics V, Brussels, Belgium, 2014.

(C13) F. Zimmermann, A. Plech, S. Richter, A. Tünnermann and S. Nolte. Erasure and formation of femtosecond laser-induced nanostructures. Proc. SPIE. 9355-39, Photonics West - Frontiers in Ultrafast Optics: Biomedical, Scientific, and Industrial Applications XV, San Francisco, USA, 2015.

(C14) S. Richter, F. Zimmermann, A. Tünnermann, and S. Nolte. Realization of birefringent nanogratings in various glasses. Progress in electromagnetic research symposium (PIERS), Prague, Czech Republic, 2015.

(C15) S. Richter, F. Hashimoto, F. Zimmermann, Y. Ozeki, K. Itoh, A. Tünnermann and S. Nolte. Spatial and temporal temperature distribution of ultrashort pulse induced heat accumulation in glass. Proc. SPIE. 9355-42, Photonics West - Frontiers in Ultrafast Optics: Biomedical, Scientific, and Industrial Applications XV, San Francisco, USA, 2015.

(C16) A. Plech, F. Zimmermann, S. Richter, M. Liebi, M. Guizar-Sicairos, S. Doyle, A. Tünnermann, and S. Nolte. Structure formation in the bulk of laser-irradiated glasses. Small-angle scattering conference, Berlin, Germany, 2015.

(C17) S. Nolte, K. Bergner, R. Krämer, D. Richter, S. Richter, C. Voigtländer, and F. Zimmermann. Volume processing of transparent materials by ultrashort laser pulses. Proc. of Lasers and Electro-Optics/Pacific Rim, Busan, South Korea, 2015.

(C18) F. Zimmermann, A. Plech, A. Tünnermann and S. Nolte. Structural evolution of ultrashort pulse-induced nanogratings. 2nd workshop on Progress of Ultrafast Laser Modifications of Materials (PULMM), Neuchatel, Switzerland, 2016.

Acknowledgements

I would like to express my sincere gratitude towards all the people whose generous support throughout the last years has made this work possible.
First I want to thank my supervisor Prof. Dr. Stefan Nolte, head of the Ultrafast Optics group at the Institute of Applied Physics for this wonderful topic and the highly productive environment for research in his group. This work would not have been possible without his valuable advice, his critical and pointed questions which were always a big support in finishing my ideas and their presentations.
I am very grateful to the people with whom I had the opportunity to cooperate. At first I would like to thank PD Dr. Anton Plech from the Karlsruher Institute of Technology for the comprehensive support, valuable insights in the field of X-ray scattering and the ongoing fruitful discussions. In addition, I am deeply indebted to Prof. Dr. Matthieu Lancry and Prof. Dr. Bertrand Poumellec from the Institut de Chimie Moleculaire et des Materiaux d'Orsay, University of Paris Sud in France for showing me the capabilities of laser-materials processing of various glasses and hosting me in Paris. My research stay in Paris and Bordeaux was a unique possibility to extend my scientific knowledge and personal perception of life.
My long term office colleague Dr. Sören Richter deserves a very big thank for all the fruitful discussions, his experimental advices and versatile ideas for my work. I also like to spend my gratitude to Dr. Sven Döring for the fruitful discussions and conscientiousness giving me advices even for the tiniest details of my work. Many thanks go to my colleague Mr. Tobias Ullsperger for the opportunity to pass on what I have learned and support of various tasks.
Furthermore I want to thank the staff at the Institute of Applied Physics, in particular Mrs. Christiane Otto for the preparation of the manifold glass samples and Mr. Bodo Martin for the care about all the institute's computers and devices. Moreover I want to thank Natali Sergeev and Prof. Dr. Matthieu Lancry for recording the SEM images and Dr. Reinhard Geiss and Mr. Michael Steinert for the acquisition of the FIB-SEM images.

Special thanks go to Mr. Klaus Bergner, Dr. Gabor Matthäus, Mr. Frank Burmeister, Mr. Daniel Richter, Mrs. Ria Krämer, Mrs. Ulrike Blumröder, Dr. Robert Kammel and all the other colleagues from the ultrafast optics group of the IAP, for their assistance and the ambitious but pleasant atmosphere at the IAP.
I thank my friends Albert, Falko, Christian, Sören, Helena, Anne, Jan, Jana, Jura as well as my band colleagues Alexander and Nadine for helping me to free my mind keeping up my morale.
I am very indebted to my parents who have permanently given me great support, encouragement and joyful as well as relaxing times at home. Moreover, I want to thank my brother Martin for the meaningful discussions and diverse advices in all areas of life as well as my sister Anita who helped me extending my knowledge beyond the world of physics. In addition my cousins earn big thanks for always motivating and supporting me. Lastly, but most importantly great and profound gratitude goes to my wife Nadejda. She always kept on motivating and encouraging me for diverse ideas and activities.

Zusammenfassung

Gläser bieten außergewöhnliche optische, chemische und mechanische Eigenschaften. Durch die Entwicklung von Ultrakurzpulslasern konnte die hochpräzise Glasbearbeitung in den letzten Jahren revolutioniert werden, so dass vielfältige Aufgabenstellungen, z.B. im Bereich des lasergestützten Fügens, Bohrens oder Schneidens umgesetzt werden konnten. Bei allen diesen Verfahren stellt die nichtlineare Absorption der ultrakurzen Laserpulse die Grundlage dar [1, 2].

Über die direkte Bearbeitung hinaus ermöglichen ultrakurze Pulse das lokale Einschreiben anisotroper Strukturen in ein ansonsten isotropes Material mit Strukturgrößen kleiner als die Wellenlänge des Lichts. Diese sogenannten Nanogitter entstehen durch die kumulative Wirkung mehrerer hundert Laserpulse und sind stets senkrecht zur Polarisation des Einschreiblasers ausgerichtet [12, 15, 16]. Bekannt für ihre hohe Doppelbrechung ist der Entstehungsprozess der Nanogitter insbesondere aufgrund der kurzen Zeitskalen, komplexen physikalischen Mechanismen sowie der vergrabenen Strukturdetails jedoch noch nicht vollständig verstanden. Seit ihrer Entdeckung war lange unklar ob Nanogitter aus einer kontinuierlichen Brechzahlmodulation oder mikroskopischen Poren, welche in periodischen Stegen angeordnet sind, bestehen [53, 130]. Darüber hinaus wurden Nanogitter in verschiedenen Gläsern [152], Kristallen [153] und kürzlich sogar im Volumen von Halbleitern beobachtet [155]. Dies zeigt, dass ein übergeordneter Mechanismus ihre Entstehung diktiert.

Im Rahmen dieser Arbeit wurden die primären Bestandteile der Nanogitter, ihr Entstehen und Anordnung in periodischen Gitterstegen sowie die damit verknüpften Phänomene und Materialabhängigkeiten umfassend untersucht. Die Ergebnisse liefern neue Erkenntnisse über das komplexe Zusammenspiel der laser-induzierten Ionisierung, Defektbildung, Relaxation angeregter Ladungsträger sowie der folgenden Materialmodifikation.

Zunächst wurden Nanogitter in Kieselglas untersucht, das mit seiner einfachen Zusammensetzung und gut dokumentierten Eigenschaften als Material der Wahl diente, um die laser-induzierten Modifikationen zu analysieren. Die Entstehung der Nanogitter ist

ein sequentieller Prozess der mehrere Laserpulse pro Laserspot erfordert. Dahingegen definieren Laserparameter wie Pulsdauer, -energie und Fokussierung die Laserintensität und somit die Schwelle der Nanogitterentstehung. Die Absorption ultrakurzer Laserpulse geht mit dem Aufbrechen des Glasnetzwerkes und daraus resultierenden Defekten, wie z.B. Non-bridging Oxygen Hole Centers (NBOHCs) oder E' Centers einher, die die Ionisationsschwelle von Puls zu Puls reduzieren [15, 95, 24] und somit die Rückkopplung unter andauernder Bestrahlung vermitteln. Durch das Aufbrechen von Bindungen entsteht molekularer Sauerstoff, der sich in mikroskopischen Poren sammelt. Das wiederholte Aufheizen und Abkühlen des Glases resultiert aufgrund der hohen Abkühlraten in einer erhöhten fiktiven Temperatur im Vergleich zum unbestrahlten Glas, die aufgrund der Anomalität von Kieselglas eine lokale Verdichtung zur Folge hat. Als Resultat ist die mikroskopische Nanostruktur in verdichtetem Material eingebettet. Das niedrigere relative Volumen verursacht (als direkte Reaktion) Zugdehnungen innerhalb des bestrahlten Bereiches sowie im umgebenen Material. Die Amplitude der Zugdehnungen skaliert mit der Laserrepetitionsrate wie Messungen atomarer Bindungsabstände mittels Weitwinkelröntgenstreuung belegen. Durch mechanisches Trennen laser-bestrahlter Bereiche relaxiert der elastische Anteil teilweise, wodurch eine bimodale Oberflächendeformation aufgrund einer zugrunde liegenden Nanostruktur entsteht.

Durch die Verknüpfung von Kleinwinkelröntgenstreuung, Messungen des optischen Gangunterschieds sowie gezieltem Materialabtrag mittels fokussiertem Ionenstrahl und anschließender Rasterelektronenmikroskopie konnte eindeutig nachgewiesen werden, dass Nanogitter aus mikroskopischen Poren bestehen. Zum ersten Mal konnte die Entstehung dieser Poren, ihr Wachstum und Anordnung in regelmäßigen Gitterstegen beobachtet und systematisch untersucht werden. Wie sich zeigte, kann der sequentielle Entstehungsprozess in Abhängigkeit der Anzahl der eingestrahlten Laserpulse in 4 Phasen gegliedert werden: Einzelne fokussierte ultrakurze Laserpulse induzieren isotrope zylindrische Löcher, die sich vollkommen deterministisch und ohne die Anwesenheit intrinsischer Materialinhomogenitäten bilden (Phase 1). Durch eine höhere Anzahl von Laserpulsen pro Spot werden diese Löcher deformiert und zufällig angeordnete Materialinhomogenitäten entstehen (Phase 2). Diese bilden den Keim für das Wachstum anisotroper Poren aufgrund von Feldverstärkung senkrecht zur Laserpolarisation in Kombination mit Defekt-induzierter Absorption von Puls zu Puls (Phase 3). Nachdem sich eine Vielzahl von Poren gebildet hat, richten sich diese exakt senkrecht zur Polarisationsrichtung aus und die Porenzahl steigt weiter an (Phase 4). Während die Anordnung der Poren zunächst entsprechend des in

[15, 24] beschriebenen nanoplasmonischen Modells erfolgen kann, sind andere Effekte, wie z.B. die kohärente Überlagerung des an bestehenden Gitterstegen gestreuten Feldes für die Entstehung neuer Gitterstege und so die kontinuierliche Reduktion der Periode (auch unterhalb $\lambda/2n$) verantwortlich [96]. Dieser Ansatz liefert eine Erklärung für die verringerte Gitterperiode bei wiederholtem Wiederbeschreiben. Mit jedem erneuten Ausrichten der Nanogitter steigt die Anzahl anisotroper Poren und so das Füllverhältnis der Gitterstege, was aufgrund der stärkeren Streuung kleinere Perioden begünstigt.
Die Ergebnisse erklären diverse Aspekte im Zusammenhang mit Nanogittern. Zunächst bestehen Nanogitter aus leeren (bzw. gas-gefüllten) Poren, die sich in regelmäßigen Stegen anordnen. Daraus resultiert die enorme Doppelbrechung trotz der geringen Strukturgröße eingebrachter Modifikationen. Ebenfalls erklärt dies die stark anisotrope Ätzrate in Abhängigkeit der Polarisationsrichtung des Einschreiblasers [26]. Des Weiteren zeigt der oben genannte Mechanismus, dass die Entwicklung der Nanogitter direkt mit der Entstehung makroskopischer Voids, die typischerweise bei höheren Pulsenergien beobachtet werden, verknüpft ist. Daher ist die Bildung von Nanogittern in Gläsern wie z.B. Borosilikatglas gehemmt [61], in denen kaum Voids beobachtet werden [138]. Der oben genannte Entstehungsmechanismus ist sowohl für punktweises Einschreiben gültig als auch für den Fall, dass der Laserfokus kontinuierlich verfahren wird. Im letzten Fall sind jedoch weniger Pulse pro Laserspot für die Entstehung der Nanogitter notwendig. Nach nur wenigen Laserpulsen pro Spot (in Phase 2) begünstigt die Akkumulation Laser-induzierter Spannungen die Entstehung von Rissen entlang der Verfahrrichtung. Diese Risse dienen als Keim für das Wachstum anisotroper Poren aufgrund lokaler Feldverstärkung, insbesondere wenn die Polarisation senkrecht zur Verfahrrichtung orientiert ist. Dahingegen wird im Fall von punktweisem Einschreiben die Anordnung regelmäßiger Nanogitter stark verzögert wie die in-situ Beugungsmessungen an Nanogitterproben belegen, da keine Keime (bzw. elongierte Risse entlang der Verfahrrichtung) für das Wachstum der Poren vorliegen. Im Weiteren liefert der Ansatz der sinkenden Gitterperiode auf Basis kohärenter Überlagerung des gestreuten Feldes eine Erklärung für die, in dieser Arbeit gemessenen, kleinen Perioden Laser-induzierter Oberflächengitter (engl.: Laser-Induced Periodic Surface Structures, kurz: LIPSS) [151].
Im Rahmen dieser Arbeit konnte nachgewiesen werden, dass Nanogitter in verschiedenen Gläsern erzeugt werden können. Sie stellen keine Eigenheit von Kieselglas dar und sind nicht mit dem anomalen Verhalten der Glasdichte in Abhängigkeit der fiktiven Temperatur verknüpft. Der Entstehungsmechanismus in dotiertem Glas (z.B. ULE oder Germanium

dotiertes Silikatglas) sowie in Borosilikat basiert auf Porenwachstum sowie nachfolgender Ausrichtung der Poren. Thermomechanische Eigenschaften beeinflussen die Schwelle der Nanogitterentstehung (z.B. in Abhängigkeit der Laserwiederholrate), die Zersetzung des Glases unter Bestrahlung mittels ultrakurzer Laserpulse in eine poröse Nanostruktur sowie mikroskopische Eigenschaften, wie z.B. die Dicke der Poren. Eine niedrigere Modifikationsschwelle (z.B. durch Defekt-basierte Absorption) kann die Anordnung in periodischen Gitterstegen beschleunigen. Zusätzlich zeigen die Untersuchungen der Nanogitter in Borofloat 33 in Übereinstimmung mit aktuellen theoretischen Studien [77], dass intrinsische Inhomogenitäten die Periode laser-induzierter Nanostrukturen stark beeinflussen. Zum ersten Mal konnte eine Nanogitterperiode von 60 nm ($\approx \lambda/10$n) beobachtet werden.

Nanogitter können wiederbeschrieben werden, d.h. ein bereits bestehendes Gitter kann durch Einschreiben an der gleichen Stelle aber mit gedrehter Polarisation ausgelöscht und neu angeordnet werden. Dieser Prozess wurde im Rahmen der Arbeit umfassend untersucht wobei die Ergebnisse zeigen, dass die Gitterentstehung in der gleichen Abfolge für wiederholtes Wiederbeschreiben geschieht. Dennoch führt wiederholtes Einschreiben des Gitters dazu, dass die Porosität des Glases steigt woraus eine höhere Doppelbrechung bei hohem Pulsüberlapp resultiert. Obwohl die Gitterqualität bei mehrfachem Überschreiben degradiert, ermöglicht das Wiederbeschreiben diverse Anwendungen wie z.B. wiederbeschreibbare optische Datenspeicherung mit enormen Datendichten [67].

Die Verknüpfung von intrinsischen Glaseigenschaften und induzierter Periode der Nanostrukturen ermöglicht die Herstellung diverser photonischer Bauelemente auf Grundlage maßgeschneiderter Gitter- und den damit verbundenen optischen Eigenschaften. In diesem Rahmen wurde demonstriert, dass das lokale Einschreiben anisotroper Nanostrukturen mit ansonsten schwer realisierbaren Strukturgrößen genutzt werden kann, um z.B. Wellenplatten zur nahezu beliebigen Polarisationsmanipulation herzustellen. Zum einen dienen Nanogitter-basierende Wellenplatten zur Erzeugung von optischen Vortex-Strahlen mit radialer oder azimutaler Polarisation die im Weiteren z.B. als optische Pinzette mit variablem Bahndrehimpuls genutzt werden können [176]. Die Transmission der Wellenplatten kann z.B. für die Anwendung in Hochleistungslasern durch Ausheizen Laser-induzierter Defekte deutlich erhöht werden. Zum anderen wurde eine polarisationskodierte Beleuchtung generiert, die strukturierte Beleuchtungsmikroskopie in einer einzigen Aufnahme gewährleistet. Die schnellere Bildgebung ermöglicht es, rasante mechanische oder biologische Prozesse mit hoher Auflösung zu beobachten. Dabei weisen die

Nanogitter-basierenden Wellenplatten hohe Temperaturstabilität bis 850°C auf, so dass selbst Anwendungen unter extremen Bedingungen denkbar sind.
Zukünftig könnten weitere Untersuchungen die Porenentstehung selbst oder die Reduktion der Nanogitterperiode (durch z.B. Aufteilen eines bestehenden Gittersteges [96]) auf Grundlage zeitaufgelöster Röntgenstreuung adressieren. Für letzteres wäre eine Zeitauflösung von Puls zu Puls ausreichend, um strukturelle Änderungen eines gegebenen Nanogittervolumens zu analysieren.

Ehrenwörtliche Erklärung

Ich erkläre hiermit ehrenwörtlich, dass ich die vorliegende Arbeit selbständig, ohne unzulässige Hilfe Dritter und ohne Benutzung anderer als der angegebenen Hilfsmittel und Literatur angefertigt habe. Die aus anderen Quellen direkt oder indirekt übernommenen Daten und Konzepte sind unter Angabe der Quellen gekennzeichnet.
Bei der Auswahl und Auswertung des folgenden Materials haben mir die nachstehend aufgeführten Personen in der jeweils beschriebenen Weise unentgeltlich geholfen:

1. Die SAXS und WAXS Messungen an der cSAXS beamline des Paul Scherrer Instituts Villigen (Ch) wurden in Zusammenarbeit mit PD Dr. Anton Plech, Karlsruher Institut für Technologie durchgeführt.

2. Die Absorptionsmessungen in Kapitel 3.3.1 sowie die Messungen des optischen Gangunterschieds in Abbildung 4.15 wurden in Zusammenarbeit mit Dr. Sören Richter aufgenommen.

3. Die Photolumineszenz in Kapitel 3.3 wurde in Zusammenarbeit mit Dr. B. Hari Babu, Universität Paris Süd gemessen.

4. Die Aufnahmen des Keramikchips mittels picoSIM sowie mittels Weitfeldmikroskopie in Abbildung 5.3 wurde von M. Sc. Sapna Shukla erstellt.

Weitere Personen waren an der inhaltlich-materiellen Erstellung der vorliegenden Arbeit nicht beteiligt. Insbesondere habe ich hierfür nicht die entgeltliche Hilfe von Vermittlungs bzw. Beratungsdiensten (Promotionsberater oder anderen Personen) in Anspruch genommen. Niemand hat von mir unmittelbar oder mittelbar geldwerte Leistungen für Arbeiten erhalten, die im Zusammenhang mit dem Inhalt der vorgelegten Dissertation stehen.
Teile dieser Arbeit wurden aus Prioritätsgründen bereits veröffentlicht oder zur Veröffentlichung eingereicht [61, 128, 133, 136, 146, 156, 162, 178, 179, 180, 181]. Die Arbeit wurde bisher weder im In- noch im Ausland in gleicher oder ähnlicher Form einer anderen Prüfungsbehörde vorgelegt.
Die geltende Promotionsordnung der Physikalisch-Astronomischen Fakultät ist mir bekannt. Ich versichere ehrenwörtlich, dass ich nach bestem Wissen die reine Wahrheit gesagt und nichts verschwiegen habe.

Jena, den Felix Zimmermann

Lebenslauf

Persönliche Daten

Name	Felix Ralf Zimmermann
Geburtsdatum, -ort	24.06.1986, Suhl

Ausbildung

06/2005	Abitur am Johann-Gottfried-Herder-Gymnasium Suhl
09/2005 - 05/2006	Zivildienst Suhl
10/2006 - 11/2011	Studium der Physik an der Friedrich-Schiller-Universität Jena
11/2011	Abschluss des Jenaer Physik-Studiums mit dem Diplom

Wissenschaftlicher Werdegang

04/2009 - 01/2012	Studentische Forschungsaufgaben an der Friedrich-Schiller-Universität Jena
09/2010	Forschungspraktikum am Forschungszentrum Jülich
12/2010 - 11/2011	Diplomarbeit am Institut für Angewandte Physik, FSU Jena
05/2015 - 06/2015	Forschungsaufenthalt an der Universität Paris-Süd, Frankreich
seit 03/2012	Promotion am Institut für Angewandte Physik, FSU Jena

Jena, den Felix Zimmermann